UNIVERSITÀ DEGLI STUDI DI NAPOLI "FEDERICO II"

Dottorato di Ricerca in Fisica Fondamentale ed Applicata
XVIII Ciclo

Dr. Diego Monorchio

Study of the properties of the a_1 meson produced in the $B \to D^{*-} a_1^+$ decay at the BABAR Experiment

Thesis for Doctor of Philosophy degree

Coordinatore del Dottorato di Ricerca:
Prof. Arturo Tagliacozzo

NOVEMBRE 2005

Contents

Introduction

In their first seven years of running, the two experiments at the B-factories BABAR and Belle have reached impressive results in their investigation on the Standard Model flavor sector.
The CP violation in the B meson decays has been clearly established, and the efforts of the two collaboration are now concentrated on the attempt to over-constraint the Cabibbo-Kobayashi-Maskawa quark mixing matrix through independent measurements of the Unitarity Triangle parameters, related to the B meson decay properties, and search for new physics effects.
Besides this primary goal, the high luminosity of PEP-II, coupled with the high acceptance of the BABAR detector, allows competitive measurements not only in B-physics but also in other fields such as hadron spectroscopy, charm and τ physics.

The work presented in this thesis, consists in the study of the properties of the a_1 meson produced in the $B \to D^{*-} a_1^+$ ($a_1^+ \to \pi^-\pi^+\pi^+$) decay at the BABAR experiment.
First discovered as a $\rho\pi$ resonance in pion-proton scattering, the axial vector meson a_1 remained an elusive prey due its large width and the presence of high physical backgrounds.
Two class of experiments, based on different production processes, have been performed to study this particle: hadronic production experiments and $\tau \to a_1\nu_\tau$ decays. They give inconsistent results on the measurements of the a_1 pole mass and width (see section 3.3). For this reason the Particle Data Group [13] does not quote a world average for these quantities but only provide a conservative estimate:

$$\begin{array}{rcl} m_{a_1}^{PDG} & = & 1230 \pm 40 \text{ MeV} \\ \Gamma_{a_1}^{PDG} & \text{between} & 250 \text{ and } 600 \text{ MeV}. \end{array} \quad (1)$$

Also the theoretical understanding of the a_1 is not rigorous. Many models have been proposed

[75, 49] to describe the line-shape and the resonant substructures, but none have provided an entirely satisfactory description of the data. Additional experimental inputs are essential for a better understanding of this system.

In this work, for the first time the a_1 meson is studied through the $B \to D^{*-} a_1^+$ ($a_1^+ \to \pi^-\pi^+\pi^+$) process. The huge number of B's produced at BABAR , together with the high branching ratio of this decay and with the numerous kinematic constraints that can be applied in the B meson reconstruction, make this channel a quite clean environment to study the a_1 resonance.
We have performed a Dalitz plot analysis (based on the standard Isobar model described in section 5.2) of the 3 pions system produced in the $B \to D^{*-}\pi^+\,\pi^+\,\pi^-$ decays. This kind of analysis allows to reach to different purposes. The first one is to separate the a_1 resonance from other possible spin parity states that can contribute to the three pion mass spectrum: the resulting a_1 mass distribution is then used to determine the pole mass and the width of this particle. The second purpose is the study of the substructures contributing to the $a_1^+ \to \pi^-\pi^+\pi^+$ process providing information on the strong decay dynamics.

In addition to the possibility to study the a_1 meson, the $B \to D^{*-} a_1^+$ decay presents also other reasons of interest, more strictly related to the B physics.
As recently suggested in [27], measuring the polarization amplitudes in the $B \to D^{*-} a_1^+$ decay provides a test of the factorization assumption. Factorization represents one of the mostly used tool to evaluate the hadronic matrix elements describing the QCD non-perturbative effects in the B decays amplitudes. Despite this approach, and its extensions, was found to predict with good accuracy several processes, there are cases where it fails and it is important to test it in depth in order to verify its limits and improve our knowledge on the strong interactions effects in exclusive weak decays of hadrons containing a b-quark.
Moreover the study of time dependent CP asymmetries in $B \to D^* a_1$ decays can be used to extract the weak phase $(2\beta + \gamma)$, providing a further constraint on the Unitarity Triangle.

The present thesis is organized in five chapters.
Chapter 1 represents an introduction to the main topic actually under study at BABAR : the determination of the Standard Model parameters through the measurements of the B meson decay

properties.

Chapter 2 is devoted to a detailed description of the BABAR detector, built around the e^+e^- interaction region of the B-factory PEP-II.

Chapter 3 is an introduction to the study of the non-leptonic $B \to D^{*-}a_1^+$ mode. It contains a summary on the current status of knowledge on the a_1 meson and an introduction to the spin parity analysis technique adopted to study the three pions system. Moreover the factorization test through the polarization measurement and the measurement of $(2\beta + \gamma)$ from the study of time dependent CP asymmetries in $B \to D^{*-}a_1^+$ are discussed.

Chapter 4 contains a detailed description of the criteria adopted to select the $B \to D^{*-}a_1^+$ decay and a discussion on the main discriminating variables used for background rejection and characterization.

In chapter 5 it is described the spin parity analysis of the 3 pions system based on the Isobar model. The results on the a_1 substructure study and the measurement of the a_1 mass and width are presented.

Chapter 1

B physics and the Standard Model

1.1 Introduction

This chapter is a theoretical introduction to the main topic actually under study by the BABAR experiment: the determination of the Standard Model parameters through the measurements of the B meson decay properties.
In section 1.2 is introduced the Cabibbo-Kobayashi-Maskawa (CKM) matrix, which describes the flavor-changing weak coupling between the quarks: in the Standard Model it contains the source of CP-violation.
In section 1.3 the Unitarity Triangle is discussed. It represents the unitarity of the CKM matrix in the b sector. The main goal of the experiments at the B -factories, Belle and BABAR , is to over-constraint the position of the Unitarity Trianlge vertex by combining several independent measurements of the B decays properties. The recent results on the Unitarity Triangle analysis are reported in this section.
Section 1.4 discuss the time evolution of the neutral B meson and the so called $B^0\overline{B}^0$ mixing. It is also shown how CP violation manifests itself in time dependent asymmetries arising from the interference between B decays with and without mixing.
The time dependent CP asymmetries can be directly related to the Unitarity Triangle angles, and, in section 1.5, the concrete example of the $\sin(2\beta+\gamma)$ measurement in $B \rightarrow D^{(*)}h$ decays is illustrated.

1.2 The Standard Model and the CKM matrix

The Standard Model of particle physics [1] is a field theory, with local gauge symmetry $SU(3)_C \times SU(2)_L \times U(1)_Y$, and describes the strong, weak, and electromagnetic interactions between the known elementary particles. The electromagnetic and weak interactions are discussed in detail in References [2, 3], while a very good introduction to the strong interaction can be found in Reference [4].

The fundamental ingredients of the Standard Model are six leptons and six quarks divided in three generations. Each of these particles has an antiparticle, with the same mass but opposite electrical charge and *quantum numbers*, e.g. strangeness and beauty. Each quark generation, commonly called a quark flavor, consists of three multiplets:

$$Q_L^I = \begin{pmatrix} U_L^I \\ D_L^I \end{pmatrix} = (3,2)_{+1/6}, \quad u_R^I = (3,1)_{+2/3}, \quad d_R^I = (3,1)_{-1/3}, \tag{1.1}$$

where $(3,2)_{+1/6}$ denotes a triplet of $SU(3)_C$, doublet of $SU(2)_L$ with hyper-charge $Y = Q - T_3 = +1/6$, and similarly for the other representations.

Family			Quantum Numbers			
1	2	3	T	T_3	Y	$Q = Y/2 + T_3$
$\begin{pmatrix} \nu_e \\ e \end{pmatrix}_L$	$\begin{pmatrix} \nu_\mu \\ \mu \end{pmatrix}_L$	$\begin{pmatrix} \nu_\tau \\ \tau \end{pmatrix}_L$	$1/2$	$+1/2$	-1	0
			$1/2$	$-1/2$	-1	-1
e_R	μ_R	τ_R	0	0	-2	-1
$\begin{pmatrix} u \\ d \end{pmatrix}_L$	$\begin{pmatrix} c \\ s \end{pmatrix}_L$	$\begin{pmatrix} t \\ b \end{pmatrix}_L$	$1/2$	$+1/2$	$+1/3$	$+2/3$
			$1/2$	$-1/2$	$+1/3$	$-1/3$
u_R	c_R	t_R	0	0	$4/3$	$+2/3$
d_R	s_R	b_R	0	0	$-2/3$	$-1/3$

Table 1.1: Electroweak interaction multiplets.

The interactions of quarks with the $SU(2)_L$ gauge bosons are described by the Lagrangian

$$\mathcal{L}_W = -\frac{1}{2} g \overline{Q^I_{Li}} \gamma^\mu \tau^a \mathbf{1}_{ij} Q^I_{Lj} W^a_\mu + \text{Hermitian conjugate} \,, \tag{1.2}$$

where g is the weak coupling constant, γ^μ operates in Lorentz space, τ^a operates in $SU(2)_L$ space, and $\mathbf{1}$ is the unit matrix operating in generation (flavor) space. This unit matrix is written explicitly to make the transformation to mass eigenbasis clearer.

The Standard Model includes also a single Higgs scalar doublet field $\phi(1,2)_{+1/2}$. The interactions between the quarks and this field generate the fermion masses through the spontaneous symmetry breaking mechanism [5]. The Lagrangian for these interactions is given by the Yukawa coupling:

$$\mathcal{L}_Y = -\mathbf{G}_{ij} \overline{Q^I_{Li}} \phi d^I_{Rj} - \mathbf{F}_{ij} \overline{Q^I_{Li}} \tilde{\phi} u^I_{Rj} + \text{H.c.}, \tag{1.3}$$

where $\mathbf{G}$ and $\mathbf{F}$ are general *complex* 3×3 matrices. Their complex nature is the source of CP violation in the Standard Model. Due to the non-zero expectation value of the Higgs field in the vacuum, $\langle \phi \rangle = 1/\sqrt{2}(v, 0)$, the spontaneous symmetry breaking transforms $SU(2)_L \otimes U(1)_Y$ in $U(1)_{\text{EM}}$, and the two components of the quark doublet become distinguishable, as are the three members of the W^μ triplet. The charged current interaction in (1.2) is given by

$$\mathcal{L}_W = -\sqrt{\frac{1}{2}} g \overline{u^I_{Li}} \gamma^\mu \mathbf{1}_{ij} d^I_{Lj} W^+_\mu + \text{h.c.}. \tag{1.4}$$

The mass terms for the quarks arise from the replacement $\Re(\phi^0) \rightarrow \sqrt{\frac{1}{2}}(v + H^0)$ in (1.3) of the ϕ field near its minimum $\langle \phi \rangle$, and are given by

$$\mathcal{L}_M = -\sqrt{\frac{1}{2}} v \mathbf{G}_{ij} \overline{d^I_{Li}} d^I_{Rj} - \sqrt{\frac{1}{2}} v \mathbf{F}_{ij} \overline{u^I_{Li}} u^I_{Rj} + \text{H.c.} \,, \tag{1.5}$$

with

$$\mathbf{M}_d = \mathbf{G} v/\sqrt{2}, \quad \mathbf{M}_u = \mathbf{F} v/\sqrt{2}. \tag{1.6}$$

The quark fields in (1.1) are eigenstates of the weak interaction but do not correspond to the quark states in nature with definite mass. This is commonly referred to as the mass eigenstates being *rotated* with respect to the eigenstates of the weak interactions [6].

Since the two eigenbases are not identical, the mass matrices $\mathbf{M}_d$ and $\mathbf{M}_u$ do not correspond to the physical masses of the quarks. These matrices can be transformed to the mass eigenbasis by defining four unitary matrices such that

$$\mathbf{V}_{dL} \mathbf{M}_d \mathbf{V}^\dagger_{dR} = \mathbf{M}^{\text{diag}}_d, \quad \mathbf{V}_{uL} \mathbf{M}_u \mathbf{V}^\dagger_{uR} = \mathbf{M}^{\text{diag}}_u, \tag{1.7}$$

where $\mathbf{M}_q^{\rm diag}$ are diagonal and real, while $\mathbf{V}_{qL}$ and $\mathbf{V}_{qR}$ are complex. In the mass basis the charged current interactions (1.4) can be rewritten as

$$\mathcal{L}_W = -\sqrt{\frac{1}{2}} g \overline{u_{Li}} \gamma^\mu \overline{\mathbf{V}}_{ij} d_{Lj} W_\mu^+ + \text{h.c.}. \tag{1.8}$$

Here the quark fields are in the mass eigenbasis. The matrix $\overline{\mathbf{V}} = \mathbf{V}_{uL}\mathbf{V}_{dL}^\dagger$ is the unitary mixing matrix for three quark generations.

A unitary $n \times n$ complex matrix generally depends on $2n^2$ parameters. The condition of unitarity reduces this number to a total of n^2 independent parameter. Using the properties of orthogonal matrices, these parameters can be divided in

- $\frac{1}{2}n(n-1)$ real angles, and
- $n^2 - \frac{1}{2}n(n-1) = \frac{1}{2}n(n+1)$ complex phases

For n families of quarks, there are $2n$ quark fields. Physical observables are invariant under phase redefinitions of the fields, and is possible to remove $2n-1$ of the complex phases by redefining the quark fields. Therefore, there are

- $\frac{1}{2}n(n+1) - (2n-1 = \frac{1}{2}(n-1)(n-2)$ irreducible complex phases

in the unitary $n \times n$ complex matrix.

In case of the mass matrices, there are three real angles and six total complex phases. The number of phases in $\bar{V}$ is reduced by a transformation

$$\overline{\mathbf{V}} \implies \mathbf{V} = \mathbf{P}_u \overline{\mathbf{V}} \mathbf{P}_d^*, \tag{1.9}$$

where $\mathbf{P}_u$ and $\mathbf{P}_d$ are diagonal matrices of pure complex phases. This transformation corresponds to redefining the phases of the quark fields in the mass eigenbasis:

$$q_{Li} \to (\mathbf{P}_q)_{ij} q_{Lj}, \quad q_{Ri} \to (\mathbf{P}_q)_{ij} q_{Rj}, \tag{1.10}$$

which does not change the real diagonal mass matrix $\mathbf{M}_q^{\rm diag}$. The five phase differences among the elements of $\mathbf{P}_u$ and $\mathbf{P}_d$ can be chosen so that the transformation (1.9) eliminates five of the six

independent phases from $\overline{\mathbf{V}}$. The new matrix $\mathbf{V}$ is left with three real angles and one irreducible complex phase.

The presence of this irreducible phase is the source of CP violation in the Standard Model. This can be easily understood by observing that the mass lagrangian $\mathcal{L}_M$ of eq. 1.5 is the sum of two terms of the type

$$\bar{u}M(1+\gamma_5)u + \bar{u}M^\dagger(1+\gamma_5)u = \bar{u}(M+M^\dagger)u + \bar{u}(M+M^\dagger)\gamma_5 u. \tag{1.11}$$

The properties of this term under C and P transformations are given by:

$$\begin{aligned} \bar{u}(M+M^\dagger)u + \bar{u}(M+M^\dagger)\gamma_5 u &\longmapsto \bar{u}(M+M^\dagger)u - \bar{u}(M+M^\dagger)\gamma_5 u \quad \text{under} \quad P \\ \bar{u}(M+M^\dagger)u + \bar{u}(M+M^\dagger)\gamma_5 u &\longmapsto \bar{u}(M^T+M^*)u - \bar{u}(M^T+M^*)\gamma_5 u \quad \text{under} \quad C \end{aligned} \tag{1.12}$$

so that

$$\bar{u}(M+M^\dagger)u + \bar{u}(M+M^\dagger)\gamma_5 u \longmapsto \bar{u}(M^T+M^*)u + \bar{u}(M^T+M^*)\gamma_5 u \quad \text{under} \quad CP. \tag{1.13}$$

This means that

$$\mathcal{L}_M \longmapsto \mathcal{L}_M \quad \text{under} \quad CP \iff M = M^*, \tag{1.14}$$

i.e. the presence of an irreducible phase in the results in a non CP invariant lagrangian.

This phase is called the Kobayashi-Maskawa phase [7], δ_{KM}, and the mixing matrix is called the Cabibbo-Kobayashi-Maskawa (CKM) matrix [8, 7].

It is important to note that the existence of the third generation of quarks is a necessary ingredient for the presence of the complex phase, and therefore CP violation in the Standard Model. In a Standard Model with only two generations of quarks, the procedure described above removes all the complex phases and the 2×2 mixing matrix $\mathbf{V}$ is left with only one real parameter which is the Cabibbo angle. It was this observation that led Kobayashi and Maskawa to suggest a third quark generation in 1973 long before the discovery of the beauty quark b in 1977 [9, 10] and of the top quark t in 1995 [11, 12].

The presence of only one complex phase in the CKM model implies that all CP-violating effects are closely related. Therefore different physical processes, such as decays of Kaons and B mesons, can be used to probe the same source of CP violation.

The CKM matrix $\mathbf{V}$ can be symbolically written as

$$\mathbf{V} \equiv \begin{pmatrix} V_{ud} & V_{us} & V_{ub} \\ V_{cd} & V_{cs} & V_{cb} \\ V_{td} & V_{ts} & V_{tb} \end{pmatrix} , \tag{1.15}$$

which explicitly shows the flavor-changing aspect of the weak interactions. Each element $\mathbf{V}_{q_i q_j}$ determines the amplitude of interactions between quarks q_i and q_j. The magnitude of all nine elements of this matrix have now been measured in the weak decays of hadrons containing the relevant quarks, and in some cases in the deep inelastic neutrino–nucleon scattering [13]. The precision on these elements reflects both the experimental limitations and the theoretical uncertainties associated with the imprecise knowledge of the hadronic quantities required to analyze the experimental data [6]. Present knowledge of the magnitude $|V_{ij}|$ of the matrix elements can be summarized as [13]

$$|\mathbf{V}| \equiv \begin{pmatrix} 0.9739 - 0.9751 & 0.221 - 0.227 & 0.0029 - 0.0045 \\ 0.221 - 0.227 & 0.9730 - 0.9744 & 0.039 - 0.044 \\ 0.0048 - 0.014 & 0.037 - 0.043 & 0.9990 - 0.9992 \end{pmatrix} . \tag{1.16}$$

where the values are the 90% confidence limits on $|V_{ij}|$.

1.3 The Unitarity Triangle

There are several parameterizations of the CKM matrix $\mathbf{V}$ that exhibit its unitarity explicitly. One of these is considered commonly the "standard" parameterization [14] and utilizes three angles θ_{12}, θ_{23}, θ_{13}, and a complex phase $\delta \equiv \delta_{\rm KM}$

$$\mathbf{V} = \begin{pmatrix} c_{12}c_{13} & s_{12}c_{13} & s_{13}e^{-i\delta} \\ -s_{12}c_{23} - c_{12}s_{23}s_{13}e^{i\delta} & c_{12}c_{23} - s_{12}s_{23}s_{13}e^{i\delta} & s_{23}c_{13} \\ s_{12}s_{23} - c_{12}c_{23}s_{13}e^{i\delta} & -c_{12}s_{23} - s_{12}c_{23}s_{13}e^{i\delta} & c_{23}c_{13} \end{pmatrix} , \tag{1.17}$$

with $c_{ij} \equiv \cos\theta_{ij}$ and $s_{ij} \equiv \sin\theta_{ij}$, and indexes $i, j = 1, 2, 3$ corresponding to the three quark generations. In this parameterization, the angles θ_{ij} are related to the amount of "mixing" between two generations i and j. For example θ_{12} corresponds to the Cabibbo angle [8].

The unitarity of $\mathbf{V}$ implies nine constraints between its elements. Three of these constraints are relative to the elements of each row

$$\begin{array}{rcrcrcl} |V_{ud}|^2 & + & |V_{us}|^2 & + & |V_{ub}|^2 & = & 1\,, \\ |V_{cd}|^2 & + & |V_{cs}|^2 & + & |V_{cb}|^2 & = & 1\,, \\ |V_{td}|^2 & + & |V_{ts}|^2 & + & |V_{tb}|^2 & = & 1\,, \end{array} \tag{1.18}$$

while the other six express the condition of orthogonality between any pair of rows or any pair of columns of the matrix. The six orthogonality conditions require the sum of three complex terms to vanish and can be represented graphically as triangles in the complex plane [14, 15, 16]. All these triangles have the same area $|J|/2$, with $J = c_{12}c_{23}c_{13}^2 s_{12}s_{23}s_{13}\sin\delta$.

Three of these triangles, defined by

$$V_{ud}V_{us}^* + V_{cd}V_{cs}^* + V_{td}V_{ts}^* = 0, \tag{1.19}$$

$$V_{us}V_{ub}^* + V_{cs}V_{cb}^* + V_{ts}V_{tb}^* = 0, \tag{1.20}$$

$$V_{ud}V_{ub}^* + V_{cd}V_{cb}^* + V_{td}V_{tb}^* = 0\,, \tag{1.21}$$

are very useful in understanding the Standard Model predictions for CP violation, and are shown in Figure 1.1.

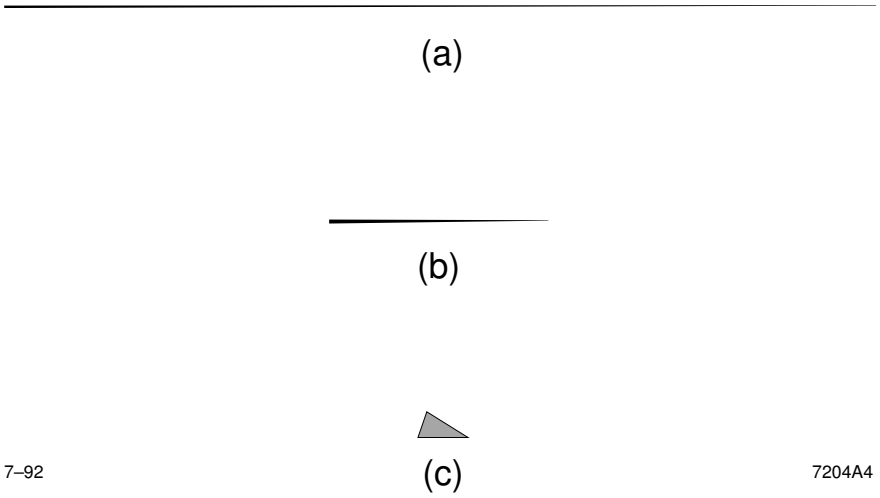

Figure 1.1: The unitarity triangles defined by (1.19) in a), (1.20) in b), and (1.21) in c). The same scale has been used for all triangles.

The length of the sides of these triangles can be measured from the decay rates of, respectively, $K \equiv (\bar{s}d)$, $B_s \equiv (\bar{b}s)$, and $B_{\ d} \equiv (\bar{b}d)$ mesons.

The size of the angles are proportional to the magnitude of CP-violating effects in the decays of, respectively, K, B_s, and B_d mesons. In case of the K and B_s mesons, the experimental precision needs to be high in order to be able to resolve the structure of the flat triangles.

On the contrary, the third triangle, related to the B_d mesons, is expected to have large angles, which result in large CP-violating effects. This triangle is illustrated in Figure 1.1c, and is commonly referred to as the "Unitarity Triangle".

It is customary to study the Unitarity Triangle with the Wolfenstein parametrization [17] of the CKM matrix. In this parameterization, matrix $\mathbf{V}$ is written as [14]

$$\mathbf{V} = \begin{pmatrix} 1-\frac{\lambda^2}{2} & \lambda & A\lambda^3(\rho - i\eta) \\ -\lambda & 1-\frac{\lambda^2}{2} & A\lambda^2 \\ A\lambda^3(1-\rho-i\eta) & -A\lambda^2 & 1 \end{pmatrix} + \mathcal{O}(\lambda^4)\ , \tag{1.22}$$

with $\lambda = |V_{us}| = 0.22$ playing the role of the expansion parameter, and A, ρ, and η real numbers of the order of unity. The parameters of the standard parameterization (1.17) are related to the Wolfenstein parameters in (1.22) by

$$s_{12} \equiv \lambda, \quad s_{23} \equiv A\lambda^2, \quad s_{13}e^{-i\delta} \equiv A\lambda^3(\rho - i\eta)\ . \tag{1.23}$$

The CKM elements can be written in terms of the Wolfenstein parameters A, ρ, and η, by using relation (1.23), as

$$V_{us} = \lambda, \quad V_{cb} = A\lambda^2, \quad V_{ub} = A\lambda^3(\rho - i\eta), \tag{1.24}$$

$$V_{td} = A\lambda^3(1 - \bar{\rho} - i\bar{\eta}), \tag{1.25}$$

$$ImV_{cd} = -A^2\lambda^5\eta, \quad ImV_{ts} = -A\lambda^4\eta, \tag{1.26}$$

with

$$\bar{\rho} = \rho(1 - \lambda^2/2), \quad \bar{\eta} = \eta(1 - \lambda^2/2)\ . \tag{1.27}$$

These expressions are valid up to $\mathcal{O}(\lambda^6)$ corrections and turn out to be excellent approximations to their exact expressions[18].

The rescaled Unitarity Triangle in Figure 1.2b is derived from (1.21) by choosing a phase convention such that $V_{cd}V_{cb}^*$ is real, dividing the lengths of all sides by $V_{cd}V_{cb}^*$, and aligning one side of hte

triangle with the real axis. Two vertexes of the rescaled Unitarity Triangle are thus fixed at (0,0) and (1,0), while the coordinates of the remaining vertex are denoted by $(\bar{\rho}, \bar{\eta})$. In the $(\bar{\rho}, \bar{\eta})$ plane,

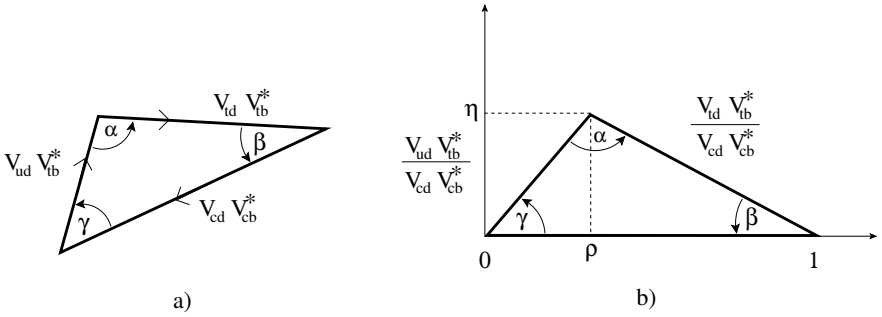

Figure 1.2: (a) The Unitarity triangle as defined in relation (1.21), and (b) the rescaled triangle, where all sides are divided by $V_{cb}^* V_{cd}$.

the lengths of the sides of the triangle are given by

$$R_b \equiv \sqrt{\bar{\rho}^2 + \bar{\eta}^2} = \frac{1 - \lambda^2/2}{\lambda} \left| \frac{V_{ub}}{V_{cb}} \right|, \quad R_t \equiv \sqrt{(1-\bar{\rho})^2 + \bar{\eta}^2} = \frac{1}{\lambda} \left| \frac{V_{td}}{V_{cb}} \right| , \tag{1.28}$$

Similarly, the three angles α, β, and γ are defined by

$$\alpha \equiv \arg \left[-\frac{V_{td} V_{tb}^*}{V_{ud} V_{ub}^*} \right], \quad \beta \equiv \arg \left[-\frac{V_{cd} V_{cb}^*}{V_{td} V_{tb}^*} \right], \quad \gamma \equiv \arg \left[-\frac{V_{ud} V_{ub}^*}{V_{cd} V_{cb}^*} \right] \equiv \pi - \alpha - \beta \, . \tag{1.29}$$

It is possible to perform various independent measurements of the angles and the sides which can over-constrain the Unitarity Triangle and then test the Standard Model. Most of the constraints for the Unitarity Triangle vertex come from measurements of rates and CP asymmetries in B mesons decays that are actually the main goal pursued by the experiments at the B -factories BABAR and Belle.

Various analysis exist in order to combine the various measurements and determine the position of the $(\bar{\rho}, \bar{\eta})$ vertex. The standard analysis of the Unitarity Triangle proposed by the UTfit collaboration[19] make use of the following experimental measurements:

- The CKM matrix elements $|V_{cb}|$ and $|V_{ub}|$ can be measured from the rates of semi-leptonic decays of the B meson in charmed and charmless mesons.
  Several approaches exist to extract the matrix elements that can be divided in two categories:

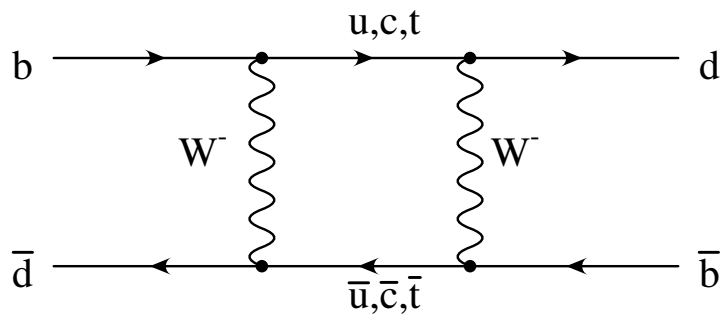

Figure 1.3: Feynman diagram of the second-order weak interaction responsible for the flavor oscillation $\overline{B}^0 \rightarrow B^0$.

the exclusive measurements where single decay channels are considered(such as $B \rightarrow D^* l\nu$ for $|V_{cb}|$ and $B \rightarrow \pi l\nu$ for $|V_{ub}|$), and the inclusive measurements which focus on the inclusive $b \rightarrow cl\nu$ and $b \rightarrow ul\nu$ rates.
From the ratio

$$\frac{|V_{cb}|}{|V_{ub}|} = \frac{\lambda}{1 - \frac{\lambda^2}{2}} \sqrt{\overline{\rho}^2 + \overline{\eta}^2}\,. \tag{1.30}$$

results a constraint in the ($\bar{\rho}$, $\bar{\eta}$) plane that describes a circle centered at (0,0).

- In the Standard Model $B^0\overline{B}^0$ oscillations occur through a second order process (a box diagram) with a loop containing W and up-type quarks. The Feynman diagram for this process is illustrated in figure 1.3. The box diagram with the top quark gives the dominant contribution. The $B^0\overline{B}^0$ oscillation frequency, which is related to the mass difference between the light and the heavy mass eigenstates of the system, is expressed, in the Standard Model, as function of $\bar{\rho}$, $\bar{\eta}$ and other elements of CKM matrix:

$$\Delta m_d \;=\; \frac{G_F^2}{6\pi^2} m_W^2 \; \eta_c S(x_t) \; A^2\lambda^6 \; [(1-\overline{\rho})^2 + \overline{\eta}^2] \; m_{B_d} \; f_{B_d}^2 \hat{B}_{B_d}\;, \tag{1.31}$$

where $S(x_t)$ is Inami-Lim function [20] and $x_t = m_t^2/M_W^2$ (with m_t being the t quark mass in the regularization scheme $\overline{MS}$, $m_t^{\overline{MS}}(m_t^{\overline{MS}})$, and m_W the W boson mass). η_c is the short distance correction now calculated at *next-to-leading* order in perturbative QCD. $f_{B_d}^2 \hat{B}_{B_d}$ is a factor hiding all the non-perturbative effects that contribute to Δm_d. It can be provided by lattice QCD methods. The Δm_d constraint in the ($\bar{\rho}$, $\bar{\eta}$) plane can be represented by a circle centered at(1,0).

- The mixing frequency Δm_s of $B_s\bar{B}_s$ oscillations is usually combined with Δm_d:

$$\frac{\Delta m_d}{\Delta m_s} = \frac{m_{B_d} f_{B_d}^2 \hat{B}_{B_d}}{m_{B_s} f_{B_s}^2 \hat{B}_{B_s}} \left(\frac{\lambda}{1 - \frac{\lambda^2}{2}} \right)^2 \left[(1-\overline{\rho})^2 + \overline{\eta}^2 \right]. \tag{1.32}$$

  This gives again a circle centered at (1,0).

- Indirect CP violation in the Kaon system is usually expressed in terms of ϵ_K parameter which is the fraction of CP violating component in the mass eigenstates. It can be related to the Standard Model parameters by:

$$\epsilon_K = C_\varepsilon \, A^2 \lambda^6 \, \overline{\eta} \left[-\eta_1 S(x_c) + \eta_2 S(x_t) \left(A^2 \lambda^4 \left(1 - \overline{\rho} \right) \right) + \eta_3 S(x_c, x_t) \right] \, \hat{B}_K \, , \tag{1.33}$$

  where

$$C_\varepsilon = \frac{G_F^2 f_K^2 m_K m_W^2}{6\sqrt{2}\pi^2 \Delta m_K} \, . \tag{1.34}$$

  $S(x_i)$ and $S(x_i, x_j)$ again are the Inami-Lim functions [20], being $x_q = m_q^2/m_W^2$ and including NLO corrections [21, 22, 23].f_K is the kaon decay constant and Δm_K the neutral kaon system mixing frequency.

- The mixing induced CP asymmetry, $a_{J/\psi K_{S,L}}$ in the $B_d \to J/\psi K_{S,L}$ decays allows to determine the sine of the angle 2β of the Unitarity Triangle almost without any hadronic uncertainties. In this case the CP asymmetry appears in the interference between amplitudes describing decays with and without mixing. The time dependent asymmetry for $B_d \to J/\psi K_{S,L}$ decays is measured at the B-factories and can be related to $\sin 2\beta$ through:

$$a_{J/\psi K_{S,L}}(\Delta t) = -\eta_{CP} \sin(\Delta m_{B_d} \Delta t) \sin 2\beta. \tag{1.35}$$

The five constraints on the ($\bar{\rho}$, $\bar{\eta}$) plane listed above are showed in figure 1.4, while the result of the combined fit performed by the UTfit [19] collaboration is reported in figure 1.5. The actual estimation found for the Unitarity Triangle vertex is:

$$\begin{aligned} \bar{\rho} &= 0.214 \pm 0.047 \\ \bar{\eta} &= 0.343 \pm 0.028 \end{aligned} \tag{1.36}$$

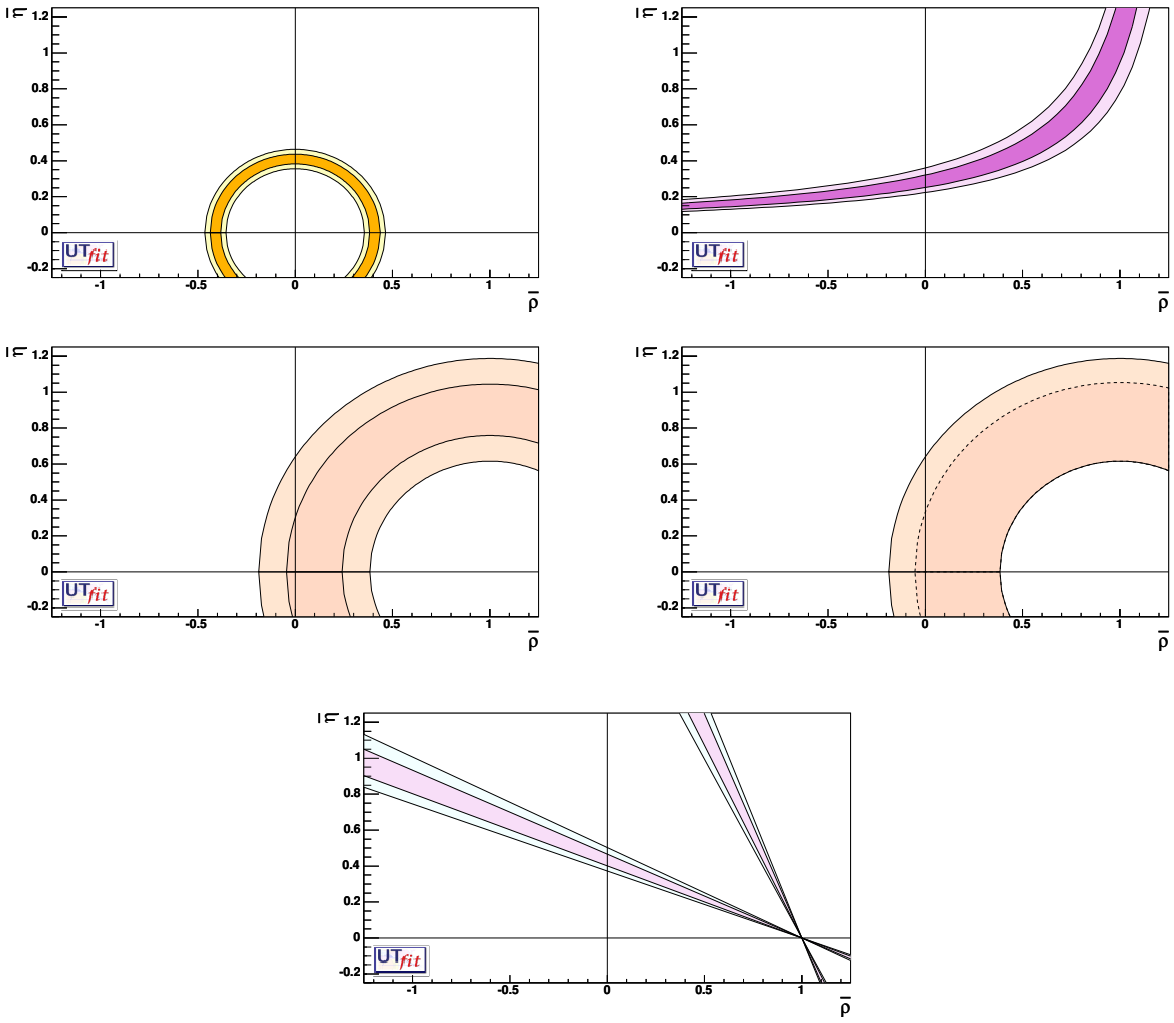

Figure 1.4: Constraints used for the standard analysis by the UTfit collaboration. Starting from the upper left plot they represent respectively the measurements of $|V_{cb}|/|V_{ub}|$, ϵ_K, Δm_d, $\Delta m_d/\Delta m_s$ and $\sin 2\beta$. The two bands represent the allowed regions at 68% and 95% confidence level.

1.4 Time evolution of the B^0 mesons

In the previous section, we have mentioned how the study of the time dependent CP-asymmetry in $B \rightarrow J\psi K_{S,L}$ decays can be used to measure the angle β of the Unitarity Triangle. The same physical principle allows to relate the others angles α and γ to the measurements of the time dependent CP-asymmetries in other B decay channels. In this section we'll see how the CP violation

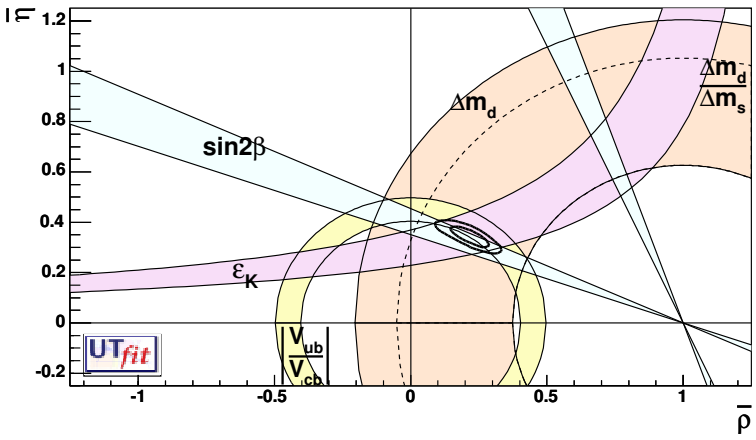

Figure 1.5: Determination of the Unitarity Triangle vertex using the standard analysis. The constraints used (bands at 68% and 95% C.L.) represent the measurements of $|V_{cb}|/|V_{ub}|$, ϵ_K, Δm_d, $\Delta m_d/\Delta m_s$ and $\sin 2\beta$. The results for the vertex coordinates are reported in eq. 1.36.

manifests itself in the interference between B decays with and without mixing. A concrete example will be shown in the next section, where the relation between the angle $2\beta + \gamma$ and the CP asymmetries in $B \rightarrow D^{(*)+}h^-$ (h^- being a $\bar{u}d$ meson) will be discussed.

1.4.1 $B^0\overline{B}^0$ mixing

The neutral B_d mesons contain one b type and one d-type quark (or anti-quark). A description of these systems can be given in terms of different states. There are the flavor eigenstates, with a definite quark content which are relevant in particle production and particle decay processes and there are the Hamiltonian eigenstates, with definite mass and lifetime which are relevant to describe particle propagation through space-time.

The Hamiltonian of the system, in the flavor eigenbasis can be written [24]:

$$H = M - \frac{i}{2}\Gamma, \tag{1.37}$$

where M and Γ are 2×2 Hermitian matrices. CPT invariance guarantees $H_{11} = H_{22}$. An

arbitrary state can be expressed by a linear combination of the neutral B meson flavor eigenstates $B^0 = (\bar{b}, d)$ and $\bar{B}^0 = (b, \bar{d})$:

$$a|B^0\rangle + b|\bar{B}^0\rangle, \tag{1.38}$$

and its evolution is governed by the time-dependent Schrödinger equation

$$i\frac{d}{dt}\begin{pmatrix} a \\ b \end{pmatrix} = H\begin{pmatrix} a \\ b \end{pmatrix} \equiv (M - \frac{i}{2}\Gamma)\begin{pmatrix} a \\ b \end{pmatrix}. \tag{1.39}$$

A perturbative expression for H_{ij} matrix elements ([25]) is:

$$\begin{aligned} M_{ij} &= m_B\delta_{ij} + \langle i|H_W^{\Delta B=2}|j\rangle + \mathcal{P}\sum_n \frac{1}{m_B - E_n}\langle i|H_W^{\Delta B=1}|n\rangle\langle n|H_W^{\Delta B=1}|j\rangle \\ \Gamma_{ij} &= 2\pi\sum_n \delta(E_n - m_B)\langle i|H_W^{\Delta B=1}|n\rangle\langle n|H_W^{\Delta B=1}|i\rangle \end{aligned} \tag{1.40}$$

where $\mathcal{P}$ is the principal part, m_B the B^0 mass, and E_n the energy of the intermediate state $|n\rangle$. As it can be seen, M_{12} and Γ_{12} are the dispersive and absorptive parts respectively of the transition amplitude from B^0 to $\bar{B}^0$ and are therefore particularly relevant in discussing CP violation phenomenology. The states B^0 and $\bar{B}^0$ are related through CP transformation by:

$$CP|B^0\rangle = e^{2i\xi_B}|\bar{B}^0\rangle, \quad CP|\bar{B}^0\rangle = e^{-2i\xi_B}|B^0\rangle, \tag{1.41}$$

where the phase ξ_B is *arbitrary*. The freedom in defining it comes from the fact that flavor conservation (in particular b-flavor) is a symmetry of the strong interactions. This is true for any possible final state f and its CP conjugate $e^{2i\xi_f}\bar{f}$.

The flavor eigenstates are different from the mass eigenstates (as it can be seen computing the eigenvectors of the Hamiltonian), thus they mix up as they propagate in space and time. The light B_L and the heavy B_L mass eigenstates are:

$$|B_L\rangle = p|B^0\rangle + q|\bar{B}^0\rangle, \tag{1.42}$$

$$|B_H\rangle = p|B^0\rangle - q|\bar{B}^0\rangle. \tag{1.43}$$

where the q and p obey the normalization condition

$$|q|^2 + |p|^2 = 1. \tag{1.44}$$

Note that $\arg(q/p^*)$ is just an overall common phase for $|B_L\rangle$ and $|B_H\rangle$ and has no physical significance. The mass and lifetime difference between the two eigenstates are defined as:

$$\Delta m_d \equiv M_H - M_L, \quad \Delta\Gamma_B \equiv \Gamma_H - \Gamma_L. \tag{1.45}$$

Δm_d and $\Delta\Gamma_B$ are related to the Hamiltonian elements by the following relations:

$$(\Delta m_d)^2 - \frac{1}{4}(\Delta\Gamma_B)^2 = 4(|M_{12}|^2 - \frac{1}{4}|\Gamma_{12}|^2), \tag{1.46}$$

$$\Delta m_d \Delta\Gamma_B = 4\Re(M_{12}\Gamma_{12}^*). \tag{1.47}$$

The ratio $\frac{q}{p}$ can be expressed by:

$$\frac{q}{p} = -\frac{\Delta m_d - \frac{i}{2}\Delta\Gamma_B}{2(M_{12} - \frac{i}{2}\Gamma_{12})} = -\frac{2(M_{12}^* - \frac{i}{2}\Gamma_{12}^*)}{\Delta m_d - \frac{i}{2}\Delta\Gamma_B}. \tag{1.48}$$

Experimental data from the B factories allows to assume that:

$$\Delta\Gamma_B \ll \Delta m_d. \tag{1.49}$$

With this assumption, the equations 1.46, 1.47 and 1.48 simplify into

$$\Delta m_d = 2|M_{12}|, \quad \Delta\Gamma_B = 2\Re(M_{12}\Gamma_{12}^*)/|M_{12}|, \tag{1.50}$$

$$q/p = -|M_{12}|/M_{12}. \tag{1.51}$$

Any B state can thus be written as a linear combination of the states B_H and B_L, whose coefficients a_H and a_L evolve in time as:

$$a_H(t) = a_H(0)e^{-iM_H t}e^{-\frac{1}{2}\Gamma_H t}, \quad a_L(t) = a_L(0)e^{-iM_L t}e^{-\frac{1}{2}\Gamma_L t}. \tag{1.52}$$

A state produced at $t = 0$ as a pure B^0, denoted with $|B^0_{\rm phys}\rangle$, has $a_L(0) = a_H(0) = 1/(2p)$ and similarly for a state produced at $t = 0$ as a $\bar{B}^0$. The time evolution is given by:

$$|B^0_{\rm phys}(t)\rangle = g_+(t)|B^0\rangle + (q/p)g_-(t)|\bar{B}^0\rangle, \tag{1.53}$$

$$|\bar{B}^0_{\rm phys}(t)\rangle = (p/q)g_-(t)|B^0\rangle + g_+(t)|\bar{B}^0\rangle, \tag{1.54}$$

where

$$g_+(t) = e^{-iMt}e^{-\Gamma t/2}\cos(\Delta m_d\, t/2), \tag{1.55}$$

$$g_-(t) = e^{-iMt}e^{-\Gamma t/2} i \sin(\Delta m_d\, t/2), \tag{1.56}$$

$M = \frac{1}{2}(M_H + M_L)$ and $\Gamma = \frac{1}{2}(\Gamma_H + \Gamma_L)$. $\tau = \frac{1}{\Gamma}$ is called average lifetime of the B mesons.

From the equations above it can be seen that a B meson produced at $t = 0$ as a B^0 can become a $\bar{B}^0$ and vice-versa (mixing probability). The frequency of the oscillation is the difference of the two mass eigenstates Δm_d which is therefore called the *mixing frequency* of the $B^0\bar{B}^0$ system.

1.4.2 Time evolution at the $\Upsilon(4S)$

In *BABAR*, B mesons are produced in decays of the $\Upsilon(4S)$, which is a $b\bar{b}$ bound state similar to the positronium state. Its mass of $10.58\,\mathrm{GeV}/c^2$ is slightly above the energy threshold for production of two B mesons. About equal amounts of $B^+\,B^-$ and $B^0\,\overline{B}^0$ pair are produced in the $\Upsilon(4S)$ decay. The time evolution of the $B^0\,\overline{B}^0$ pair represents an example of the quantum coherence.

The initial state $|\Upsilon(4S)\rangle$ has spin $S = 1$, and therefore total angular momentum $J = S + L = 1$, and CP eigenvalue $\eta_{CP} = +1$. The decay proceeds through strong interactions and therefore the angular momentum, the beauty quantum number ($b + \bar{b} = 1 - 1 = 0$), and CP must be conserved. The final state is given by the pair of pseudo-scalar B mesons

$$|B^0_{\rm phys}\overline{B}^0_{\rm phys}\rangle = \frac{a}{\sqrt{2}}\,|B_L B_H\rangle + \frac{b}{\sqrt{2}}\,|B_H B_L\rangle\ . \tag{1.57}$$

with the usual normalization condition $|a|^2 + |b|^2 = 1$. The time evolution of $|B^0_{\rm phys}\overline{B}^0_{\rm phys}\rangle$ is given by

$$|B^0_{\rm phys}\overline{B}^0_{\rm phys}; t_1, t_2\rangle = a\ \mathrm{e}^{i\lambda_+ t_1}\mathrm{e}^{i\lambda_- t_2}|B_L B_H\rangle + b\ \mathrm{e}^{i\lambda_- t_1}\mathrm{e}^{i\lambda_+ t_2}|B_H B_L\rangle\ , \tag{1.58}$$

where t_1 and t_2 are the "proper" times of the B mesons.

The Bose–Einstein statistics requires the total wave function $|\Psi\rangle = |\Psi_{\rm flavor}\rangle|\Psi_{\rm space}\rangle$ for this state to be symmetric at all times. Since the B mesons are spin–0 particles, the total spin S is zero, and the total angular momentum J is given by the orbital angular momentum L of the two mesons. Conservation of J requires $L = 1$, and therefore the B mesons are produced in a P-wave, and $|\Psi_{\rm space}\rangle$ is antisymmetric. For the total wave function $|\Psi\rangle$ to be symmetric, it is then necessary to have $a = -b = 1$.

In a thought experiment, and if the lifetime τ_{B^0} was long enough, one could separate the two B mesons and place them at two space-time points separated by a space-like distance so that events

in one point could not influence those in the other. Nevertheless, due to the quantum coherence the decay of one of the two mesons as a B^0 would force the other meson to be necessarily a $\overline{B}^0$. This represents an example of the Einstein-Podolsky-Rosen paradox.

Time dependent CP asymmetries can be measured in events where one of the two B meson (B_{tag}) decays in a flavor eigenstate $f_{\rm tag}$ and the other one (B_{rec}) decays in a finale state f which is accessible to both the B^0 and $\overline{B}^0$ mesons.
The probability of observing the final state $|f\ f_{\rm tag}\rangle$ depends on

- the difference Δt between the decay times $t_{\rm rec}$ and $t_{\rm tag}$,
- decay amplitudes

$$\begin{array}{ll} A_f = \langle f|H|B^0\rangle, & \bar{A}_f = \langle f|H|\overline{B}^0\rangle, \\ A_{tag} = \langle f_{tag}|H|B^0\rangle, & \bar{A}_{tag} = \langle \bar{f}_{tag}|H|\overline{B}^0\rangle, \end{array} \tag{1.59}$$

- oscillation parameter q/p defined in 1.48, and
- flavor of $B_{\rm tag}$ whether $B_{\rm tag} = B^0$ or $B_{\rm tag} = \overline{B}^0$.

From the equations above, is possible to derive the time dependent decay rate distributions f_+ (f_-) for $B \to f$ when $B_{\rm tag}$ is a B^0 ($\overline{B}^0$):

$$f_\pm = \frac{e^{-|\Delta t|/\tau}}{4\tau}\left[1 \pm S_f \sin(\Delta m_d \Delta t) \mp C_f \cos(\Delta m_d \Delta t)\right], \tag{1.60}$$

where

$$S_f = \frac{2\mathcal{I}m\lambda_f}{1+|\lambda_f|^2} \text{ and } C_f = \frac{1-|\lambda_f|^2}{1+|\lambda_f|^2}, \tag{1.61}$$

and

$$\lambda_f \equiv \frac{q}{p}\frac{\bar{A}_f}{A_f}. \tag{1.62}$$

The distributions above are normalized such that $f_+ + f_- = 1$. The coefficient C_f and S_f, can be extracted by fitting the experimental decay rates of eq. 1.60. For suitable choices of the final state f they can be related to the angles of the Unitarity Triangle. Next section shows how the time dependent decay rates in $B \to D^{(*)+}h^-$ decays can be used to extract the $2\beta + \gamma$ angle.

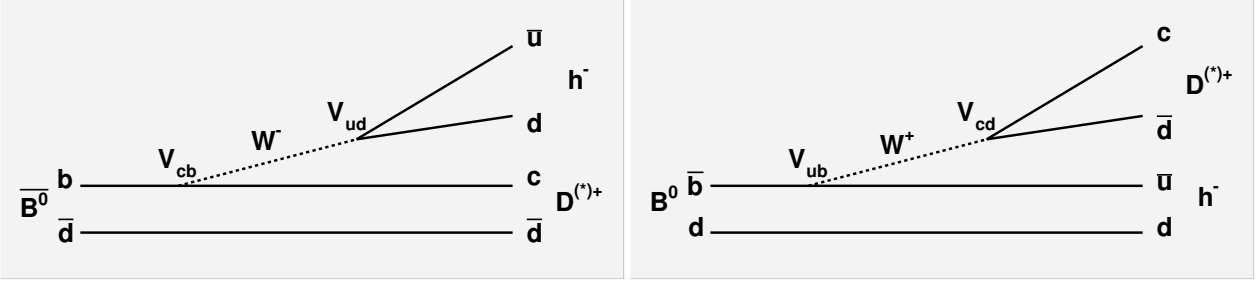

Figure 1.6: Feynman diagrams for the $B \rightarrow D^{(*)+}h^-$ transition. Left: CKM favored amplitude. Right: CKM suppressed amplitude.

1.5 Measurement of $\sin(2\beta+\gamma)$ in the $B \rightarrow D^{(*)}h$ decays

The final states $D^{(*)+}h^-$ (here h^- denotes a light $\bar{u}d$ meson) can be produced from $\overline{B}^0$ decays, via a CKM favored process, and from B^0 decays, via a CKM suppressed diagram. Similarly, the charged conjugate states $D^{(*)-}h^+$ are accessible from both the B^0 (favored) and $\overline{B}^0$ (suppressed) decays. Feynman diagrams for these processes are shown in figure 1.6.

The ratio $\frac{\bar{A}_f}{A_f}$ in the definition of λ_f (equation 1.62) is, for the final states $D^{(*)+}h^-$, given by:

$$\frac{\bar{A}_{D^{(*)+}h^-}}{A_{D^{(*)+}h^-}} = \frac{V_{cb}V_{ud}^*}{V_{cd}V_{ub}^*}\frac{\bar{M}_{D^{(*)+}h^-}}{M_{D^{(*)+}h^-}}, \tag{1.63}$$

where $\bar{M}_{D^{(*)+}h^-}$ and $M_{D^{(*)+}h^-}$ are the matrix hadronic elements for the decays which express the fact that quarks are bound by strong interactions into color neutral hadrons. In the Standard Model, to a good approximation (neglecting CP violation in mixing) the ratio $|\frac{q}{p}|$ can be estimated from the box diagrams shown in Figure 1.3:

$$\frac{q}{p} = -\frac{M_{12}^*}{|M_{12}|} = \frac{V_{tb}^*V_{td}}{V_{tb}V_{td}^*}. \tag{1.64}$$

Combining Equations 1.64 and 1.63 results:

$$\lambda_{D^{(*)+}h^-} = \left(\frac{V_{tb}^*V_{td}}{V_{tb}V_{td}^*}\right)\left(\frac{V_{cb}V_{ud}^*}{V_{cd}V_{ub}^*}\right)\frac{\bar{M}_{D^{(*)+}h^-}}{M_{D^{(*)+}h^-}}. \tag{1.65}$$

Isolating the weak phase, using Equation 1.29 the parameter $\lambda_{D^{(*)+}h^-}$ can be written:

$$\lambda_{D^{(*)+}h^-} = e^{-i(2\beta+\gamma)}\left(\frac{|V_{tb}^*V_{td}|}{|V_{tb}V_{td}^*|}\right)\left(\frac{|V_{cb}V_{ud}^*|}{|V_{cd}V_{ub}^*|}\right)\frac{\bar{M}_{D^{(*)+}h^-}}{M_{D^{(*)+}h^-}}. \tag{1.66}$$

Expliciting the phase of the hadronic matrix elements also leads to:

$$\lambda_{D^{(*)+}h^-} = e^{-i(2\beta+\gamma+\delta)} \left(\frac{|V_{tb}^* V_{td}|}{|V_{tb}V_{td}^*|}\right) \left(\frac{|V_{cb}V_{ud}^*|}{|V_{cd}V_{ub}^*|}\right) \frac{|\bar{M}_{D^{(*)+}h^-}|}{|M_{D^{(*)+}h^-}|}, \tag{1.67}$$

where δ is the strong phase difference between the hadronic matrix elements of the $\bar{B}^0 \to D^{(*)+}h^-$ and $B^0 \to D^{(*)+}h^-$ decays. The relation above becomes, assuming no CP violation in mixing ($\frac{|q|}{|p|} = 1$):

$$\lambda_{D^{(*)+}h^-} = e^{-i(2\beta+\gamma+\delta)} \left(\frac{|V_{cb}V_{ud}^*|}{|V_{cd}V_{ub}^*|}\right) \frac{|\bar{M}_{D^{(*)+}h^-}|}{|M_{D^{(*)+}h^-}|}. \tag{1.68}$$

In the case of $f = D^{(*)-}h^+$ the ratio $\frac{\bar{A}_f}{A_f}$ is:

$$\frac{\bar{A}_{D^{(*)-}h^+}}{A_{D^{(*)-}h^+}} = \frac{V_{ub}V_{cd}^*}{V_{ud}V_{cb}^*} \frac{\bar{M}_{D^{(*)-}h^+}}{M_{D^{(*)-}h^+}}, \tag{1.69}$$

The relations $\bar{M}_f = M_{\bar{f}}$ and $\bar{M}_{\bar{f}} = M_f$ hold (CP conservation in strong interactions) thus the final expression for $\lambda_{D^{(*)-}h^+}$ is:

$$\lambda_{D^{(*)-}h^+} = e^{-i(2\beta+\gamma-\delta)} \left(\frac{|V_{ub}V_{cd}^*|}{|V_{ud}V_{cb}^*|}\right) \frac{|M_{D^{(*)+}h^-}|}{|\bar{M}_{D^{(*)+}h^-}|}, \tag{1.70}$$

In conclusion opposite charge combinations of the particles in the final states have the same weak phase $(2\beta+\gamma)$, $|\lambda|$ one the inverse of the other and difference of strong phase δ appearing with opposite sign. The weak phase is $2\beta+\gamma$ is the same for all the $D^{(*)}h$ final states while δ and $|\lambda|$ depend on the specific process.

Using the results obtained above, is possible to write the time dependent rates of equation 1.60 as:

$$\begin{aligned} f_\pm &= \frac{e^{-|\Delta t|/\tau}}{4\tau(1+|\lambda|^2)}[1 \mp 2|\lambda| sin(2\beta+\gamma-\xi\delta)\sin(\Delta m_d \Delta t) \\ &\mp \xi(1-|\lambda|^2)\cos(\Delta m_d \Delta t)], \end{aligned} \tag{1.71}$$

where -(+) are for B^0 ($\bar{B}^0$) and $\xi = 1$(-1) for $D^{(*+)}h^-(D^{(*-)}h^+)$ final states.

A limit of this method is in the small value of the parameter $|\lambda|$ (~ 0.02) that reduces the sensitivity to the parameter $sin(2\beta+\gamma\pm\delta)$. In fact $sin(2\beta+\gamma\pm\delta)$ appears in the coefficient of $sin(\Delta m\Delta t)$ which is of order 0.04 to be compared to the coefficient of $cos(\Delta m\Delta t)$ which is of order 1. In particular even at high statistics, there is not enough sensitivity for extracting from a fit to the data both $sin(2\beta+\gamma\pm\delta)$ and $|\lambda|$. Thus, the parameter $|\lambda|$ is needed as an external input in the fit and must be measured independently.

The small value of $|\lambda|$ reflects the fact that the decays $B^0 \to D^{(*)+}h^-$ and $\bar{B}^0 \to D^{(*)-}h^+$ are $Cabibbo\ suppressed$ respect to $B^0 \to D^{(*)-}h^+$ and $\bar{B}^0 \to D^{(*)+}h^-$ since they contain the CKM matrix element V_{ub} (λ^3_{cab}, λ_{cab} = sine of the Cabibbo angle = 0.22) as opposed to V_{cb} (λ^2_{cab}). A further suppression is given by the presence of V_{cd} instead of V_{ud} (this is another factor λ_{cab}).
The uncertainty on the measurement of $|\lambda|$, is then propagated on the estimation of $sin(2\beta+\gamma\pm\delta)$.

Note that once $s_\pm = sin(2\beta+\gamma\pm\delta)$ is measured, $2\beta+\gamma$ and δ can be obtained by:

$$sin^2(2\beta+\gamma) = \frac{1}{2}\left[1 + s_+s_- \mp \sqrt{(1-s^+)(1-s^-)}\right] \tag{1.72}$$

$$cos^2(\delta) = \frac{1}{2}\left[1 + s_+s_- \pm \sqrt{(1-s^+)(1-s^-)}\right]. \tag{1.73}$$

As it can be seen, there is an eight-fold ambiguity since for each value of $\sin^2(2\beta+\gamma)$ there are four possible solutions: $(2\beta+\gamma)$, $\pi-(2\beta+\gamma)$, $\pi+(2\beta+\gamma)$ and $2\pi-(2\beta+\gamma)$.

In order to overcome these limits, recently an extension of this method has been proposed [27, 26] for decays where the finale state is a vector-vector (as in $B \to D^*\rho$ decay) or a vector-axial vector (as in $B \to D^*a_1$). In these channels, the use of a more complicated angular-time dependent analysis allows to extract the angle $(2\beta+\gamma)$ without using informations on the doubly Cabibbo suppressed amplitudes and reducing the discrete ambiguities.
The use of $B \to D^*a_1$ to measure $(2\beta+\gamma)$ is discussed in section 3.5.

Chapter 2

BABAR Experiment at PEP-II

2.1 Introduction

The primary goal of the BABAR experiment is the study of CP-violating asymmetries in the decay of neutral B meson. Secondary goals are precision measurement of decays of bottom and charm mesons and of τ leptons, and searches for rare processes accessible because of the high luminosity of PEP II B Factory.

The PEP-II B Factory is an e^+e^- asymmetric collider running at a center of mass energy of 10.58 GeV corresponding to the mass of the $\Upsilon(4S)$ resonance. The electron beam in the High Energy Ring (HER) has 9.0 GeV and the positron beam in the Low Energy Ring (LER) has 3.1 GeV. The $\Upsilon(4S)$ is therefore produced with a Lorentz boost of $\beta\gamma = 0.56$. This boost makes it possible to reconstruct the decay vertices of the two B mesons, to determine their relative decay times Δt, and thus to measure the time dependence of their decay rates, since, without boost, this distance would be too small ($\sim 30\ \mu$) to be measured by any vertex tracker.

The BABAR detector [28] has been optimized to reach the primary goal of the CP asymmetry measurement. This measurement needs the complete reconstruction of a B decay in a CP eigenstate, the flavour identification (tagging) of the non-CP B and a measure of the distance of the two decay vertices. To fulfill these needs, a very good vertex resolution, both transverse and parallel to the beam direction, excellent reconstruction efficiency for charged particles and a very good momentum resolution, efficient electron and muon identification, with low misidentification probabilities

for hadrons, are required.

A longitudinal section of the BABAR detector is shown in Fig. 2.1.The detector innermost part is reserved for the silicon vertex tracker (SVT), then there is the drift chamber (DCH), the Čerenkov light detector (DRC) and the CsI electromagnetic calorimeter (EMC). All those detector subsystems are surrounded by a solenoidal superconductor magnetic field. The iron used for the return flux has been instrumented (IFR) for muons and neutral hadrons, like K_L and neutrons, detection.

The detector geometry is cylindrical in the inner zone and hexagonal in the outermost zone: the central part of the structure is called *barrel* and it's closed forward and backward by *end caps*. The covered polar angle ranges from 350 mrad, in the forward, to 400 mrad in the backward directions (defined with respect to the high energy beam direction). The *BABAR* coordinate system has the z axis along the boost direction (or the beam direction): the y axis is vertical and the x axis is horizontal and goes toward the external part of the ring. In order to maximize the geometrical acceptance for $\Upsilon(4S)$ decays the whole detector is offset, with respect to the beam-beam interaction point (IP), by 0.37 m in the direction of the lower energy beam.

A trigger system is used to separate collisions producing interesting events from those that constitutes the noise, or the background, for instance, beam interactions with residual gas. The trigger system is divided in two consequent levels: the level one trigger ($L1$) is hardware based and is designed to have a maximum output rate of $2\ kHz$ and a maximum time delay of 12 μs, while the other level ($L3$), software based, has a throughput rate limited to $120Hz$ in order to permit an easy storage and processing of collected data.

2.2 PEP-II B Factory

PEP-II is a system consisting of two accumulating asymmetric rings designed in order to operate at a center of mass energy of the $\Upsilon(4S)$ resonance mass, 10.58 GeV. Tab. 2.1 shows the various subsystems parameters: a comparison between typical and design values is presented. As can be seen from the table, PEP-II parameters have overcome the project ones in terms of instant luminosity and daily integrated luminosity achieving recently the peak value of $1.0 \times 10^{33}\ cm^{-2}\ s^{-1}$ with a daily integrated luminosity of $700\ pb^{-1}$.

Data is mostly collected at $\Upsilon(4S)$ peak energy. Tab. 2.2 shows the active processes cross sections

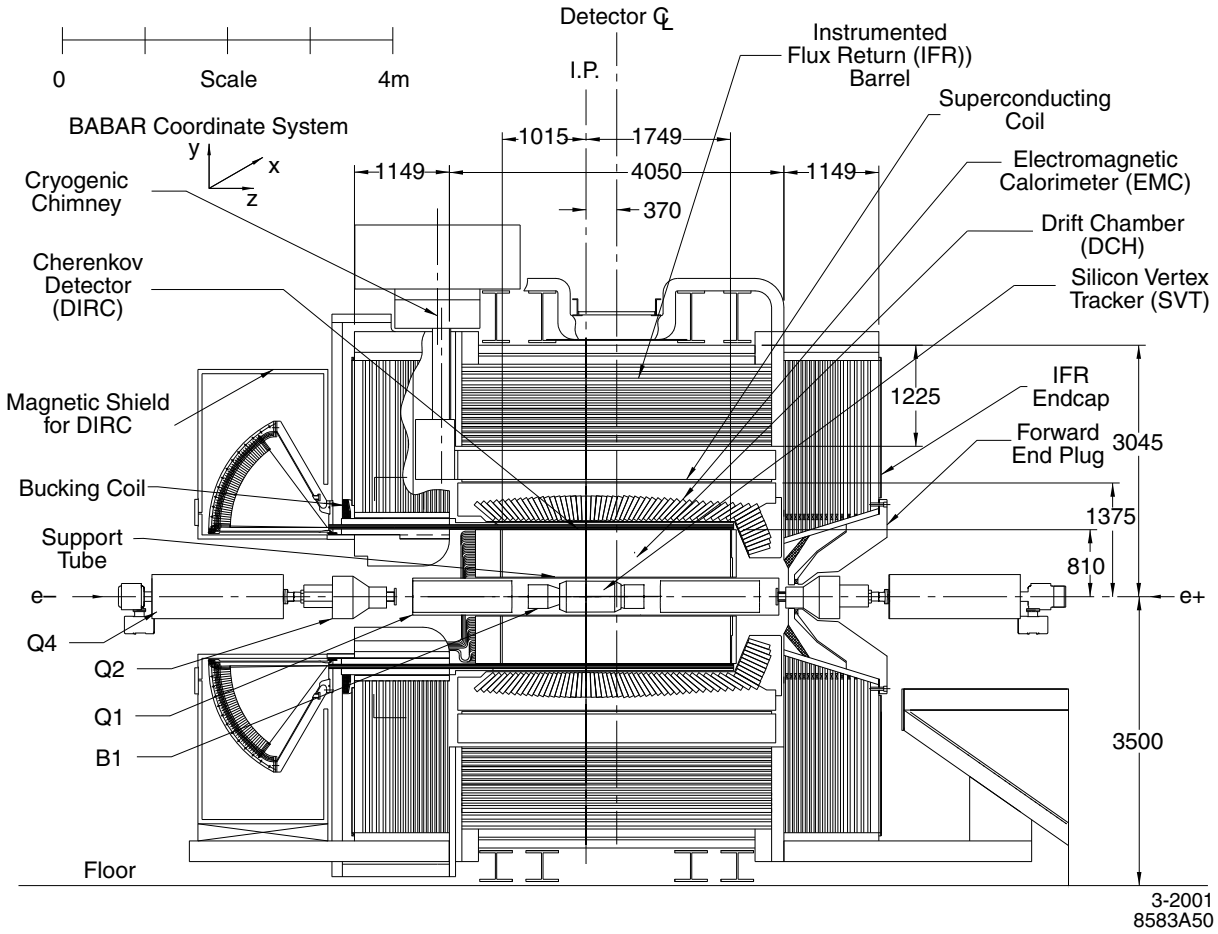

Figure 2.1: BABAR detector longitudinal section.

Parameters	Design	Typical
Energy HER/LER (GeV)	9.0/3.1	9.0/3.1
Current HER/LER (A)	0.75/2.15	1.48/2.5
# of bunch	1658	553-829
bunch time separation (ns)	4.2	6.3-10.5
σ_{Lx} (μm)	110	120
σ_{Ly} (μm)	3.3	5.6
σ_{Lz} (μm)	9000	9000
Luminosity (10^{33} $cm^{-2}s^{-1}$)	3	9
Daily average integrated luminosity (pb^{-1}/d)	135	700

Table 2.1: *PEP-II beam parameters. Design and typical values are quoted and are referred to the fourth year of machine running.*

breakdown at peak energy. From now on the production of light quark pairs (u, d, s) and $charm$ quark pairs will be referred to as "continuum production". In order to study this non-resonant production $\sim 12\%$ of data is collected with a center of mass energy 40 MeV below the $\Upsilon(4S)$ mass value.

PEP-II measures radiative Bhabha scattering to provide a luminosity fast monitor useful for operations. *BABAR* derives the absolute luminosity offline from other QED processes, mainly e^+e^- and $\mu^+\mu^-$ pairs: the systematic uncertainty on the absolute value of the luminosity is estimated to be about 1.5%. This error is dominated by uncertainties in the MonteCarlo generator and the simulation of the detector.

The energies of the two beams are calculated from the total magnetic bending strength and the average deviations of the accelerating frequencies from their central values. The systematic error on the PEP-II calculation of the absolute beam energies is estimated to be $5 - 10$ MeV, while the relative energy setting for each beam is accurate and stable to about 1 MeV.

The interaction region design, with the two beams crossing in a single interaction point with particles trajectories modified in order to have head on collisions, is realized with a magnetic field, produced by a dipole magnetic system, acting near the interaction point. The collision axis is offset from the z-axis of the *BABAR* detector by about 20 mrad in the horizontal plane to minimize the perturbation of the beams by the solenoidal field. In this configuration the particles and the beams

$e^+e^- \rightarrow$	Cross section (nb)
$b\bar{b}$	1.05
$c\bar{c}$	1.30
$s\bar{s}$	0.35
$u\bar{u}$	1.39
$d\bar{d}$	0.35
$\tau^+\tau^-$	0.94
$\mu^+\mu^-$	1.16
e^+e^-	~ 40

Table 2.2: *Various processes cross sections at $\sqrt{s} = M_{\Upsilon(4S)}$. $Bhabha$ cross section is an effective cross section, within the experimental acceptance.*

are kept far apart in the horizontal plane outside the interaction region and parassite collisions are minimized. Magnetic quadrupoles included inside the detector's magnetic field, and hence realized in Samarium-Cobalt, are strongly focusing the beams inside the interaction region.

In order to keep track of PEP-II beams displacement with respect to the *BABAR* detector, the interaction point position is computed on periodic intervals, using two tracks events. Interaction region dimensions (beam-spot) computed in that way are $\sim 150\ \mu m$ along x, $\sim 50\ \mu m$ along y and $1\ cm$ along z axis. The y dimension estimate is completely dominated by tracking resolution and can be improved by looking at luminosity variations as a function of relative beams position. In particular, knowing the beam currents and the x beam-spot dimension, it is possible to get a resolution on y $(\sigma_y) \sim 5\ \mu m$, value that remain stable within 10% in a one hour time scale. Those measurements can be also verified offline by measuring multi hadrons events primary vertexes[1].

Fig. 2.2 shows the integrated luminosity obtained by PEP-II and collected by *BABAR* from the beginning of data taking (November 1999) to the end of September 2005.

[1]By reconstructing all the tracks in one event it is possible to have an estimate of primary vertex position: $\Upsilon(4S)$ decay point in transversal plane. Given that the boost along the z axis produces a relative displacement of the two B mesons this method has a relative poor resolution that get worse in presence of long-lived particles.

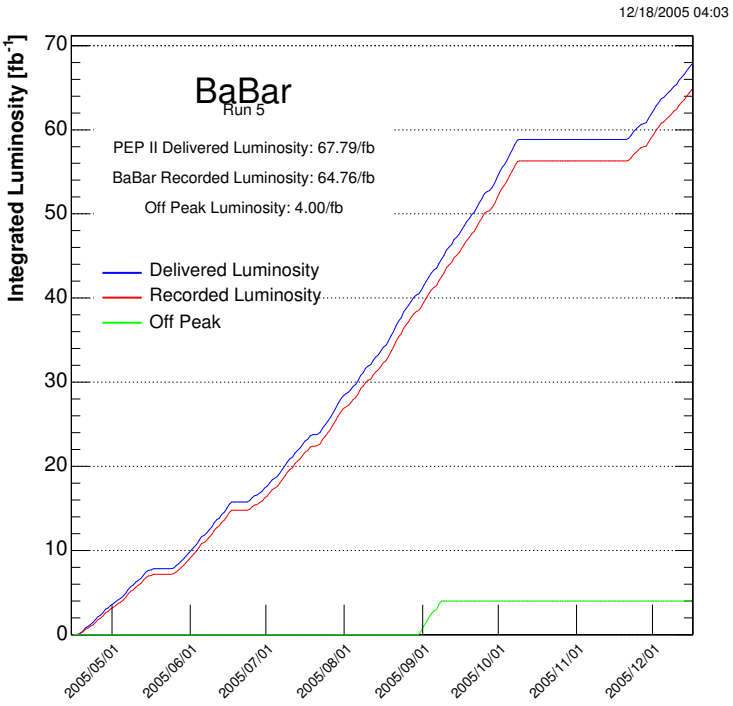

Figure 2.2: Integrated luminosity obtained by PEP-II and collected by *BABAR* from 1999 to September 2005.

2.3 Tracking system

The charged particle tracking system consists of two different components: the silicon vertex tracker (SVT) and the drift chamber (DCH): the main purpose of this tracking system is the efficient detection of charged particles and the measurement of their momentum and angles with high precision. These track measurements are important for the extrapolation to the DIRC, the EMC and the IFR: at lower momenta, the DCH measurements are more important while at higher momenta the SVT dominates.

2.3.1 The Silicon Vertex Tracker: SVT.

The vertex detector has a radius of $20\,cm$ from the primary interaction region: it is placed inside the support tube of the beam magnets and consists of five layers of double-sided silicon strip sensors detectors to provide five measurements of the positions of all charged particles with polar angles in the region $20.1^\circ < \theta < 150^\circ$. Because of the presence of a $1.5\,T$ magnetic field, the charged particle tracks with transverse momenta lower than $\sim 100\ \mathrm{MeV}/c$ cannot reach the drift chamber active volume. So the SVT has to provide stand-alone tracking for particles with transverse momentum less than $120\ \mathrm{MeV}/c$, the minimum that can be measured reliably in the DCH alone: this feature is essential for the identification of slow pions from D^*-meson decays. Because of these, the SVT has to provide redundant measurements.

Beyond the stand-alone tracking capability, the SVT provides the best measurement of track angles which is required to achieve design resolution for the Čerenkov angle for high momentum tracks. The SVT is very close to the production vertex in order to provide a very precise measure of points on the charged particles trajectories on both longitudinal (z) and transverse directions. The longitudinal coordinate information is necessary to measure the decay vertex distance, while the transverse information allows a better separation between secondary vertices coming from decay cascades.

More precisely, the design of the SVT was carried out according to some important guidelines:

- The number of impact points of a single charged particle has to be greater than 3 to make a stand-alone tracking possible, and to provide an independent momentum measure.

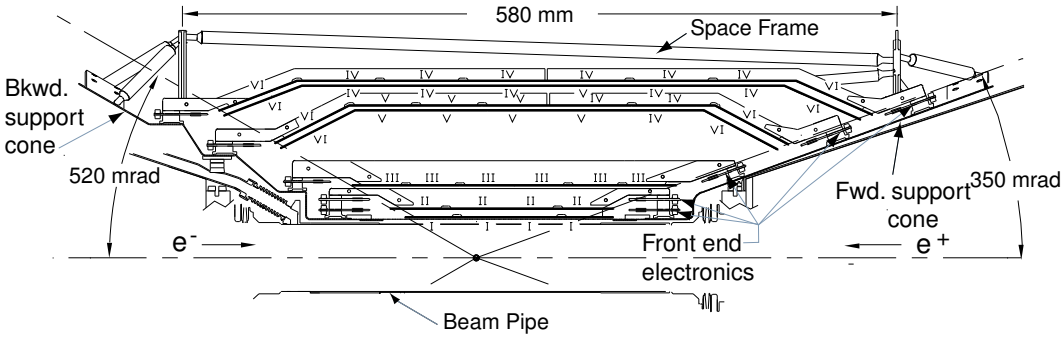

Figure 2.3: SVT schematic view: longitudinal section

- The first three layers are placed as close as possible to the impact point to achieve the best resolution on the z position of the B meson decay vertices.
- The two outer layers are close to each other, but comparatively far from the inner layers, to allow a good measurement of the track angles.
- The SVT must withstand 2 MRad of ionizing radiation: the expected radiation dose is 1 Rad/day in the horizontal plane immediately outside the beam pipe and 0.1 Rad/day on average.
- Since the vertex detector is inaccessible during normal detector operations, it has to be reliable and robust.

These guidelines have led to the choice of a SVT made of five layers of double-sided silicon strip sensors: the spatial resolution, for perpendicular tracks must be $10 - 15\,\mu m$ in the three inner layers and about $40\,\mu m$ in the two outer layers. The three inner layers perform the impact parameter measurement, while the outer layers are necessary for pattern recognition and low p_t tracking. The silicon detectors are double-sided (contain active strips on both sides) because this technology reduces the thickness of the materials the particles have to cross, thus reducing the energy loss and multiple scattering probability compared to single-sided detectors. The sensors are organized in modules (Fig. 2.3). The SVT five layers contain 340 silicon strip detectors with AC-coupled silicon strips.

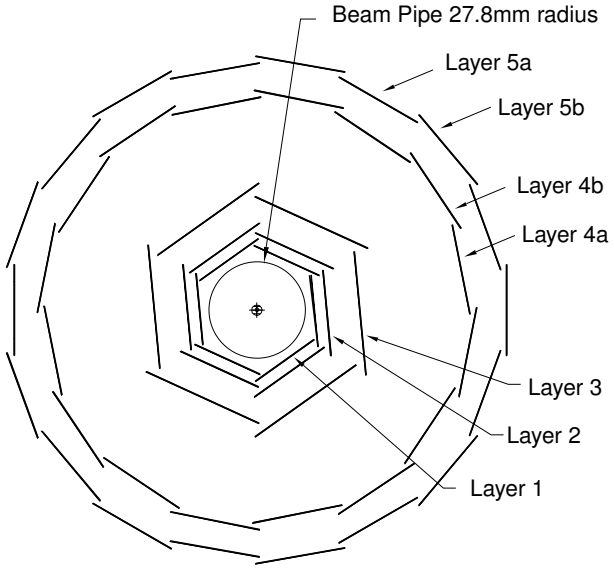

Figure 2.4: Cross-sectional view of the SVT in a plane perpendicular to the beam axis.

Each detector is $300\,\mu m$-thick but sides range from $41\,mm$ to $71\,mm$ and there are 6 different detector types. Each of the three inner layers has a hexagonal transverse cross-section and it is made up of 6 detector modules, arrayed azimuthally around the beam pipe, while the outer two layers consist of 16 and 18 detector modules, respectively. The inner detector modules are barrel-style structures, while the outer detector modules employ the novel arch structure in which the detectors are electrically connected across an angle. This arch design was chosen to minimize the amount of silicon required to cover the solid angle while increasing the solid angle for particles near the edges of acceptance: having incidence angles on the detector closer to 90 degrees at small dip angles insures a better resolution on impact points. One of the main features of the SVT design is the mounting of the readout electronics entirely outside the active detector volume.

The strips on the two sides of the rectangular detectors in the barrel regions are oriented parallel (ϕ strips) or perpendicular (z strips) to the beam line: in other words, the inner sides of the detectors have strips oriented perpendicular to the beam direction to measure the z coordinate (z-size), whereas the outer sides, with longitudinal strips, allow the ϕ-coordinate measurement (ϕ-side). In the forward and backward regions of the two outer layers, the angle between the strips on the two sides of the trapezoidal detectors is approximately 90° and the ϕ strips are tapered.

The inner modules are tilted in ϕ by 5°, allowing an overlap region between adjacent modules: this

provide full azimuthal coverage and is convenient for alignment. The outer modules are not tilted, but are divided into sub-layers and placed at slightly different radii (see Fig. 2.4).

The total silicon area in the SVT is $0.94\,m^2$ and the number of readout channels is about $150\,000$. The geometrical acceptance of SVT is 90% of the solid angle in the c.m. system and typically 80% are used in charged particle tracking.

The z-side strips are connected to the read-out electronics with flexible *Upilex* fanout circuits glued to the inner faces of half-modules: as a matter of fact, each module is divided into two electrically separated forward and backward half-modules. The fanout circuits consist of conductive traces on a thin flexible insulator (copper traces on Kapton): the traces are wire-bonded to the end of the strips.

In the two outer layers, in each module the number of z strips exceeds the number of read-out channels, so that a fraction of the strips is "ganged", i.e., two strips are connected to the same read-out channel. The "ganging" is performed by the fanout circuits. The length of a z strip is about $50\,\mu m$ (case of no ganging) or $100\,\mu m$ (case of two strip connected): the ganging introduces an ambiguity on the z coordinate measurement, which must be resolved by the pattern recognition algorithms. The ϕ strips are daisy-chained between detectors, resulting in a total strip length of up to $26\,cm$. Also, for the ϕ-side, a short fanout extension is needed to connect the ends of the strips to the read-out electronics.

Table 2.3: Parameters of the SVT layout: these characteristics are shown for each layer.

	1st layer	2nd layer	3rd layer	4th layer	5th layer
radius (mm)	32	40	54	91-127	114-144
modules/layer	6	6	6	16	18
wafers/module	4	4	6	7	8
read-out pitch (μm)					
ϕ	50-100	55-110	55-110	100	100
z	100	100	100	210	210

The signals from the read-out strips are processed using a new technique, bringing in several

advantages. After amplification and shaping, the signals are compared to a preset threshold and the time they exceed this threshold (time over threshold, or ToT) is measured. This time interval is related to the charge induced in the strip by the charged particle crossing it. Unlike the traditional peak-amplitude measurement in the shaper output, the ToT has the advantage of an approximately logarithmic relation of the time interval to the charge signal. This compresses the active dynamic range of the signal, ensuring a good sensitivity in the lower range. When a particle crosses a silicon detector a cluster of adjoining strips producing a signal is formed. The good signal resolution in the lower range ensures a good determination of the tails of the cluster thus improving the resolution on the impact point measurement.

The electronic noise measured is found to vary between 700 and 1500 electrons ENC (equivalent noise charge), depending on the layer and the readout view: this can be compared to the typical energy deposition for a minimum ionizing particle at normal incidence, which is equivalent to ~ 24000 electrons.

During normal running conditions, the average occupancy of the SVT in a time window of $1\,\mu s$ is about 2% for the inner layers, where it is dominated by machine backgrounds, and less than 1% for the outer layers, where noise hits dominate.

The cluster reconstruction is based on a cluster finding algorithm: first the charge pulse height of a single pulse is calculated form the ToT value and clusters are formed grouping adjacent strips with consistent times. The position x of a cluster formed by n strips is evaluated with an algorithm called "head-to-tail" algorithm:

$$x = \frac{(x_1 + x_n)}{2} + \frac{p}{2}\frac{(Q_n - Q_1)}{(Q_n + Q_1)}$$

where x_i and Q_i are the position and the collected charge of i-th strip and p is the read-out pitch. This formula always gives a cluster position within $p/2$ of the geometrical center of the cluster. The cluster pulse height is simply the sum of the strip charges, while the cluster time is the average of the signal times.

The SVT efficiency can be calculated for each half-module by comparing the number of associated hits to the number of tracks crossing the active area of the half-module. Excluding defective readout sections (9 over 208), the combined hardware and software efficiency is 97%.

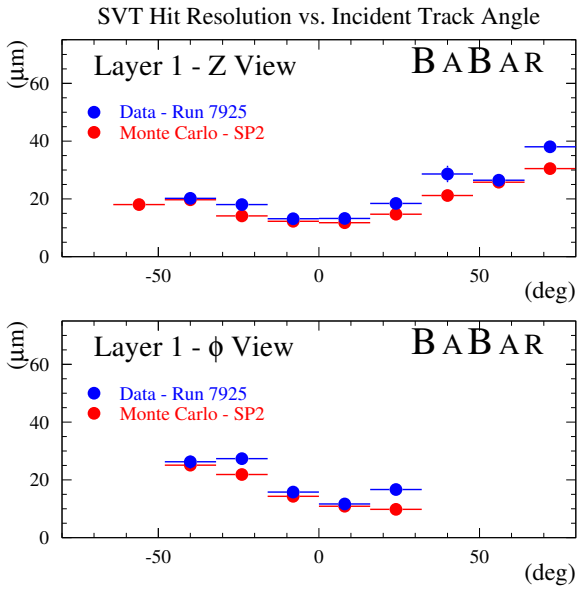

Figure 2.5: *SVT hit resolution in the z and ϕ coordinate in microns, plotted as functions of the track incident angle in degrees.*

The spatial resolution of SVT hits is calculated by measuring the distance (in the plane of the sensor) between the track trajectory and the hit, using high-momentum tracks in two prong events: the uncertainty due to the track trajectory is subtracted from the width of the residual distribution to obtain the hit resolution. The track hit residuals are defined as the distance between track and hit, projected onto the wafer plane and along either the ϕ or z direction. The width of this residual distribution is then the SVT hit resolution. Fig. 2.5 shows the SVT hit resolution for z and ϕ side hits as a function of the track incident angle: the measured resolutions are in very good agreement with the MonteCarlo expected ones. Over the whole SVT, resolutions are raging from $10-15\,\mu m$ (inner layers) to $30-40\,\mu m$ (outer layers) for normal tracks.

For low-momentum tracks ($p_t < 120$ MeV/c), the SVT provides the only particle identification information. The measure of the ToT value enables to obtain the pulse height and hence the ionization dE/dx: the value of ToT are converted to pulse height using a look-up table computed from the pulse shapes. The double-sided sensors provide up to ten measurements of dE/dx per track: with signals from at least four sensors, a 60% truncated mean dE/dx is calculated. For MIPs, the resolution on the truncated mean dE/dx is approximately 14%: a 2σ separation between

kaons and pions can be achieved up to momentum of 500 MeV/c and between kaons and protons beyond 1 GeV/c.

2.3.2 The drift chamber: DCH.

The drift chamber is the second part of *BABAR* tracking system: its principal purpose is the efficient detection of charged particles and the measurement of their momenta and angles with high precision. The DCH complements the measurements of the impact parameter and the directions of charged tracks provided by the SVT near the impact point (IP). At lower momenta, the DCH measurements dominate the errors on the extrapolation of charged tracks to the DIRC, EMC and IFR. The reconstruction of decay and interaction vertices outside of the SVT volume, for instance the K^0_S decays, relies only on the DCH. For these reasons, the chamber should provide maximal solid angle coverage, good measurement of the transverse momenta and positions but also of the longitudinal positions of tracks with a resolution of $\sim 1\,mm$, efficient reconstruction of tracks at momenta as low as 100 MeV/c and it has to minimally degrade the performance of the calorimeter and particle identification devices (the most external detectors). The DCH also needs to supply information for the charged particle trigger. For low momentum particles, the DCH is required to provide particle identification by measuring the ionization loss (dE/dx). A resolution of about 7% allows π/K separation up to 700 MeV/c. This particle identification (PID) measurement is complementary to that of the DIRC in the barrel region, while in the extreme backward and forward region, the DCH is the only device providing some discrimination of particles of different mass. The DCH should also be able to operate in presence of large beam-generated backgrounds having expected rates of about $5\,kHz$/cell in the innermost layers.

To meet the above requirements, the DCH is a $280\,cm$-long cylinder (see left plot in Fig. 2.6), with an inner radius of $23.6\,cm$ and an outer radius of $80.9\,cm$: it is bounded by the support tube at its inner radius and the particle identification device at its outer radius. The flat end-plates are made of aluminum: since the *BABAR* events will be boosted in the forward direction, the design of the detector is optimized to reduce the material in the forward end. The forward end-plate is made thinner ($12\,mm$) in the acceptance region of the detector compared to the rear end-plate ($24\,mm$), and all the electronics is mounted on the rear end-plate. The device is asymmetrically located with respect to the IP: the forward length of 174.9 cm is chosen so that particles emitted at polar angles of 17.2° traverse at least half of the layers of the chamber before exiting through the front

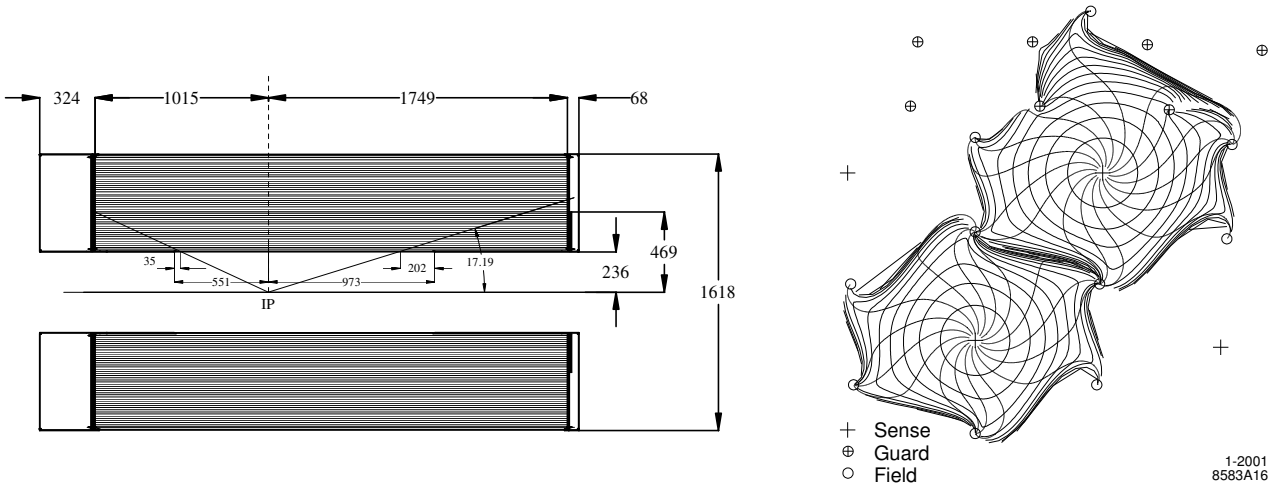

Figure 2.6: Side view of the *BABAR* drift chamber (the dimensions are in mm) and isochrones (i.e. contours of equal drift time of ions) in cells of layer 3 and 4 of an axial super-layer. The isochrones are spaced by $100\,ns$.

end-plate. In the backward direction, the length of 101.5 cm means that particles with polar angles down to 152.6° traverse at least half of the layers.

The inner cylinder is made of $1\,mm$ beryllium and the outer cylinder consists of two layers of carbon fiber glued on a Nomex core: the inner cylindrical wall is kept thin to facilitate the matching of SVT and DCH tracks, to improve the track resolution for high momentum tracks and to minimize the background from photon conversions and interactions. Material in the outer wall and in the forward direction is also minimized in order not to degrade the performance of the DIRC and the EMC.

The region between the two cylinders is filled up by a gas mixture consisting of Helium-isobutane ($80\% : 20\%$): the chosen mixture has a radiation length that is five times larger than commonly used argon-based gases. 40 layers of wires fill the DCH volume and form 7104 hexagonal cells with typical dimensions of $1.2 \times 1.9\,cm^2$ along the radial and azimuthal directions, respectively (see right plot in Fig. 2.6). The hexagonal cell configuration has been chosen because approximate circular symmetry can be achieved over a large portion of the cell. Each cell consist of one sense wire surrounded by six field wires: the sense wires are $20\,\mu m$ gold-plated tungsten-rhenium, the field wires are $120\,\mu m$ and $80\,\mu m$ gold-plated aluminum. By using the low-mass aluminum field wires and the helium-based gas mixture, the multiple scattering inside the DCH is reduced to a

minimum, representing less than $0.2\% X_0$ of material. The total thickness of the DCH at normal incidence is $1.08\% X_0$.

The drift cells are arranged in 10 super-layers of 4 cylindrical layers each: the super-layers contain wires oriented in the same direction: to measure the z coordinate, axial wire super-layers and super-layers with slightly rotated wires (*stereo*) are alternated. In the stereo super-layers a single wire corresponds to different ϕ angles and the z coordinate is determined by comparing the ϕ measurements from axial wires and the measurements from rotated wires. The stereo angles vary between ± 45 mrad and ± 76 mrad.

While the field wires are at ground potential, a positive high voltage is applied to the sense wires: an avalanche gain of approximately 5×10^4 is obtained at a typical operating voltage of $1960\, V$ and a $80:20$ helium:isobutane gas mixture.

In each cell, the track reconstruction is obtained by the electron time of flight: the precise relation between the measured drift time and drift distance is determined from sample of e^+e^- and $\mu^+\mu^-$ events. For each signal, the drift distance is estimated by computing the distance of closest approach between the track and the wire. To avoid bias, the fit does not include the hit of the wire under consideration. The estimated drift distances and the measured drift times are averaged over all wires in a layer.

The DCH expected position resolution is lower than $100\, \mu m$ in the transverse plane, while it is about $1\, mm$ in the z direction. The minimum reconstruction and momentum measure threshold is about 100 MeV/c and it is limited by the DCH inner radius. The design resolution on the single hit is about $140\, \mu m$ while the achieved weighted average resolution is about $125\, \mu m$. Left plot in Fig. 2.7 shows the position resolution as a function of the drift distance, separately for the left and the right side of the sense wire. The resolution is taken from Gaussian fits to the distributions of residuals obtained from unbiased track fits: the results are based on multi-hadron events for data averaged over all cells in layer 18.

The specific energy loss (dE/dx) for charged particles through the DCH is derived from the measurement of the total charge collected in each drift cell: the specific energy loss per track is computed as a truncated mean from the lowest 80% of the individual dE/dx measurements. Various corrections are applied to remove sources of bias: these corrections include changes in gas pressure and temperature ($\pm 9\%$ in dE/dx), differences in cell geometry and charge collection

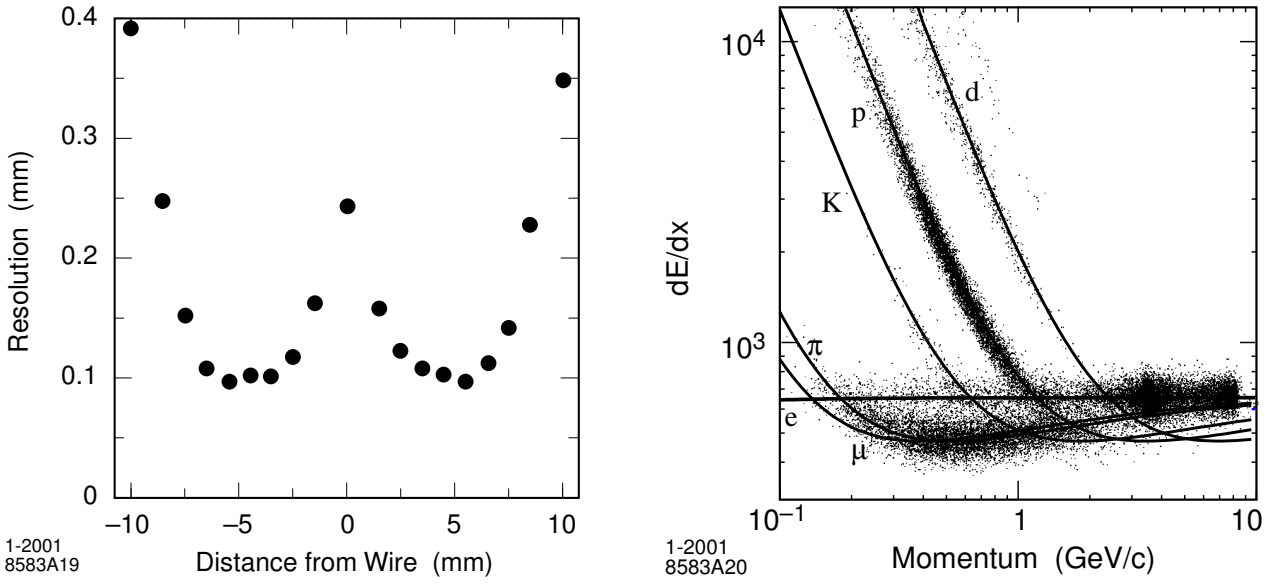

Figure 2.7: Left plot: DCH position resolution as a function of the drift chamber in layer 18, for tracks on the left and right side of the sense wire. The data are averaged over all cells in the layer. Right plot: measurement of dE/dx in the DCH as a function of the track momenta. The data include large samples of beam background triggers as evident from the high rate of protons. The curves show the Bethe-Bloch predictions derived from selected control samples of particles of different masses.

($\pm 8\%$), signal saturation due to space charge buildup ($\pm 11\%$), non-linearities in the most probable energy loss at large dip angles ($\pm 2.5\%$) and variation of cell charge collection as a function of the entrance angle ($\pm 2.5\%$).

Right plot in Fig. 2.7 shows the distribution of the corrected dE/dx measurements as a function of track momenta: the superimposed Bethe-Bloch predictions have been determined from selected control samples of particles of different masses. The achieved dE/dx rms resolution for Bhabha events is typically 7.5%, limited by the number of samples and Landau fluctuations, and it is close to the expected resolution of 7%.

2.3.3 The charged particle tracking system.

As already said, the *BABAR* tracking system is based on SVT and DCH detectors: charged particle tracking has been studied with large samples of cosmic ray muons, e^+e^-, $\mu^+\mu^-$ and $\tau^+\tau^-$ events, as well as multi-hadrons.

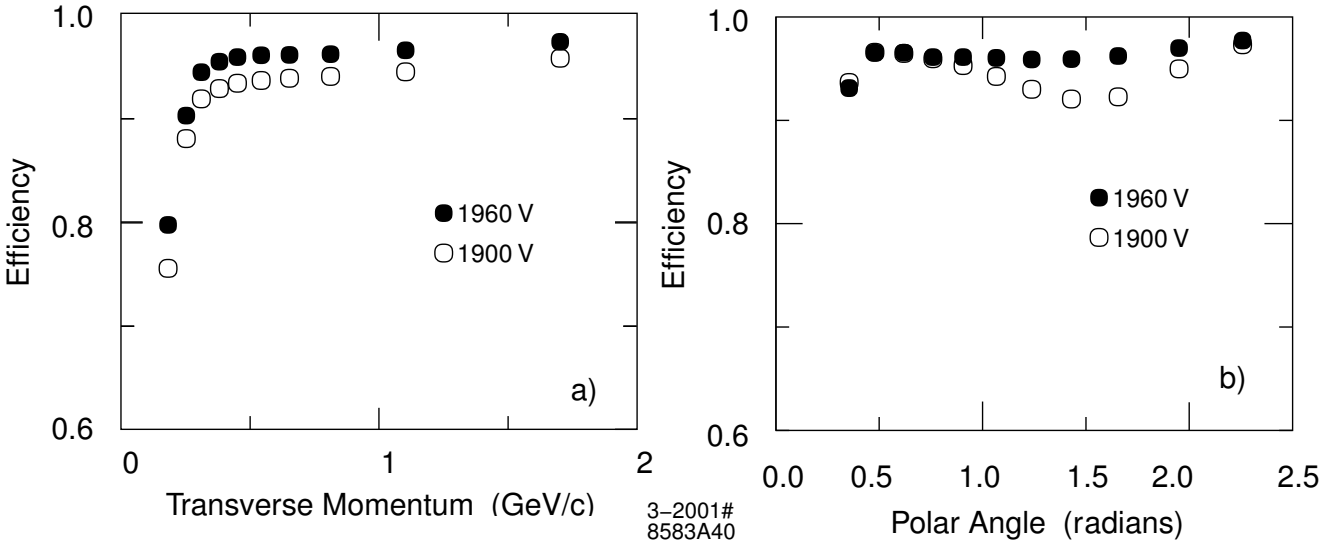

Figure 2.8: Track reconstruction efficiency in the DCH at operating voltages of $1960\,V$ and $1900\,V$ as a function of transverse momentum (left plot) and of polar angle (right plot). The efficiency is measured in multi-hadron events.

Charged tracks are defined by five parameters (d_0, ϕ_0, ω, z_0 and $\tan\lambda$) and their associated error matrix: these parameters are measured at the point of closest approach to the z-axis and d_0 and z_0 are the distances of this point from the origin of the coordinate system (in the $x-y$ plane and on the z axix, respectively). The angle ϕ_0 is the azimuth of the track, λ is the dip angle relative to the transverse plane and ω is the curvature. d_0 and ω have signs that depend on the particle charge.

The track finding and the fitting procedure make use of the Kalman filter algorithm that takes into account the detailed description of material in the detector and the full map of the magnetic field. First of all, tracks are reconstructed with DCH hits through a stand-alone DCH algorithm: the resulting tracks are then extrapolated into the SVT and SVT track segments are added and a Kalman fit is performed to the full set of DCH and SVT hits. Any remaining SVT hits are then passed to the SVT stand-alone track finding algorithms. Finally, an attempt is made to combine

tracks that are only found by one of the two tracking systems and thus recover tracks scattered in the material of the support tube.

The efficiency for track reconstruction in the DCH has been measured as a function of transverse momentum, polar and azimuthal angles in multi-track events. These measurement rely on specific final states and exploit the fact that the track reconstruction can be performed independently in the SVT and the DCH. The absolute DCH tracking efficiency is determined as the ratio of the number of reconstructed DCH tracks to the number of tracks detected in the SVT with the requirement that they fall within the acceptance of the DCH. Left plot in Fig. 2.8 shows the efficiency in the DCH as a function of transverse momentum in multi-hadron events.

At design voltage of $1960\,V$, the efficiency averages $98 \pm 1\%$ per track above 200 MeV/c: the data recorded at $1900\,V$ show a reduction in efficiency by about 5% for tracks almost at normal incidence, indicating that the cells are not fully efficient at this voltage (see right plot in Fig. 2.8).

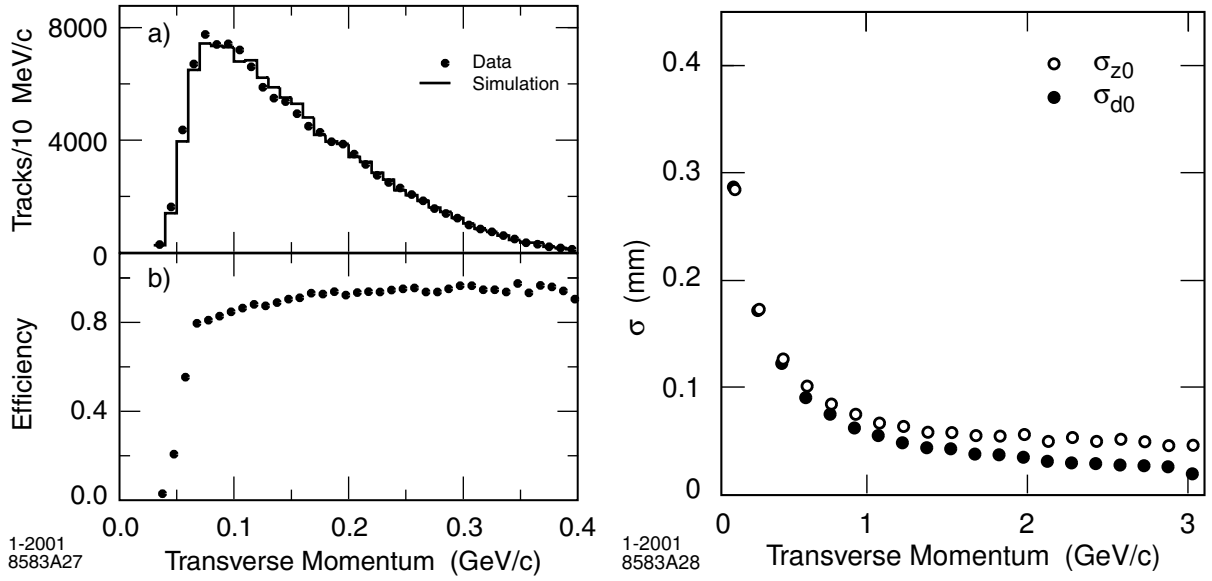

Figure 2.9: Left plot: MonteCarlo studies of low momentum tracks in the SVT on $D^{*+} \to D^0\pi^+$ events. a) comparison with data in $B\bar{B}$ events and b) efficiency for slow pion detection derived from simulated events. Right plot: resolution in the parameters d_0 and z_0 for tracks in multi-hadron events as a function of the transverse momentum.

The stand-alone SVT tracking algorithms have a high efficiency for tracks with low transverse momentum: to estimate the tracking efficiency for these low momentum tracks, a detailed Monte-

Carlo study was performed. The pion spectrum was derived from simulation of the inclusive D^* production in $B\bar{B}$ events and MonteCarlo events were selected in the same way as the data: since the agreement with MonteCarlo is very good, the detection efficiency has been derived from MonteCarlo simulation. The SVT extends the capability of the charge particle reconstruction down to transverse momenta of ~ 50 MeV/c (see left plot in Fig. 2.9).

The resolution in the five track parameters is monitored using e^+e^- and $\mu^+\mu^-$ pair events: the resolution is derived from the difference of the measured parameters for the upper and lower halves of the cosmic ray tracks traversing the DCH and the SVT. On this sample with transverse momenta above 3 GeV/c, the resolution for single tracks is $23\,\mu m$ in d_0 and $29\,\mu m$ in z_0. To study the dependence of resolution from transverse momentum, a sample of multi-hadron events is used: the resolution is determined from the width of the distribution of the difference between the measured parameters (d_0 and z_0) and the coordinates of the vertex reconstructed from the remaining tracks in the event: right plot in Fig. 2.9 shows the dependence of the resolution in d_0 and z_0 as a function of p_t. The measured resolutions are about $25\,\mu m$ in d_0 and $40\,\mu m$ in z_0 for p_t of 3 GeV/c: these values are in good agreement with the MonteCarlo studies and in reasonable agreement also with the results from cosmic rays.

2.4 Čerenkov **light detector:** *DIRC*

The particle identification system is crucial for *BABAR* since the CP violation analysis requires the ability to fully reconstruct one of the B meson and to tag the flavour of the other B decay: the momenta of the kaons used for flavour tagging extend up to about 2 GeV/c with most of them below 1 GeV/c. On the other hand, pions and kaons from the rare two-body decays $B^0 \to \pi^+\pi^-$ and $B^0 \to K^+\pi^-$ must be well separated: they have momenta between 1.7 and 4.2 GeV/c with a strong momentum-polar angle correlation of the tracks (higher momenta occur at more forward angles because of the c.m. system boost). So the particle identification system should be:

- thin and uniform in term of radiation lengths to minimize degradation of the calorimeter energy resolution,
- small in the radial dimension to reduce the volume (cost) of the calorimeter,
- with fast signal response,

- able to tolerate high background.

DIRC stands for Detection of Internally Reflected Čerenkov light and it refers to a new kind of ring-imaging Čerenkov detector which meets the above requirements. The particle identification in the *DIRC* is based on the Čerenkov radiation produced by charged particles crossing a material with a speed higher than light speed in that material. The angular opening of the Čerenkov radiation cone depends on the particle speed:

$$\cos\theta_c = \frac{1}{n\beta}$$

where θ_c is the Čerenkov cone opening angle, n is the refractive index of the material and β is the particle velocity over c. The principle of the detection is based on the fact that the magnitudes of angles are maintained upon reflection from a flat surface.

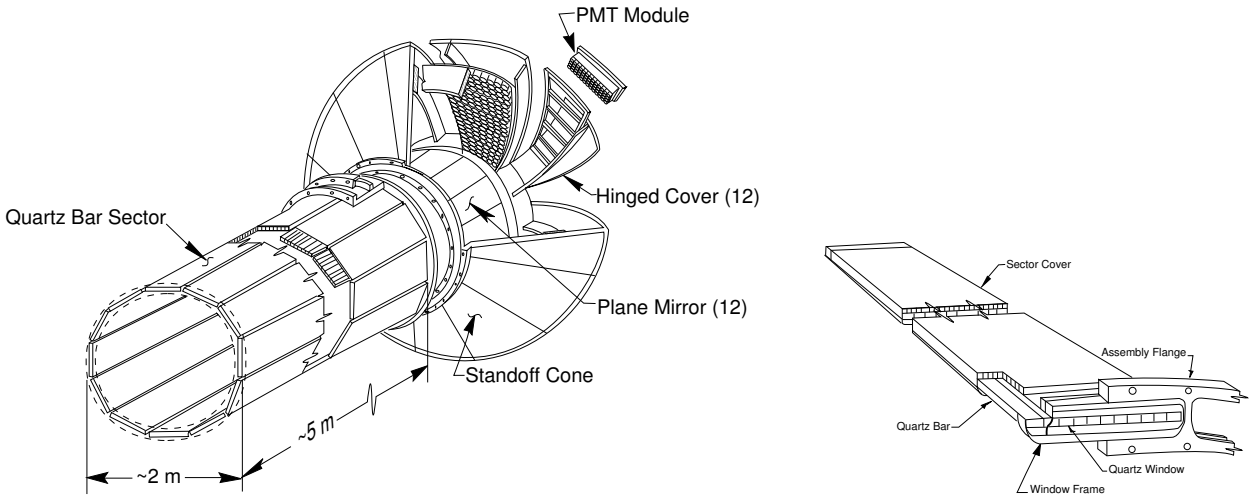

Figure 2.10: Mechanical elements of the *DIRC* and schematic view of bars assembled into a mechanical and optical sector.

Since particles are produced mainly forward in the detector because of the boost, the *DIRC* photon detector is placed at the backward end: the principal components of the *DIRC* are shown in Fig. 2.10. The *DIRC* is placed in the barrel region and consists of 144 long, straight bars arranged in a 12-sided polygonal barrel. The bars are $1.7\,cm$-thick, $3.5\,cm$-wide and $4.90\,m$-long: they are placed into 12 hermetically sealed containers, called *bar boxes*, made of very thin aluminum-hexcel

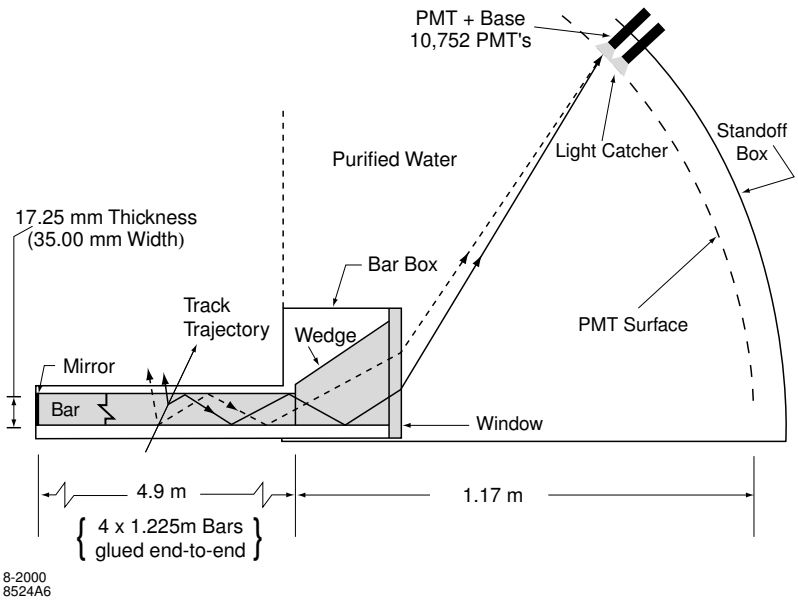

Figure 2.11: Schematics of the DIRC fused silica radiator bar and imaging region. Not shown is a 6 mrad angle on the bottom surface of the wedge.

panels. Within a single bar box, 12 bars are optically isolated by a $\sim 150\,\mu m$ air gap enforced by custom shims made from aluminum foil.

The radiator material used for the bars is synthetic fused silica: the bars serve both as radiators and as light pipes for the portion of the light trapped in the radiator by total internal reflection. Synthetic silica has been chosen because of its resistance to ionizing radiation, its long attenuation length, its large index of refraction, its low chromatic dispersion within its wavelength acceptance.

The Čerenkov radiation is produced within these bars and is brought, through successive total internal reflections, in the backward direction outside the tracking and magnetic volumes: only the backward end of the bars is instrumented. A mirror placed at the other end on each bar reflects forward-going photons to the instrumented end. The Čerenkov angle at which a photon was produced is preserved in the propagation, modulo some discrete ambiguities (the forward-backward ambiguity can be resolved by the photon arrival-time measurement, for example). The *DIRC* efficiency grows together with the particle incidence angle because more light is produced and a larger fraction of this light is totally reflected. To maximize the total reflection, the material must have a refractive index (fused silica index is $n = 1.473$) higher than the surrounding environment (the

DIRC is surrounded by air with index $n = 1.0002$).

Once photons arrive at the instrumented end, most of them emerge into a water-filled expansion region (see Fig. 2.11), called the ***Standoff Box***: the purified water, whose refractive index matches reasonably well that of the bars ($n_{H_2O} = 1.346$), is used to minimize the total internal reflection at the bar-water interface.

The standoff box is made of stainless steel and consists of a cone, cylinder and 12 sectors of PMTs: it contains about 6000 liters of purify water. Each of the 12 PMTs sectors contains 896 PMTs in a close-packed array inside the water volume: the PMTs are linear focused $2.9\,cm$ diameter photo-multiplier tubes, lying on an approximately toroidal surface.

The *DIRC* occupies only $8\,cm$ of radial space, which allows for a relatively large radius for the drift chamber while keeping the volume of the CsI Calorimeter reasonably low: it corresponds to about $17\%\ X_0$ at normal incidence. The angular coverage is the 94% of the ϕ azimuthal angle and the 83% of $\cos\theta_{CM}$.

Čerenkov photons are detected in the visible and near-UV range by the PMT array. A small piece of fused silica with a trapezoidal profile glued at the back end of each bar allows for significant reduction in the area requiring instrumentation because it folds one half of the image onto the other half. The PMTs are operated directly in water and are equipped with light concentrators: the photo-multiplier tubes are about $1.2\,m$ away from the end of the bars. This distance from the bar end to the PMTs, together with the size of the bars and PMTs, gives a geometric contribution to the single photon Čerenkov angle resolution of about 7 mrad. This is a bit larger than the resolution contribution from Čerenkov light production (mostly a 5.4 mrad chromatic term) and transmission dispersions. The overall single photon resolution expected is about 9 mrad.

The image from the Čerenkov photons on the sensitive part of the detector is a cone cross-section whose opening angle is the Čerenkov angle modulo the refraction effects on the fused silica-water surface. In the most general case, the image consists of two cone cross-sections out of phase one from the other by a value related to an angle which is twice the particle incidence angle. In order to associate the photon signals with a track traversing a bar, the vector pointing from the center of the bar end to the center of each PMT is taken as a measure of the photon propagation angles α_x, α_y and α_z. Since the track position and angles are known from the tracking system, the three α angles can be used to determine the two Čerenkov angles θ_C and ϕ_C. In addition, the arrival time

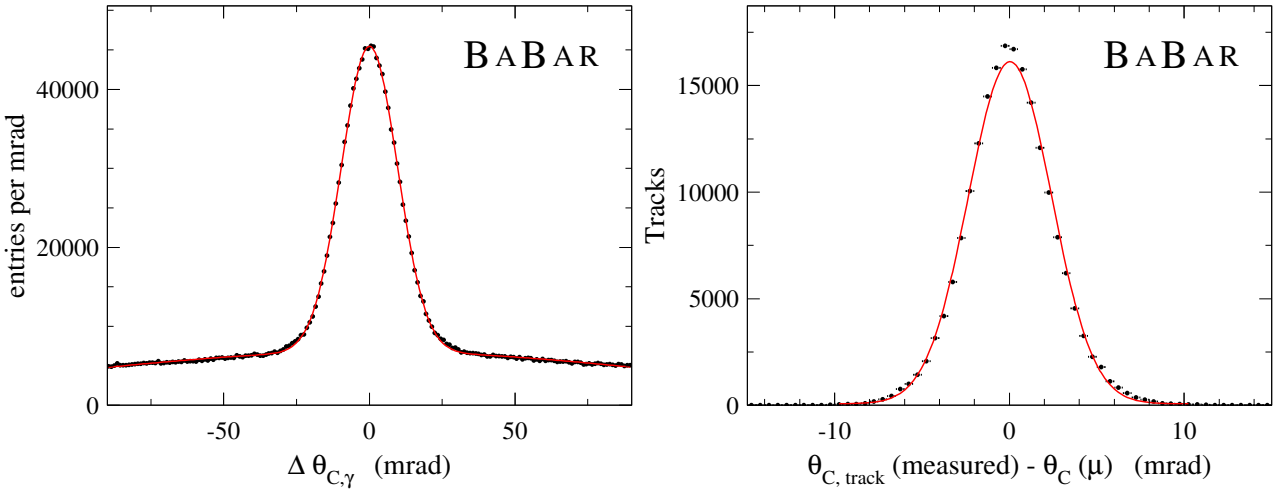

Figure 2.12: From di-muon data events, left plot: single photon Čerenkov angle resolution. The distribution is fitted with a double-Gaussian and the width of the narrow Gaussian is 9.6 mrad. Right plot: reconstructed Čerenkov angle for single muons. The difference between the measured and expected Čerenkov angle is plotted and the curve represents a Gaussian distribution fit to the data with a width of 2.4 mrad.

of the signal provides an independent measurement of the propagation of the photon and can be related to the propagation angles α. This over-constraint on the angles and the signal timing are useful in dealing with ambiguities in the signal association and high background rates.

The expected number of photo-electrons (N_{pe}) is ~ 28 for a $\beta = 1$ particle entering normal to the surface at the center of a bar and increases by over a factor of of two in the forward and backward directions.

The time distribution of real Čerenkov photons from a single event is of the order of $50\,ns$ wide and during normal data taking they are accompanied by hundreds of random photons in a flat background distribution within the trigger acceptance window. The Čerenkov angle has to be determined in an ambiguity that can be up to 16-fold: the goal of the reconstruction program is to associate the correct track with the candidate PMT signal with the requirement that the transit time of the photon from its creation in the bar to its detection at the PMT be consistent with the measurement error of about $1.5\,ns$.

An unbinned maximum likelihood formalism is used to take into account all information provided by the $DIRC$: the reconstruction routine provides a likelihood value for each of the five stable particle types (e, μ, π, K and p) if the track passes through the active volume of the $DIRC$. These likelihood probabilities are calculated in an iterative process by maximizing the likelihood value for the entire event while testing different hypotheses for each track. If enough photons are found, a fit of θ_C and the number of observed signal and background photons are calculated.

In the absence of correlated systematic errors, the resolution ($\sigma_{C,\text{track}}$) on the track Čerenkov angle should scale as

$$\sigma_{C,\text{track}} = \frac{\sigma_{C,\gamma}}{\sqrt{N_{pe}}}$$

where $\sigma_{C,\gamma}$ is the single photon angle resolution. This angular resolution (obtained from di-muon events) can be estimated to be about 10.2 mrad, in good agreement with the expected value (see left plot in fig. 2.12). The measured time resolution is $1.7\,ns$ close to the intrinsic $1.5\,ns$ time spread of the PMTs. In di-muon event data, the number of photo-electrons varies between 20 for small polar angles at the center of the barrel and 65 at large polar angles: this is variation is well reproduced by MonteCarlo and can be understood by the fact that the number of Čerenkov photons varies with the path length of the track in the radiator (smaller path length at perpendicular incidence at the center of the barrel). Also the fraction of photons trapped by total internal reflection rises with larger values of $|\cos(\theta_{\text{track}})|$: this increase in the number of photons for forward going tracks corresponds also to an increase in momentum of the tracks and thus an improvement of the $DIRC$ performance.

The width of the track Čerenkov angle resolution for di-muon events is 2.4 mrad compared to the design goal of 2.2 mrad (see right plot in Fig. 2.12). From the measured single track resolution versus momentum in d-muon events and from the difference between the expected Čerenkov angles of charged pions and kaons, the pion-kaon separation power of the $DIRC$ can be evaluated: the expected separation between pions and kaons at 3 GeV/c is about 4.2σ, within 15% of the design goal.

The charged kaon efficiency is compared to the charged pion misidentification in Fig. 2.13. In the reconstruction of the invariant mass of the hadronic system, given the difference in the kaon momentum spectrum, Fig. 2.13, a ch arged track is identified as kaon if $p_K > 300\,\text{MeV}$.

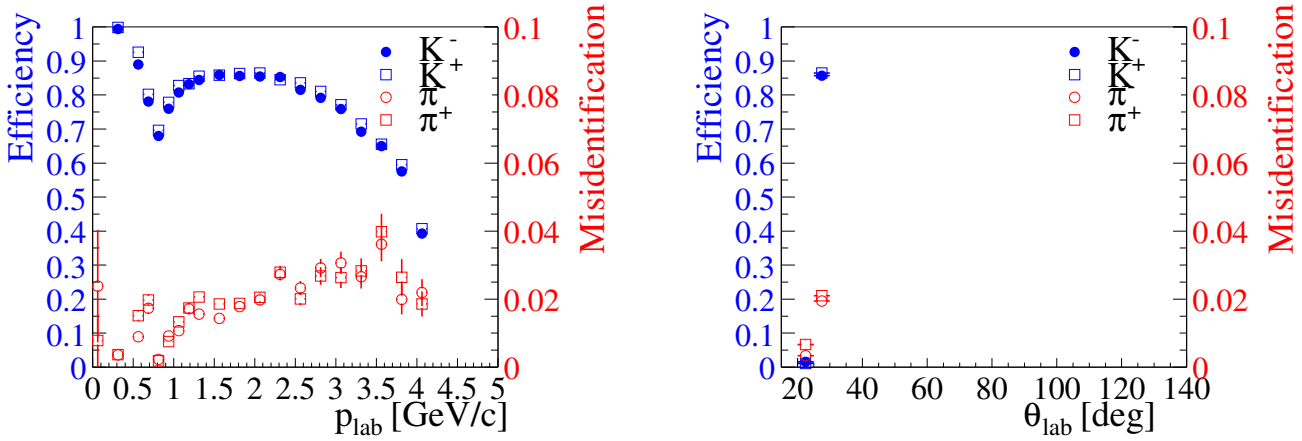

Figure 2.13: Charged kaon identification and pion misidentification probabilit y for the tight kaon micro selector as a function of momentum (left) and polar angle (right). The solid markers indicate the efficiency for positive particles, the empty markers the efficiency for negative particles. Note the different scales for identification and misidentification on the left and right ordinates, respectively.

2.5 Electromagnetic calorimeter: *EMC*

The understanding of CP violation in the B meson system requires the reconstruction of final state containing a direct π^0 or that can be reconstructed through a decay chain containing one or more daughter $\pi^0 s$. The electromagnetic calorimeter is designed to measure electromagnetic showers with excellent efficiency and energy and angular resolution over the energy range from 20 MeV to 9 GeV. This capability should allow the detection of photons from π^0 and η decays as well as from electromagnetic and radiative processes. By identifying electrons, the *EMC* contributes to the flavour tagging of neutral B mesons via semi-leptonic decays. The upper bound of the energy range is given by the need to measure QED processes like $e^+e^- \rightarrow e^+e^-(\gamma)$ and $e^+e^- \rightarrow \gamma\gamma$ for calibration and luminosity determination. The lower bound is set by the need for highly efficient reconstruction of B-meson decays containing multiple π^0s and η^0s. The measurement of very rare decays containing π^0s in the final state (for example, $B^0 \rightarrow \pi^0\pi^0$) puts the most stringent requirements on energy resolution, expected to be of the order of $1-2\%$. Below 2 GeV energy, the π^0 mass resolution is dominated by the energy resolution, while at higher energies, the angular resolution becomes dominant and it is required to be of the order of few mrad. The *EMC* is also used for electron identification and for completing the *IFR* output on μ and K^0_L identification. It

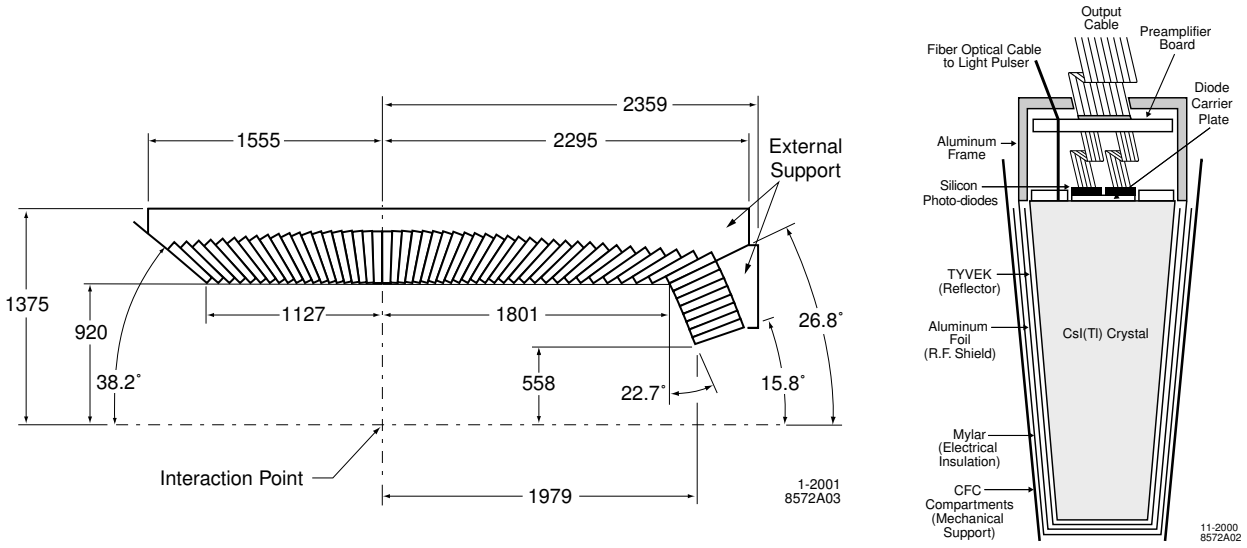

Figure 2.14: The electromagnetic calorimeter layout in a longitudinal cross section and a schematic view of the wrapped CsI(Tl) crystal with the front-end readout package mounted on the rear face (not to scale).

also has to operate in a $1.5\,T$ magnetic field.

The EMC has been chosen to be composed of a finely segmented array of thallium-doped cesium iodide (CsI(Tl)) crystals. The crystals are read out with silicon photo-diodes that are matched to the spectrum of scintillation light. The energy resolution of a homogeneous crystal calorimeter can be described empirically in terms of a sum of two terms added in quadrature:

$$\frac{\sigma_E}{E} = \frac{a}{\sqrt[4]{E(\,\mathrm{GeV})}} \oplus b$$

where E and σ_E refer to the energy of a photon and its rms error, measured in GeV. The energy dependent term $a(\sim 2\%)$ arises basically from the fluctuations in photon statistics, but also from the electronic noise of the photon detector and electronics and from the beam-generated background that leads to large numbers of additional photons. This first term dominates at low energy, while the constant term $b(\sim 1.8\%)$ is dominant at higher energies (> 1 GeV). It derives from non-uniformity in light collection, leakage or absorption in the material in front of the crystals and uncertainties in the calibration.

The angular resolution is determined by the transverse crystal size and the distance from the interaction point: it can be empirically parameterized as a sum of an energy dependent and a constant

term

$$\sigma_\theta = \sigma_\phi = \frac{c}{\sqrt{E(\,\mathrm{GeV})}} + d$$

where E is measured in GeV and with $c \sim 4\,\mathrm{mrad}$ and $d \sim 0\,\mathrm{mrad}$.

In CsI(Tl), the intrinsic efficiency for the detection of photons is close to 100% down to a few MeV, but the minimum measurable energy in colliding beam data is about $20\ \mathrm{MeV}$ for the EMC: this limit is determined by beam and event-related background and the amount of material in front of the calorimeter. Because of the sensitivity of the π^0 efficiency to the minimum detectable photon energy, it is extremely important to keep the amount of material in front of the EMC to the lowest possible level.

Thallium-doped CsI has high light yield and small Molière radius in order to allow for excellent energy and angular resolution. It is also characterized by a short radiation length for shower containment at *BABAR* energies. The transverse size of the crystals is chosen to be comparable to the Molière radius achieving the required angular resolution at low energies while limiting the total number of crystals and readout channels.

The *BABAR* EMC (left plot in Fig. 2.14) consists of a cylindrical barrel and a conical forward end-cap: it has a full angle coverage in azimuth while in polar angle it extends from 15.8° to 141.8° corresponding to a solid angle coverage of 90% in the CM frame. Radially the barrel is located outside the particle ID system and within the magnet cryostat: the barrel has an inner radius of $92\,cm$ and an outer radius of $137.5\,cm$ and it's located asymmetrically about the interaction point, extending $112.7\,cm$ in the backward direction and $180.1\,cm$ in the forward direction. The barrel contains 5760 crystals arranged in 48 rings with 120 identical crystals each: the end-cap holds 820 crystals arranged in eight rings, adding up to a total of 6580 crystals. They are truncated-pyramid CsI(Tl) crystals (right plot in Fig. 2.14): they are tapered along their length with trapezoidal cross-sections with typical transverse dimensions of $4.7 \times 4.7\,cm^2$ at the front face, flaring out toward the back to about $6.1.0\,cm^2$. All crystals in the backward half of the barrel have a length of $29.6\,cm$: toward the forward end of the barrel, crystal lengths increase up to $32.4\,cm$ in order to limit the effects of shower leakage from increasingly higher energy particles. All end-cap crystals are of $32.4\,cm$ length. The barrel and end-cap have total crystal volumes of $5.2\,m^3$ and $0.7\,m^3$, respectively. The CsI(Tl) scintillation light spectrum has a peak emission at $560\,nm$: two indepen-

dent photodiodes collect this scintillation light from each crystal. The readout package consists of two silicon PIN diodes, closely coupled to the crystal and to two low-noise, charge-sensitive preamplifiers, all enclosed in a metallic housing.

A typical electromagnetic shower spreads over many adjacent crystals, forming a *cluster* of energy deposit: pattern recognition algorithms have been developed to identify these clusters and to discriminate single clusters with one energy maximum from merged clusters with more than one local energy maximum, referred to as *bumps*. The algorithms also determine whether a bump is generated by a charged or a neutral particle. Clusters are required to contain at least one seed crystal with an energy above $10\ \mathrm{MeV}$: surrounding crystals are considered as part of the cluster if their energy exceeds a threshold of $1\ \mathrm{MeV}$ or if they are contiguous neighbors of a crystal with at least $3\ \mathrm{MeV}$ signal. The level of these thresholds depends on the current level of electronic noise and beam-generated background.

A bump is associated with a charged particle by projecting a track to the inner face of the calorimeter: the distance between the track impact point and the bump centroid is calculated and if it is consistent with the angle and momentum of the track, the bump is associated with this charged particle. Otherwise it is assumed to originate from a neutral particle.

On average, 15.8 clusters are detected per hadronic event: 10.2 are not associated to any charged particle. Currently, the beam-induced background contributes on average with 1.4 neutral clusters with energy above $20\ \mathrm{MeV}$.

At low energy, the energy resolution of the *EMC* is measured directly with a $6.13\ \mathrm{MeV}$ radioactive photon source (a neutron-activated fluorocarbon fluid) yielding $\sigma_E/E = 5.0 \pm 0.8\%$. At high energy, the resolution is derived from Bhabha scattering where the energy of the detected shower can be predicted from the polar angle of the electrons and positrons. The measured resolution is $\sigma_E/E = 1.9 \pm 0.1\%$ at $7.5\ \mathrm{GeV}$. Fig. 2.15 shows the energy resolution on data compared with expectations from MonteCarlo. From a fit to the experimental results to eq.2.5, $a = 2.32 \pm 0.30\%$ and $b = 1.85 \pm 0.12\%$ are obtained. The constant term comes out to be greater than expected: this is mainly caused by a cross talk effect, still not corrected, in the front-end electronics.

The measurement of the angular resolution is based on Bhabha events and ranges between 12 mrad and 3 mrad going from low to high energies. A fit to eq. 2.5 results in $c = (3.87 \pm 0.07)\ mrad$ and $d = (0.00 \pm 0.04)\ mrad$.

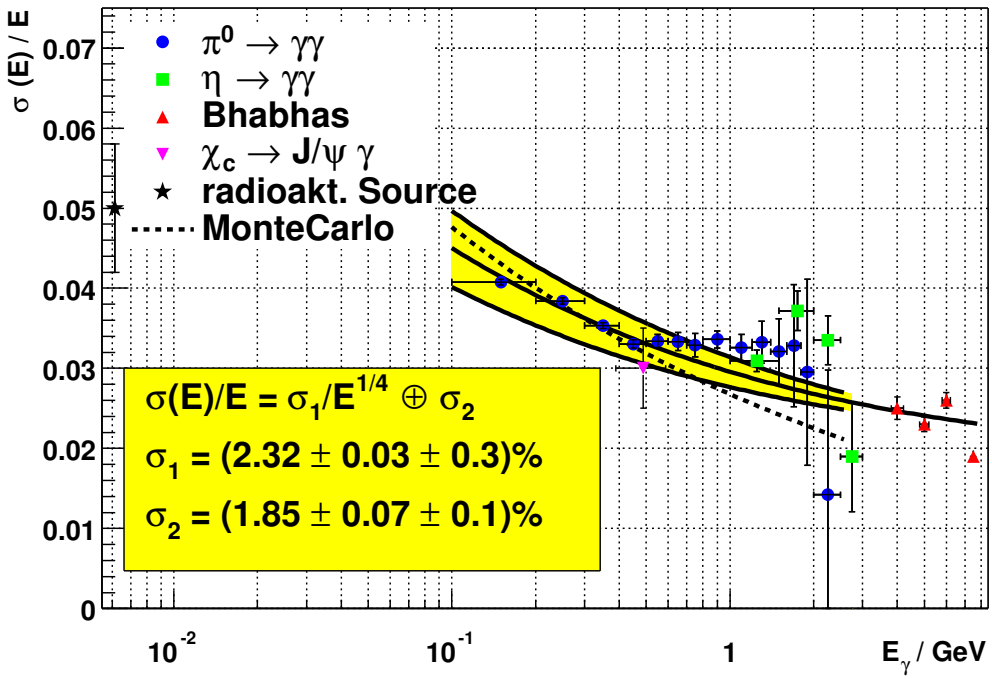

Figure 2.15: EMC *resolution as a function of the energy.*

Different criteria are established to select electrons with different level of purity. Electrons are primarily separated from charged hadrons on the basis of the ratio of the energy E deposited in the EMC to the track momentum p ($\frac{E}{p}$). This quantity should be compatible with the unity for electrons since they deposit all the energy in the calorimeter. The other charged tracks should appear as MIP (minimal ionizing particles) unless they have hadronic interactions in the calorimer crystals. To further separate hadrons a variable describing the shape of the energy deposition in the EMC (LAT) is used. In addition, the $\mathrm{d}E/\mathrm{d}x$ energy loss in the DCH and the DIRC Čerenkov angle are required to be consistent with an electron and it offers a good separation in a wide range.

The track selection criteria are tightened for electrons selection to suppress background and to ensure a reliable momentum measurement and identification efficiency: there are requirements in addition for the transverse momentum $p_\perp > 0.1\,\mathrm{GeV}/c$, and $N_{Dch} \geq 12$ for the number of associated drift chamber hits. Furthermore, only tracks with a polar angle in the range $0.360 < \theta_{lab} < 2.37$ and electron candidates with a laboratory momentum $p_{lab} > 0.5\,\mathrm{GeV}/c$ are considered.

Electrons are identified using the a likelihood-based selector [30], which uses a number of discriminating variables:

- E_{cal}/p_{lab}, the ratio of E_{cal}, the energy deposited in the EMC, and p_{lab} the momentum in the laboratory rest frame measured using the tracking system; LAT, the lateral shape of the calorimeter deposit; $\Delta\Phi$, the azimuthal distance between the centroid of the EMC cluster and the impact point of the track on the EMC; and N_{cry}, the number of crystals in the EMC cluster;
- dE/dx, the specific energy loss in the DCH;
- the Čerenkov angle θ_C and N_C, the number of photons measured in the DIRC.

First, muons are eliminated based on dE/dx and the shower energy relative to the momentum. For the remaining tracks, likelihood functions are computed assuming the particle is an electron, pion, kaon, or proton. These likelihood functions are based on probability density functions that are derived from pure particle data control samples for each of the discriminating variables. For hadrons, we take into account the correlations between energy and shower-shapes. Using combined likelihood functions

$$\begin{aligned} L(\xi) &= P(E/p, LAT, \Delta\Phi, dE/dx, \theta_C|\xi) \\ &= P_{Emc}(E/p, LAT, \Delta\Phi|\xi)\ \ P_{Dch}(dE/dx|\xi)\ \ P_{DRC}(\theta_C|\xi) \end{aligned}$$

for the hypotheses $\xi \in \{e, \pi, K, p\}$, the fraction

$$F_{\rm e} = \frac{f_{\rm e} L({\rm e})}{\sum_\xi f_\xi L(\xi)}\ , \tag{2.1}$$

is defined, where, for the relative particle fractions, $f_{\rm e} : f_\pi : f_{\rm K} : f_{\rm p} = 1 : 5 : 1 : 0.1$ is assumed. A track is identified as an electron if $F_{\rm e} > 0.95$.

The electron identification efficiency has been measured using radiative Bhabha events, as function of laboratory momentum p_{lab} and polar angle θ_{lab}. The misidentification rates for pions, kaons, and protons are extracted from selected data samples. Pure pions are obtained from kinematically selected $K^0_S \to \pi^+\pi^-$ decays and three prong $\tau^\pm$ decays. Two-body Λ and D^0 decays provide pure samples of protons and charged kaons.

The performance of the likelihood-based electron identification algorithm is summarized in Figure 2.16, in terms of the electron identification efficiency and the per track probability that a hadron is misidentified as an electron.

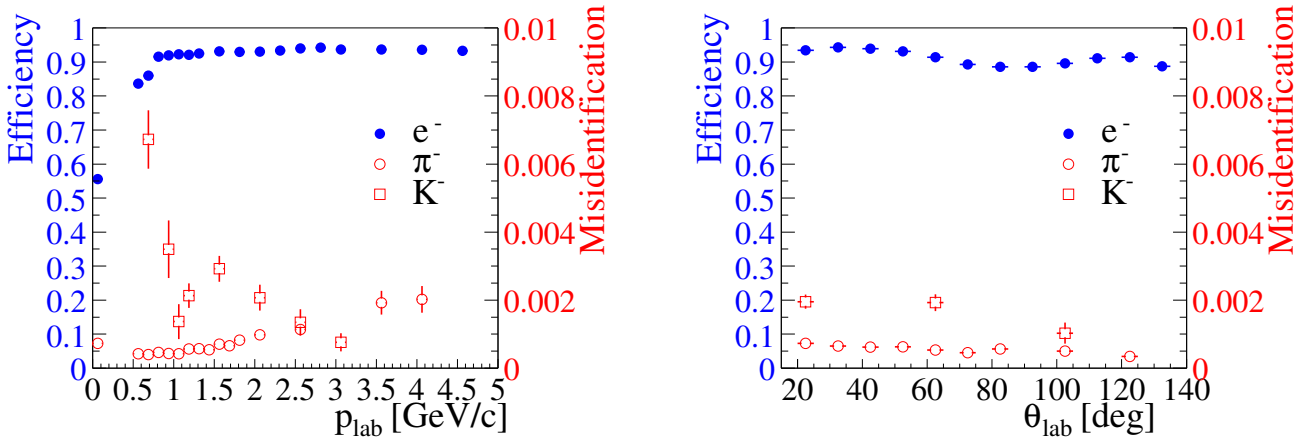

Figure 2.16: Electron identification and hadron misidentification probability for the likelihood-based electron selector as a function of momentum (left) and polar angle (right). Note the different scales for identification and misidentification on the left and right ordinates, respectively. The measurements are for luminosity-averaged rates for Run-1 and Run-2.

The average hadron fake rates per track are determined separately for positive and negative particles, taking into account the relative abundance from Monte Carlo simulation of $B\overline{B}$ events, with relative systematic uncertainties of 3.5%, 15% and 20% for pions, kaons, and protons, respectively. The resulting average fake rate per hadron track of $p_{lab} > 1.0\,\mathrm{GeV}/c$, is of the order of 0.05% for pions and 0.2% for kaons.

2.6 Instrumented Flux Return: *IFR*

IFR (*Instrumented Flux Return*) detector is dedicated to muon identification and neutral hadrons detection (mainly K_L^0) in a wide range of momentum and angles.

The IFR, as all the other *BABAR* subsystems, has an asymmetric structure with a polar angle coverage that is $17^\circ \leq \theta_{lab} \leq 150^\circ$. The IFR (Fig. 2.17) is made of 19 layers of Resistive Plate Chambers (RPC) in the barrel region and 18 layers in forward and backward regions, that are placed inside the iron layers used for the solenoidal magnetic field return joke. The iron structure is subdivided in three main parts: the barrel one surrounding the solenoid, made of 6 sextants covering the radial distance between $1.820\ m$ and $3.045\ m$ with a length of $3.750\ m$ (along the z axis);

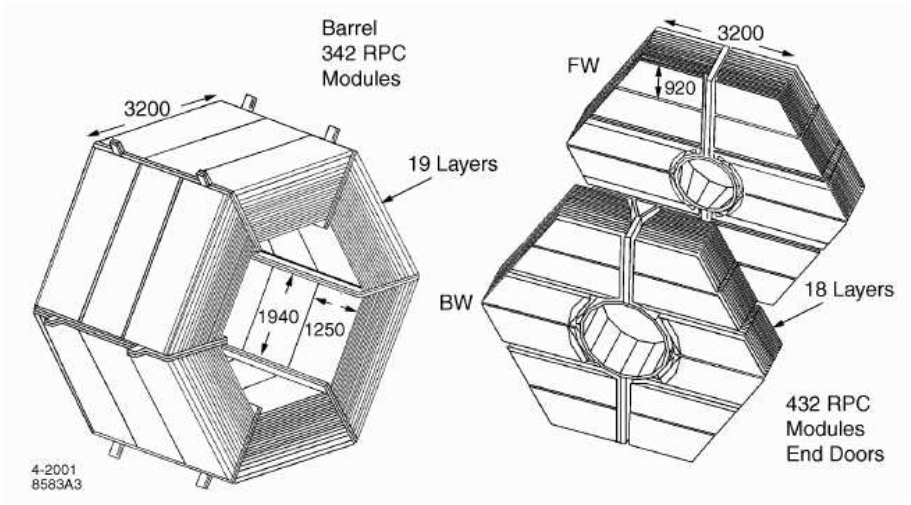

Figure 2.17: IFR *view*

the forward end-cap and backward end-cap covering the forward (positive z axis) and backward regions. Moreover, two cylindrical RPC layers have been installed between the calorimeter and the magnet cryostat in order to reveal particles exiting from the EMC. Those layers should cover the ϕ regions not covered by the barrel. Cylindrical layers are subdivided in four sections, each of them covering one fourth of the circumference: each of them has four RPC groups with orthogonal readout strips. $u - v$ helicoidal strips are placed inside along module's diagonals while ϕ and z parallel strips are placed outside. The summary of IFR readout segmentation is given in Tab. 2.4.

Each end-cap has an hexagonal shape and is vertically subdivided in two halves in order to allow internal subsystems access, if necessary: vacuum tube and PEP-II focusing elements are placed in the middle. Iron plates have a thickness ranging from 2 cm, for the inner ones placed nearest to the interaction region, to 10 cm for the outer ones; this means a total thickness of steel at normal incidence of ~ 65 cm (nearly corresponding to ~ 4 interaction lengths) in the barrel and ~ 60 cm in the end-caps. Nominal distance between iron layers in the inner barrel region is 3.5 cm while is 3.2 cm everywhere else. The increased granularity of inner layers with respect to the outer ones is due to the fact that the largest part of particles detected inside the IFR are interacting in the very first material layers. Chosen segmentation is also the result of a compromise between the subsystem cost (proportional to the volume) and the need of a good efficiency for low momentum ($> 700\,\mathrm{MeV}$) muon detection, minimizing, at the same time, fraction of K_L^0's that are

section	# di sectors	coor.	readout # layer	# strip layer/sector	strip len. (cm)	strip larg. (mm)	total # channel
barrel	6	ϕ	19	96	350	19.7-32.8	$\approx$ 11k
		z	19	96	190-318	38.5	$\approx$ 11k
end-cap	4	y	18	6x32	124-262	28.3	13,824
		x	18	3x64	10-180	38.0	$\approx$ 15k
cyl.	4	ϕ	1	128	370	16.0	512
		z	1	128	211	29.0	512
		u	1	128	10-422	29.0	512
		v	1	128	10-423	29.0	512

Table 2.4: IFR *readout segmentation. Total number of channels is* $\sim$ 53*k.*

not interacting inside the IFR. Result of this optimization is a not uniform segmentation with iron plates that have thickness increasing with distance from beam line. RPC section is shown in Fig. 2.18.

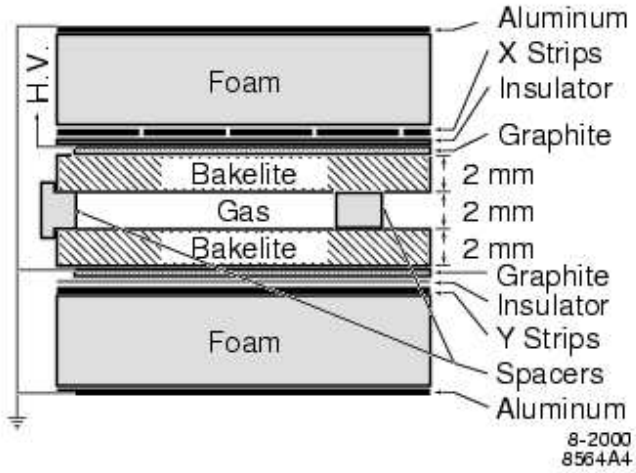

Figure 2.18: *Planar* RPC *section with HV connection scheme.*

In each barrel sextant layers are kept together by a structure that reduces the coverage of solid angle with active detectors of $\sim 7\%$. Active coverage of IFR detector is $\approx 2000\ m^2$, for a total RPC modules number that is ~ 900. Signals produced by particles crossing the gas gap inside the RPCs

are collected on both sides of the chamber by using thin strips (thickness $\sim 40\ \mu m$) with width of the order of a centimeter. Strips are applied in two orthogonal directions on insulating planes $200\ \mu m$ thick, in order to have a bi-dimensional view. In each barrel sextant each gap is hosting a chamber. This consist of a set of 3 RPC modules of rectangular shape. Each module is ~ 125 cm long along beams direction with variable width in order to completely fill the gap. Each chamber is equipped with 96 $\phi - strip$ placed along z axis that are measuring the ϕ angle inside the barrel and 96 $z - strip$ orthogonal to beams direction that are measuring z coordinate. $z - strips$ are subdivided into 3 panels of 32 strips with largeness, function of chamber radial position, ranging between 1.78 and 3.37 cm. This projective geometry allows a constant number of strips for all the various layers without decreasing detector resolution (each strip covers the same azimuthal angle). The used gas mixture is made of 56.7% Argon, 38.8% Freon-134a and 4.5% Isobutane. Working voltage for RPCs is $\sim 7.5\ kV$. Iron layers keeping apart RPC planes are chilled by a water system that keeps the temperature $\sim 20^oC$. RPC efficiencies have been measured by using cosmics taken on a weekly base.

Mean efficiency during 2000 run has been $\sim 78\%$ for the barrel and $\sim 87\%$ for the forward end-cap, less than that one measured in June 1999 ($\sim 92\%$). During the Summer 1999 the ambient temperature increased very much reaching about 32° to 38° inside the iron. During such period the IFR had problems to run the full detector because the dark current drawn by the chambers exceeded the total current limit provided by the power supply. All the chambers drawing more than $200\ \mu$A were disconnected. In October the chambers were re-connected but they didn't recover the full efficiency. The forward end-cap has been completely reconstructed and installed in the Summer 2002: 5 intermediate RPC layers were replaced by 2.54 cm of brass, 10 cm of steel were added after the last RPC layer, an RPC(layer 19) was added in front of the forward end-cap, an RPC belt was added in the barrel–end-cap overlap region. Barrel efficiencies are still decreasing and are at $\sim 40\%$ level while in the new forward end-cap, they are greater than 90%.

Muons are identified by measuring the number of traversed interaction lengths in the entire detector and comparing it with the number of expected interaction lengths for a muon of a given momentum. Moreover, the projected intersections of a track with the RPC planes are computed and, for each readout plane, all strips clusters detected within a predefined distance from the predicted intersection are associated with the track: the average number and the r.m.s. of the distribution of RPC strips per layer gives additional μ/π discriminating power. We expect in fact the average number of strips per layer to be larger for pions producing an hadronic interaction than for muons.

Other variables exploiting clusters distribution shapes are constructed. Selection criteria based on all these variables are applied to select muons. The performance of the muon selection has been tested on samples of kinematically identified muons from $\mu\mu ee$ and $\mu\mu\gamma$ final states and pions from three-prong τ decays and $K_S \to \pi^+\pi^-$ decays.

The muon selection procedure is as follows:

- tight criteria on tracking: $p_\perp > 0.1\,\mathrm{GeV}/c$, $N_{DCH} \geq 12$, $0.360 < \theta_{lab} < 2.37$ and $p_{lab} > 1.0\,\mathrm{GeV}/c$
- the energy deposited in the EMC is required to be consistent with the minimum ionizing particle:

  $50\,\mathrm{MeV} < E_{cal} < 400\,\mathrm{MeV}$;
- the number of IFR layers associated with the track has to be $N_L \geq 2$.
- the interaction lengths of material traversed by the track has to be $\lambda_{meas} > 2.2$.
- The number of interaction lengths expected for a muon of the measured momentum and angle to traverse is estimated by extrapolating the track up to the last *active* layer of the IFR. This estimate takes into account the RPC efficiencies which are routinely measured and stored. We require the difference $\Delta\lambda = \lambda_{exp} - \lambda_{meas}$ to be < 1.0, for tracks with momentum greater than 1.2 GeV/c. For track momenta between 0.5 GeV/c and 1.2 GeV/c, a variable limit is placed: $\Delta\lambda < [(p_{lab} - 0.5)/0.7]$.
- The *continuity* of the IFR cluster is defined as $T_c = \frac{N_L}{L-F+1}$, where L and F are the last and first layers with hit. T_c is expected to be 1.0 for muons penetrating an ideal detector whereas is expected smaller for hadrons. We require $T_c > 0.3$ for tracks with $0.3 < \theta_{lab} < 1.0$ (i.e. in the Forward End Cap to remove beam background).
- The observed number of hit strips in each RPC layer is used to impose the conditions on the average number of hits, $\bar{m} < 8$, and the standard deviation, $\sigma_m < 4$.
- The strip clusters in the IFR layers are combined to form a track and fit to a third degree polynomial, with the quality of the fit selected by the condition $\chi^2_{fit}/DOF < 3$. In addition, the cluster centroids are compared to the extrapolated charged track, with the requirement $\chi^2_{trk}/DOF < 5$.

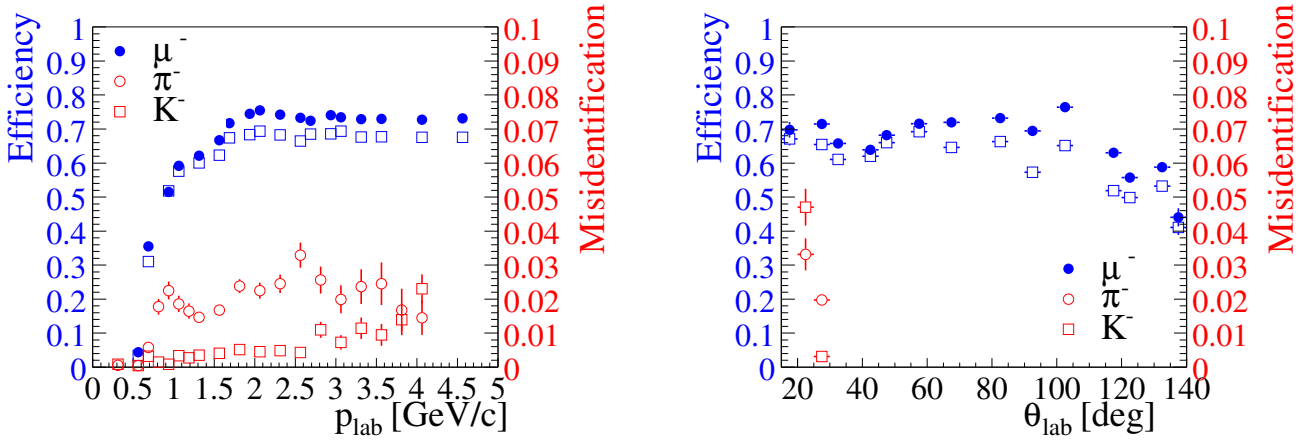

Figure 2.19: Muon identification and hadron misidentification probability for the tight muon selector as a function of momentum (left) and polar angle (right). The solid markers indicate the efficiency in 2000, the empty markers the efficiency in 2001. Note the different scales for identification and misidentification on the left and right ordinates, respectively.

The muon identification efficiency has been measured using $\mu^+\mu^-(\gamma)$ events and two-photon production of $\mu^+\mu^-$ pairs. The misidentification rates for pions, kaons, and protons are extracted from selected data samples. The performance of the muon identification algorithm is summarized in Fig. 2.19, in terms of the muon identification efficiency and the per track probability that a hadron is misidentified as a muon. Only tracks in the fiducial volume, i.e. with a polar angle in the range $20.6 < \theta_{lab} < 135.9°$, are considered. The errors shown are statistical only, the systematic error is dominated by variations in the performance of the IFR as a function of position and time.

At the end of the summer 2004 RPC from Top and Bottom Barrel sextant has been substituted with limited streamer tube (LST). Data recording **Run-5** has been started only in the second half of April 2005 so there aren't still enough data to evaluate LST efficiency and performances.

Chapter 3

Introduction to the study of the $B \to D^{*-} a_1^+$ decay

3.1 Introduction

This chapter represents a brief introduction to the study of the non-leptonic $B \to D^{*-} a_1^+$ decay channel.

As recently suggested in [27], measuring the polarization amplitudes in the $B \to D^{*-} a_1^+$ decay, which represents the main contribution to $B \to D^{*-} \pi^+ \, \pi^+ \, \pi^-$, provides a test of the factorization assumption. As we'll see in the next, the factorization represents one of the mostly used tool to evaluate the hadronic matrix elements describing the QCD non-perturbative effects in the B decays amplitudes. Despite this approach, and its extensions, was found to predict with good accuracy several processes, there are cases where it fails and it is important to test it in depth in order to verify its limits and improve our knowledge on the strong interactions effects in exclusive weak decays of hadrons containing a b-quark.

In section 1.5, we have seen how the study of time dependent CP asymmetries in $B \to D^{(*)} h$ decays can be used to extract the weak phase $(2\beta + \gamma)$. When the two meson in the final state have both spin equal to one, as in $B \to D^{*-} a_1^+$, it is possible to improve the method by performing a time dependent angular analysis that allows a determination of $(2\beta + \gamma)$ without using the information on the (hard to measure) doubly Cabibbo suppressed amplitude and resolving the discrete ambiguities discussed in 1.5.

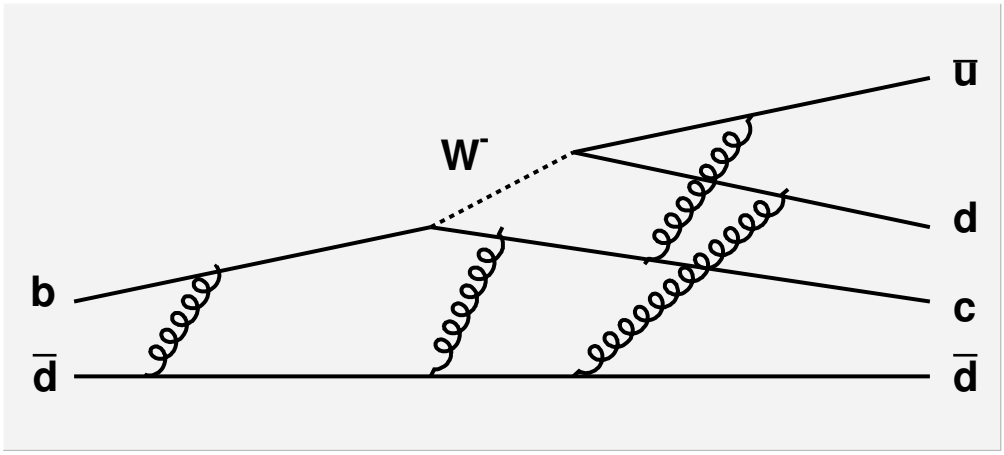

Figure 3.1: Tree diagram $b \to c\bar{u}d$, with a spectator quark $\bar{d}$, affected by gluon exchange.

As a necessary preliminary step, it is important to correctly identify the $a_1^+ \to \pi^+ \pi^+ \pi^-$ contribution to the 3 pions in $B \to D^{*-}\pi^+ \pi^+ \pi^-$ and disentangle it from other possible resonant structures. This is a challenging issue since the $a_1(1260)$ meson mass and width are poorly known [13]. The currently available measurements on the a_1 parameters give, in fact, inconsistent results. The a_1 parameters can be studied through the $B \to D^{*-} a_1^+$ decay which represents a quite clean environment to measure them.
The work presented in this thesis focus on the study of the $a_1(1260)$ meson properties.
In order to separate the a_1 from other possible contributions to the 3 pion system in $B \to D^{*-}\pi^+ \pi^+ \pi^-$ and to study the $a_1^+ \to \pi^+ \pi^+ \pi^-$ decay, a partial wave analysis is performed. The 3 pions mass spectrum is divided in several intervals and, in each interval, the Dalitz plot of the 3 body decay is analyzed.

Section 3.2 contains a brief introduction on the non-leptonic B decays. The effective Hamiltonian, obtained within the Operator Product Expansion, is shown and principles and limits of the factorization approach are discussed. In section 3.3 the current experimental measurements of the $a_1(1260)$ properties are summarized, and the advantages to study it through the $B \to D^{*-} a_1^+$ decay are illustrated. Sections 3.4 and 3.5 discuss the proposed factorization test and $\sin(2\beta + \gamma)$ measurements with $B \to D^{*-} a_1^+$. An introduction to the partial wave analysis technique adopted in this thesis to study the 3 pions system is given in section 3.6.

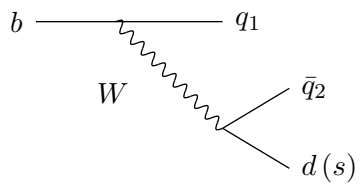

Figure 3.2: Tree diagrams ($q_1, q_2 \in \{u, c\}$).

3.2 Non-leptonic B decays

Studies of non-leptonic decays of B mesons are very useful to gain a better understanding of the dynamics of strong interactions, which are responsible for the bounding of quarks and gluons into hadrons. The complexity of the processes involved in non-leptonic decays is illustrated in fig 3.1 where it is shown how strong interactions of quarks can affect a simple $b \to c\ \overline{u}\ d$ tree diagram. The theoretical approach to these decays is based on low energy effective Hamiltonians which are calculated by making use of the "Operator Product Expansion" [31]. In this framework the factorization prescription [32] allows us to write the decay amplitudes in terms of a product of hadronic current matrix elements. Here are summarized the main concepts of this approach[1].

3.2.1 Classification

The most complicated B decays are the non-leptonic transitions, which are mediated by $b \to q_1\,\bar{q}_2\,d\,(s)$ quark-level processes, with $q_1, q_2 \in \{u, d, c, s\}$. There are two kinds of topologies contributing to such decays: tree-diagram-like and "penguin" topologies. The latter consist of gluonic (QCD) and electroweak (EW) penguins. In Figs. 3.2–3.4, the corresponding leading-order Feynman diagrams are shown. Depending on the flavor content of their final states, we may classify $b \to q_1\,\bar{q}_2\,d\,(s)$ decays as follows:

- $q_1 \neq q_2 \in \{u, c\}$: *only* tree diagrams contribute (class I).
- $q_1 = q_2 \in \{u, c\}$: tree *and* penguin diagrams contribute (class II).

[1] the discussion in this section follows an interesting review from Robert Fleisher[33]

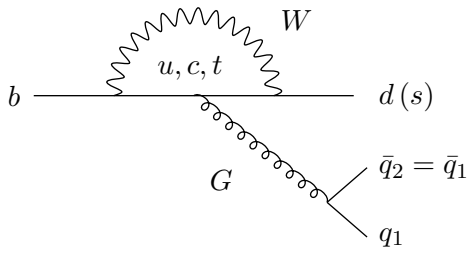

Figure 3.3: QCD penguin diagrams ($q_1 = q_2 \in \{u, d, c, s\}$).

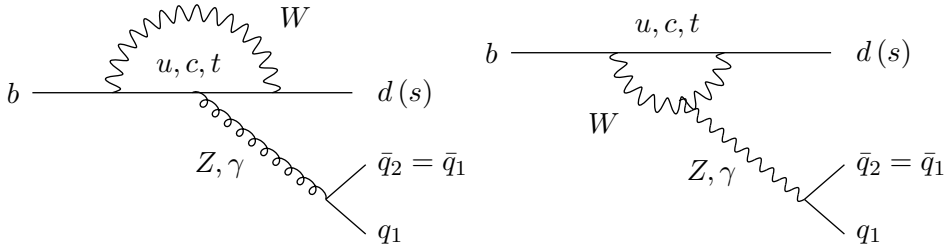

Figure 3.4: Electroweak penguin diagrams ($q_1 = q_2 \in \{u, d, c, s\}$).

- $q_1 = q_2 \in \{d, s\}$: *only* penguin diagrams contribute (class III).

3.2.2 Low-Energy Effective Hamiltonians

In order to analyze non-leptonic B decays theoretically, one uses low-energy effective Hamiltonians, which are calculated by making use of the "operator product expansion", yielding transition matrix elements of the following structure:

$$\langle f|\mathcal{H}_{\rm eff}|i\rangle = \frac{G_{\rm F}}{\sqrt{2}}\lambda_{\rm CKM}\sum_k C_k(\mu)\langle f|Q_k(\mu)|i\rangle\,. \tag{3.1}$$

The technique of the operator product expansion allows us to separate the short-distance contributions to this transition amplitude from the long-distance ones, which are described by perturbative quantities $C_k(\mu)$ ("Wilson coefficient functions") and non-perturbative quantities $\langle f|Q_k(\mu)|i\rangle$ ("hadronic matrix elements"), respectively. Here $G_{\rm F}$ is the Fermi constant, whereas $\lambda_{\rm CKM}$ is a CKM factor and μ denotes an appropriate renormalization scale. The Q_k are local operators,

which are generated by electroweak interactions and QCD, and govern "effectively" the decay in question. The Wilson coefficients $C_k(\mu)$ can be considered as scale-dependent couplings related to the vertexes described by the Q_k.

In order to illustrate this rather abstract formalism, let us consider the decays of the type $\bar{B}^0_d \to D^{(*)+}h^-$, which allow a transparent discussion of the evaluation of the corresponding low-energy effective Hamiltonian. Since this transition originates from a $b \to c\bar{u}d$ quark-level process, it is a pure "tree" decay, i.e. we do not have to deal with penguin topologies, which simplifies the analysis considerably. The leading-order Feynman diagram contributing to $\bar{B}^0_d \to D^{(*)+}h^-$ is illustrated in figure 3.1. Evaluating the Feynman diagram describing the weak transition yields

$$-\frac{g_2^2}{8}V_{ud}^*V_{cb}\left[\bar{s}\gamma^\nu(1-\gamma_5)u\right]\left[\frac{g_{\nu\mu}}{k^2-M_W^2}\right]\left[\bar{c}\gamma^\mu(1-\gamma_5)b\right]. \tag{3.2}$$

Because of $k^2 \sim m_b^2 \ll M_W^2$, it is possible to "integrate out" the W boson, and arrive at

$$\begin{aligned}\mathcal{H}_{\text{EFF}} &= \frac{G_\text{F}}{\sqrt{2}}V_{ud}^*V_{cb}\left[\bar{d}_\alpha\gamma_\mu(1-\gamma_5)u_\alpha\right]\left[\bar{c}_\beta\gamma^\mu(1-\gamma_5)b_\beta\right]\\ &= \frac{G_\text{F}}{\sqrt{2}}V_{ud}^*V_{cb}(\bar{d}_\alpha u_\alpha)_{\text{V-A}}(\bar{c}_\beta b_\beta)_{\text{V-A}} \equiv \frac{G_\text{F}}{\sqrt{2}}V_{ud}^*V_{cb}O_2\,,\end{aligned} \tag{3.3}$$

where α and β denote the color indices of the $SU(3)_\text{C}$ gauge group of QCD. Effectively, the $b \to c\bar{u}d$ decay process is now described by the "current–current" operator O_2.

Taking the QCD corrections into account, operator mixing induces a second "current–current" operator, which is given by

$$O_1 \equiv \left[\bar{d}_\alpha\gamma_\mu(1-\gamma_5)u_\beta\right]\left[\bar{c}_\beta\gamma^\mu(1-\gamma_5)b_\alpha\right]. \tag{3.4}$$

Consequently, a low-energy effective Hamiltonian of the following structure is obtained:

$$\mathcal{H}_\text{eff} = \frac{G_\text{F}}{\sqrt{2}}V_{ud}^*V_{cb}\left[C_1(\mu)O_1 + C_2(\mu)O_2\right], \tag{3.5}$$

where $C_1(\mu) \neq 0$ and $C_2(\mu) \neq 1$ are due to QCD renormalization effects [34]. These coefficients can be evaluated by first calculating the QCD corrections to the decay processes both in the full theory (i.e. with W exchange) and in the effective theory (where the W is integrated out) and then express the QCD-corrected transition amplitude in terms of QCD-corrected matrix elements and Wilson coefficients as in (3.1). This procedure is called "matching" between the full and the effective theory. The μ dependence of the Wilson coefficients assures that the physics is independent of the renormalization scale. However, an appropriate choice of μ permits to disentangle the

physics of hard QCD interactions from the physics of soft gluon exchanges. Indeed, the effects of heavy degrees of freedom, which have been integrated out of the theory, are included in the coefficients C_i. They therefore need to be evaluated at a scale μ where perturbative expansion is possible. The effects of long-distance interactions, instead, are included in the hadronic matrix elements $\langle D^{(*)+} h^- | O_i | B \rangle$ and cannot be evaluated by perturbative methods.

Non leptonic decays belonging to the class II of the classification shown in section 3.2.1 receives contributions both from tree and from penguin topologies. In this case, the operator basis is much larger than in the class I decays, where only the "tree" decay contributes. In this case the effective Hamiltonian can be written as:

$$\mathcal{H}_{\text{eff}} = \frac{G_{\text{F}}}{\sqrt{2}} \left[\sum_{j=u,c} V_{jr}^* V_{jb} \left\{ \sum_{k=1}^{2} C_k(\mu)\, Q_k^{jr} + \sum_{k=3}^{10} C_k(\mu)\, Q_k^r \right\} \right]. \tag{3.6}$$

Here another quark-flavor label $j \in \{u, c\}$ has been introduced, and the Q_k^{jr} can be classified as follows:

- Current–current operators:

$$\begin{array}{rcl} Q_1^{jr} & = & (\bar{r}_\alpha j_\beta)_{\text{V–A}} (\bar{j}_\beta b_\alpha)_{\text{V–A}} \\ Q_2^{jr} & = & (\bar{r}_\alpha j_\alpha)_{\text{V–A}} (\bar{j}_\beta b_\beta)_{\text{V–A}}. \end{array} \tag{3.7}$$

- QCD penguin operators:

$$\begin{array}{rcl} Q_3^r & = & (\bar{r}_\alpha b_\alpha)_{\text{V–A}} \sum_{q'} (\bar{q}'_\beta q'_\beta)_{\text{V–A}} \\ Q_4^r & = & (\bar{r}_\alpha b_\beta)_{\text{V–A}} \sum_{q'} (\bar{q}'_\beta q'_\alpha)_{\text{V–A}} \\ Q_5^r & = & (\bar{r}_\alpha b_\alpha)_{\text{V–A}} \sum_{q'} (\bar{q}'_\beta q'_\beta)_{\text{V+A}} \\ Q_6^r & = & (\bar{r}_\alpha b_\beta)_{\text{V–A}} \sum_{q'} (\bar{q}'_\beta q'_\alpha)_{\text{V+A}}. \end{array} \tag{3.8}$$

- EW penguin operators (the $e_{q'}$ denote the electrical quark charges):

$$\begin{array}{rcl} Q_7^r & = & \frac{3}{2} (\bar{r}_\alpha b_\alpha)_{\text{V–A}} \sum_{q'} e_{q'} (\bar{q}'_\beta q'_\beta)_{\text{V+A}} \\ Q_8^r & = & \frac{3}{2} (\bar{r}_\alpha b_\beta)_{\text{V–A}} \sum_{q'} e_{q'} (\bar{q}'_\beta q'_\alpha)_{\text{V+A}} \\ Q_9^r & = & \frac{3}{2} (\bar{r}_\alpha b_\alpha)_{\text{V–A}} \sum_{q'} e_{q'} (\bar{q}'_\beta q'_\beta)_{\text{V–A}} \\ Q_{10}^r & = & \frac{3}{2} (\bar{r}_\alpha b_\beta)_{\text{V–A}} \sum_{q'} e_{q'} (\bar{q}'_\beta q'_\alpha)_{\text{V–A}}. \end{array} \tag{3.9}$$

The current–current, QCD and EW penguin operators are related to the tree, QCD and EW penguin processes shown in Figs. 3.2–3.4. At a renormalization scale $\mu = \mathcal{O}(m_b)$, the Wilson coefficients of the current–current operators are $C_1(\mu) = \mathcal{O}(10^{-1})$ and $C_2(\mu) = \mathcal{O}(1)$, whereas those of the penguin operators are $\mathcal{O}(10^{-2})$ [35, 36].

The low-energy effective Hamiltonians discussed above apply to all B decays that are caused by the same quark-level transition, i.e. they are "universal". Consequently, the differences between the various exclusive modes of a given decay class arise within this formalism only through the hadronic matrix elements of the relevant four-quark operators. Unfortunately, the evaluation of such matrix elements is associated with large uncertainties and is a very challenging task. In this context, "factorization" is a widely used concept, and will be illustrated in the following subsection.

3.2.3 Factorization of Hadronic Matrix Elements

In order to discuss "factorization", let us consider once more the decays of type $\bar{B}^0_d \to D^{(*)+}h^-$. The corresponding transition amplitude contains the hadronic matrix elements of the $O_{1,2}$ operators between the $\langle h^- D^{(*)+}|$ final and the $|\bar{B}^0_d\rangle$ initial states. If we use the well-known $SU(N_{\rm C})$ color-algebra relation

$$T^a_{\alpha\beta}T^a_{\gamma\delta} = \frac{1}{2}\left(\delta_{\alpha\delta}\delta_{\beta\gamma} - \frac{1}{N_{\rm C}}\delta_{\alpha\beta}\delta_{\gamma\delta}\right) \tag{3.10}$$

to rewrite the operator O_1, we obtain

$$\langle h^- D^{(*)+}|\mathcal{H}_{\rm eff}|\bar{B}^0_d\rangle = \frac{G_{\rm F}}{\sqrt{2}}V^*_{ud}V_{cb}\Big[a_1\langle h^- D^{(*)+}|(\bar{d}_\alpha u_\alpha)_{\rm V\text{–}A}(\bar{c}_\beta b_\beta)_{\rm V\text{–}A}|\bar{B}^0_d\rangle$$

$$+2\,C_1\langle h^- D^{(*)+}|(\bar{d}_\alpha\, T^a_{\alpha\beta}\, u_\beta)_{\rm V\text{–}A}(\bar{c}_\gamma\, T^a_{\gamma\delta}\, b_\delta)_{\rm V\text{–}A}|\bar{B}^0_d\rangle\Big],$$

with

$$a_1 = C_1/N_{\rm C} + C_2 \sim 1. \tag{3.11}$$

The "factorization" of the hadronic matrix elements is given by:

$$\begin{aligned}
&\langle h^- D^{(*)+}|(\bar{d}_\alpha u_\alpha)_{\rm V\text{–}A}(\bar{c}_\beta b_\beta)_{\rm V\text{–}A}|\bar{B}^0_d\rangle\big|_{\rm fact} \\
&\quad = \langle h^-|\left[\bar{d}_\alpha\gamma_\mu(1-\gamma_5)u_\alpha\right]|0\rangle\langle D^{(*)+}|\left[\bar{c}_\beta\gamma^\mu(1-\gamma_5)b_\beta\right]|\bar{B}^0_d\rangle \\
&\quad = \underbrace{if_h}_{\text{decay constant}} \times \underbrace{F_0^{(BD)}(M_K^2)}_{B\to D\text{ form factor}} \times \underbrace{(M_B^2 - M_D^2),}_{\text{kinematical factor}}
\end{aligned} \tag{3.12}$$

$$\langle h^- D^{(*)+} | (\bar{d}_\alpha \, T^a_{\alpha\beta} \, u_\beta)_{\text{V–A}} (\bar{c}_\gamma \, T^a_{\gamma\delta} \, b_\delta)_{\text{V–A}} | \bar{B}^0_d \rangle \big|_{\text{fact}} = 0. \tag{3.13}$$

The quantity a_1 is a phenomenological "color factor", which governs "color-allowed" decays; the decays $\bar{B}^0_d \to D^{(*)+} h^-$ belongs to this category, since the color indexes of the h^- meson and the $\bar{B}^0_d$–$D^{(*)+}$ system run independently from each other in the corresponding leading-order diagram. On the other hand, in the case of "color-suppressed" modes, for instance $\bar{B}^0_d \to \pi^0 D^0$, where only one color index runs through the whole diagram, we have to deal with the combination

$$a_2 = C_1 + C_2/N_{\text{C}} \sim 0.25. \tag{3.14}$$

The concept of factorizing the hadronic matrix elements of four-quark operators into the product of hadronic matrix elements of quark currents has a long history [37], and can be justified, for example, in the large-N_{C} limit [38]. Interesting recent developments are the following:

- "QCD factorization" [39], which is in accordance with the old picture that factorization should hold for certain decays in the limit of $m_b \gg \Lambda_{\text{QCD}}$ [40], provides a formalism to calculate the relevant amplitudes at the leading order of a Λ_{QCD}/m_b expansion. The resulting expression for the transition amplitudes incorporates elements both of the naïve factorization approach sketched above and of the hard-scattering picture. Let us consider a decay $\bar{B} \to M_1 M_2$, where M_1 picks up the spectator quark. If M_1 is either a heavy (D) or a light (π, K) meson, and M_2 a light (π, K) meson, QCD factorization gives a transition amplitude of the following structure:

  $$A(\bar{B} \to M_1 M_2) = [\text{"naïve factorization"}] \times [1 + \mathcal{O}(\alpha_s) + \mathcal{O}(\Lambda_{\text{QCD}}/m_b)] \, . \tag{3.15}$$

  While the $\mathcal{O}(\alpha_s)$ terms, i.e. the radiative non-factorizable corrections, can be calculated systematically, the main limitation of the theoretical accuracy originates from the $\mathcal{O}(\Lambda_{\text{QCD}}/m_b)$ terms.

- Another QCD approach to deal with non-leptonic B-meson decays – the "perturbative hard-scattering approach " (PQCD) – was developed independently in [41], and differs from the QCD factorization formalism in some technical aspects.

- A very useful technique for "factorization proofs" is provided by the framework of the "soft collinear effective theory" (SCET) [42].

- Non-leptonic B decays can also be studied within QCD light-cone sum-rule approaches [43].

Despite factorization gives reliable results in describing several processes, in particular in the extended form of QCD-factorization [37], recently there have been found cases in which large non-factorizable corrections [44, 45] are present, as in $B \to \pi\pi$ and $B \to \phi K^*$ decays. It is very important to quantitatively test the limits of factorization in depth in order to improve our knowledge on the strong interaction effects in exclusive weak decays of the B mesons.

3.3 The $a_1(1260)$

The $a_1(1260)$ particle is an axial vector meson whose quantum numbers are $I^G(J^{PC}) = 1^-(1^{++})$. It was discovered as a broad $\rho - \pi$ resonance in 1964 in pion-proton scattering scattering experiments [46], and it remains nowadays poorly known due to the discordant measurements of its parameters. The present status of our knowledge of this resonance come from two kind of experiments: hadronic production and τ decays.

The first class of experiments comprises diffractive and charge exchange production with incident pions on fixed target and central production in pp collisions. These experiments are characterized by very high statistics but are made difficult by the presence of high physical backgrounds due to the other spin parity resonances contributing to the three pions system.

The decay $\tau^- \to [3\pi]^-\nu_\tau$ provides a cleanest environment to study the a_1 meson. Because of the transformation properties of the weak current under parity and G-parity, τ lepton decay to an odd number of pions is expected to occur exclusively through the axial vector current, ignoring isospin-violating effects. Thus the only possible spin-parity quantum numbers for 3π system in this decay are $J^P = 0^-$ or 1^+, simplifying the analysis with respect to the hadronic production. However, due the small mass difference between the τ and the a_1, a kinematic cutoff prevent to fully exploit the high mass tail of the 3 pion spectrum.

In table 3.1 are reported the results of the measurements of the mass and width of the a_1 meson. Despite the models adopted by the various experiments to fit the a_1 line-shape are different, the discrepancies between the measurements can be only partly attributed to model dependent systematic uncertainties. In particular the measurements of the width assume values that vary between 230$\pm$50 MeV [47] and 814$\pm$36$\pm$13 [48]. For this reason the PDG has chosen to don't perform an average of the available measurements of the a_1 mass and width and provides a conservative

Experiment	mass measurement	width measurement
CLEO	1331±10± 3 MeV	814± 36± 13 MeV
DELPHI (1)	1255± 7± 6 MeV	587± 27± 21 MeV
DELPHI (2)	1207± 5± 8 MeV	478± 3± 15 MeV
DELPHI (3)	1196± 4± 5 MeV	245± 14± 8 MeV
OPAL (1)	1262± 9± 7 MeV	621± 32± 58 MeV
OPAL (1)	1210± 7± 2 MeV	457± 15± 17 MeV
ARGUS	1211± 7^{+50}_{-0} MeV	446± 21^{+140}_{-0} MeV
KEK	1121± 8 MeV	266± 13 MeV
DELCO	1242± 37 MeV	465^{+228}_{-143} MeV
MARK-II	1260± 14 MeV	298^{+40}_{-34} MeV
ARGUS (2)	1250± 9 MeV	488 ± 32 MeV
WA76	1208± 15 MeV	430±50 MeV
WA103	1240± 10 MeV	400±35 MeV
MAC	1166± 18± 11 MeV	405±75±17 MeV
AMST (1)	1280± 30 MeV	300±50 MeV
AMST (2)	1041± 13 MeV	230±50 MeV
ISGUR reanalysis of ARGUS(2)-MARK-II-DELCO	1220± 15	420±40 MeV
BOWLER reanalysis of ARGUS(2)-AMST(1)	1260± 25	396±43 MeV

Table 3.1: Available measurements of the a_1 mass and width as reported from the Particle Data Group [13]

estimate of their values:

$$\begin{array}{lll} m_{a_1}^{PDG} & = & 1230 \pm 40\text{MeV} \\ \Gamma_{a_1}^{PDG} & \text{between} & 250 \text{ and } 600\text{MeV}. \end{array} \tag{3.16}$$

In the present work we present a measurement of the a_1 parameters in a different environment: the production through $B \to D^{*-}a_1^+$ ($\to \pi^+\pi^+\pi^-$) decays.

The high branching ratio for this process ($\sim 1\%$) and the kinematic constraints coming from the reconstruction of the full B meson decay chain, make this channel a quite clean environment to study the a_1 meson. Weak current structure together with factorization predicts that the main contribution to the 3 pions system produced in $B \to D^{*-}\pi^+\,\pi^+\,\pi^-$ is due to the $J^P = 1^+$ state, i.e. to the a_1. However contributions from $J^P = 0^-$ states are possible and factorization breaking effects can induce also spin 2 states. For this reason a Dalitz plot analysis of the 3 pions system is needed to separate the different spin parity components (section 3.6). This kind of analysis also allow us to study the intermediate resonance contributing to the process $a_1 \to \pi\pi\pi$ through the decay chain $a_1 \to X\pi$, $X \to \pi\pi$, as was recently done by a CLEO analysis [48] of the a_1 produced in τ decays. They found significant contributions of $\sigma\pi$, $f_0(1370)\pi$ and $f_2(1270)\pi$ in addition to the dominant $\rho\pi$ amplitude.

3.4 Polarization in $B \to D^{*-}a_1^+$

As recently suggested in [27], decay processes of the type $B \to$VA, involving vector and axial mesons in the final state can be used to provide a test of factorization. The $B \to D^{*-}a_1^+$ decay belong to this kind of processes and, due to its high branching ratio, is the best candidate to perform the proposed factorization test.

The decay amplitude for $B \to D^{*-}a_1^+$ can be written as a sum over polarization of weak decay amplitudes, multiplying corresponding strong decay amplitudes A_i for $a_1^+ \to \pi^+\,\pi^+\,\pi^-$ (i = $0, +, -$),

$$A(B^0 \to D^{*-}\pi^+(p_1)\pi^+(p_2)\pi^-(p_3)) = \Sigma_{i=0,+,-} H_i A_i. \tag{3.17}$$

The dominant process contributing to $a_1^+ \to \pi^+\,\pi^+\,\pi^-$ is $a_1^+ \to \rho^0\pi^+$, $\rho^0 \to \pi^+\pi^-$,

$$A_i = A_i(a_1^+ \to \rho^0\pi^+(p_2)) + A_i(a_1^+ \to \rho^0\pi^+(p_1)),$$

where the two terms correspond to the two possible ways of forming a ρ meson from $\pi^+ \pi^-$ pairs. The $a_1\rho\pi$ coupling can be written in terms of two invariant amplitudes,

$$A(a_1(p,\epsilon) \to \rho(p',\epsilon')\pi) = A(\epsilon \cdot \epsilon'^*) + B(\epsilon \cdot p')(\epsilon'^* \cdot p),$$

where (p,ϵ) and (p',ϵ') are the momenta and polarization vectors of the a_1 and ρ respectively. A and B can be related with the S and D-wave amplitudes by [49]:

$$\begin{aligned} A &= A_S + \tfrac{1}{\sqrt{(2)}} A_D \\ B &= \big[-\big(1 - \tfrac{m_\rho}{E_\rho}\big) A_S - \big(\ + 2\tfrac{m_\rho}{E_\rho}\big) \tfrac{1}{\sqrt{(2)}} A_D \big] \tfrac{E_\rho}{m_\rho \vec{p}_\rho^{\,2}}, \end{aligned} \tag{3.18}$$

where the ρ energy and momentum are given in the a_1 rest frame.
The strong decay amplitude $a_1^+ \to \pi^+ \pi^+ \pi^-$ is obtained by convoluting the $a_1^+ \to \rho^0 \pi^+$ with the amplitude for $\rho^0(\epsilon') \to \pi^+(p_i)\pi^-(p_j)$ which is proportional to $\epsilon' \cdot (p_i - p_j)$. One finds:

$$A(a_1^+(p,\epsilon) \to \pi^+(p_1)\pi^+(p_2)\pi^-(p_3)) \propto C(s_{13}, s_{23})\epsilon \cdot p_1 + (p_1 \leftrightarrow p_2),$$

where $s_{ij} = (p_i + p_j)^2$ and :

$$C(s_{13}, s_{23}) = \big[A + B m_{a_1}(E_3 - E_2)\big] B_\rho(s_{23}) + 2A B_\rho(s_{13}).$$

Here $B_\rho(s_{ij}) = (s_{ij} - m_\rho^2 - i m_\rho \Gamma_\rho)^{-1}$, and pion energies are given in the a_1 rest frame.
In the a_1 rest frame the three pions are emitted in a plane whose normal unit vector is $\hat{n} \equiv (\vec{p_1} \times \vec{p_2})/|\vec{p_1} \times \vec{p_2}|$. The B decay amplitude into final hadronic states depends on the angle θ between $\hat{n}$ and the direction $\hat{z}$ opposite to the D^* (or B) momentum, and on other two angles ϕ and ψ. ϕ is an angle in the a_1 decay plane (I), defining the direction of one of the three pions (say p_3), while ψ define the line of intersection of the D^* decay plane with a plane(II) perpendicular to $\hat{z}$. Both ϕ and ψ are measured with respect to the line of intersection of the two planes I and II. With these notations, squaring the amplitude 3.17 and integrating over ϕ and ψ one finds the following expression for the decay distribution in θ:

$$\begin{aligned} \int\int d\phi d\psi |A(B \to D^* 3\pi)|^2 &\propto |H_0|^2 \sin^2\theta |\vec{J}|^2 \\ &+ (|H_+|^2 + |H_-|^2)\tfrac{1}{2}(1 + \cos^2\theta)|\vec{J}|^2 \\ &+ (|H_+|^2 - |H_-|^2)\cos\theta Im\big[(\vec{J} \times \vec{J}^*) \cdot \hat{n}\big]. \end{aligned} \tag{3.19}$$

The vector $\vec{J}$ is defined in the rest frame of the a_1 resonance,

$$\vec{J} = C(s_{12}, s_{13})\vec{p_1} + C(s_{23}, s_{13})\vec{p_2}.$$

A fit to the angular decay distribution 3.19 enables separate measurements of the three terms $|H_0|^2$, $|H_+|^2 + |H_-|^2$, $|H_+|^2 - |H_-|^2$.
The three helicity amplitudes $H_{0,\pm}$ in $B \to D^{*-}a_1^+$ can be calculated using factorization [32] and heavy quark symmetry [50]. The theoretical predictions reported in [27] are:

$$\begin{aligned} H_0 &= -\frac{G_F}{\sqrt{(2)}} V_{cb}V_{ud}^* c_1(D^*a_1) f_{a_1} \sqrt{(}m_B m_{D^*}) \\ &\times \frac{m_B - m_D^*}{m_{a_1}}(y+1)\xi(y), \\ H_\pm &= \frac{G_F}{\sqrt{(2)}} V_{cb}V_{ud}^* c_1(D^*a_1) f_{a_1} \sqrt{(}m_B m_{D^*}) \\ &\times \big[-(y+1) \pm \sqrt{(}y^2-1)\big]\xi(y) \end{aligned} \tag{3.20}$$

Here $\xi(y)$ is the value of the Isgur-Wise function [50] at $y = (m_B^2 + m_{D^*}^2 - m_{a_1}^2)/(2m_B m_{D^*}) = 1.43$, f_{a_1} is the a_1 decay constant and $c_1(D^*a_1)$ is a QCD factor which is close to one. The numerical values of these factors do not affect the polarization prediction, for which one uses the normalization $|H_0|^2 + |H_+|^2 + |H_-|^2 = 1$:

$$|H_0|^2 = 0.75; \qquad |H_0|^2 = 0.21; \qquad |H_-|^2 = 0.04.$$

These predictions, obtained in factorization, can be tested by measuring the polarization squared moduli $|H_i|^2$ by means of a fit to the decay angular distribution in θ defined in equation 3.19.

3.5 CP violation in $B \to D^{*-}a_1^+$

In section 1.5 we have seen how it is possible to extract the Unitarity Triangle parameter $2\beta + \gamma$ by measuring the CP asymmetries in $B \to D^{(*)}h$ decays.
The BABAR and Belle collaborations have recently published measurements of $\sin(2\beta + \gamma)$ with this method, using the $B \to D\,\pi$, $B \to D^*\pi$ and $B \to D\,\rho$ decay channels [51, 52, 53, 54]. One important limit of these analyises come from the uncertainty on the ratio of magnitudes of the suppressed and favored amplitudes, e.g. for the $B \to D\,\pi$ channel:

$$r_{D\pi} = \frac{|A(B^0 \to D^+\pi^-)|}{|A(\bar{B}^0 \to D^+\pi^-)|} \tag{3.21}$$

Each of the ratios $r_{D\pi}$, $r_{D^*\pi}$ and $r_{D\rho}$ is expected to be about $\mathcal{O}(10^-2)$ but a precise determination is very difficult, since the doubly Cabibbo suppressed amplitude is not directly accessible due the the small branching ratio and the huge background from the favored channel. Current estimations

for these ratios come from the decay rate measurements of the corresponding charged B decays, (e.g. $B^+ \to D^+\pi^0$) using isospin symmetry, or from self-tagging decays with strangeness (e.g. $B^0 \to D_s^+\pi^-$) using SU(3). In the latter case, the theoretical uncertainties are hard to quantify.
For the $B \to VV$ and $B \to VA$ (vector-vector and vector-axial vector finale states) channels, it is possible to overcome this problem [26].
By expliciting the three polarization amplitudes for the CKM favored and suppressed amplitudes, we obtain the following expressions:

$$\begin{array}{rcrcl} A & \equiv & A(B^0 \to f) & = & \sum_{i=0,\|,\perp} H_i A_i, \\ \bar{A} & \equiv & A(\bar{B}^0 \to f) & = & \sum_{i=0,\|,\perp} h_i A_i. \end{array} \tag{3.22}$$

For the $B^0 \to D^{*-}a_1^+$ the A_i are calculable complex functions of the angles θ, ψ and ϕ defined in the previous section. Following the procedure described in sections 1.4 and 1.5 one arrives at the following time-dependent rate:

$$\begin{array}{rcl} \Gamma(B^0(t) \to f) & \propto & (|A|^2 + |\bar{A}|^2) + (|A|^2 - |\bar{A}|^2)\cos(\Delta m t) + \\ & & 2Im(e^{2i\beta} A \bar{A}^*)\sin(\Delta m t). \end{array} \tag{3.23}$$

The three coefficients in this expression, involve bilinear expressions in H_i and h_i multiplying calculable functions if the angle variables. The constant and $\cos\Delta mt$ terms in 3.23 determine the real and imaginary parts of $H_i H_j^*$ (and $h_i h_j^*$) for all pairs of transversity amplitude, while the coefficient of $\sin\Delta mt$ contains terms

$$Im\Big[e^{2i\beta}(H_i h_j^* + H_j h_i^*)\Big] Re(A_i A_j^*) + Re\Big[e^{2i\beta}(H_i h_j^* - H_j h_i^*)\Big] Re(A_i A_j^*). \tag{3.24}$$

Writing $H_i = |H_i|e^{i\Delta_i}$, $h_i = |h_i|e^{i\delta_i}e^{-i\gamma}$, where Δ_i and δ_i are the strong interaction phases, and using the above and similar information from $B^0(t) \to \bar{f}$ it is possible to show (see [27] and [26] for details) that a fit to the time dependent angular distributions allows to extract $(2\beta + \gamma)$, without using information on the CKM suppressed decay rate and free of the discrete ambiguities discussed in section 1.5.

3.6 Partial wave analysis for the 3 pions system

The work presented in this thesis focus on the study of the 3 pions system produced in the $B \to D^{*+}\pi^+\,\pi^-\,\pi^-$ decay.

In this section the problem of the 3 body decay will be discussed. We'll first construct a three-particle system in a definite angular momentum state and then apply the formalism to a case of a resonance decaying into three particles. Finally, we'll see how a partial wave analysis can be used to identify the different spin parity components contributing to the 3 pions system.
A complete discussion on these topics can be found in [55].

3.6.1 Notations

In the following, we will denote by $|j, m\rangle$ the single particle at rest state, where j is the spin and m is the z-component of the spin.
A finite rotation of a physical system (with respect to fixed coordinate axes) may be denoted by $R(\alpha, \beta, \gamma)$ where α, β, and γ are the standard Euler angles. To each R, there corresponds a unitary operator $U[R]$, which acts on the states $|j, m\rangle$. The angular momentum operators are the infinitesimal generators of the rotations:

$$U[R(\alpha, \beta, \gamma)] = e^{-i\alpha J_z} e^{-i\beta J_y} e^{-i\gamma J_z}. \tag{3.25}$$

The rotation of a state $|j, m\rangle$ is given by:

$$U[R(\alpha, \beta, \gamma)]|j, m\rangle = |\sum_{m'} |j, m'\rangle D^j_{m'm}(\alpha, \beta, \gamma), \tag{3.26}$$

where $D^j_{m'm}(R)$ is the standard rotation matrix [56]:

$$\begin{aligned} D^j_{m'm}(R) \equiv D^j_{m'm}(\alpha, \beta, \gamma) &= \langle j, m'|U[R]|j, m\rangle \\ &= e^{-im'\alpha} d^j_{m'm}(\beta) e^{-im\gamma}, \end{aligned} \tag{3.27}$$

with:

$$d^j_{m'm}(\beta) = \langle j, m'|e^{-i\beta J_y}|j, m\rangle \tag{3.28}$$

An important property of the D functions is the orthonormality:

$$\int dR D^{j_1 *}_{\mu_1 m_1}(R) D^{j_2}_{\mu_2 m_2}(R) = \frac{8\pi^2}{2j_1 + 1} \delta_{j_1 j_2} \delta_{\mu_1 \mu_2} \delta_{m_1 m_2}, \tag{3.29}$$

where $dR = d\alpha d\cos\beta d\gamma$.

Relativistic one-particle state with momentum $\vec{p}$ may be obtained by applying on the states $|j,m\rangle$ an unitary operator which represent a Lorentz transformation that takes a particle at rest to a particle of momentum $\vec{p}$. There are two ways of doing this, leading to canonical and helicity descriptions of relativistic free particle states. If we denote with $U[L_z(p)]$ the operator representing the pure time-like Lorentz transformation along the z-axis and with $\hat{R}(\phi,\theta,0)$ the rotation taking the z-axis into the direction of $\vec{p}$ with spherical angles (θ,ϕ) the canonical state is defined by:

$$|\vec{p},jm\rangle = U[R(\hat{\phi,}\theta,0)]U[L_z(p)]U^{-1}[R(\hat{\phi,}\theta,0)]|j,m\rangle, \tag{3.30}$$

while the helicity state is:

$$|\vec{p},j\lambda\rangle = U[R(\hat{\phi,}\theta,0)]U[L_z(p)]|j,\lambda\rangle. \tag{3.31}$$

In the helicity states the quantization axis is rotated along the $\vec{p}$ direction. There is a simple connection between the canonical and helicity description. From the definitions above one finds:

$$|\vec{p},j\lambda\rangle = \sum_m D^j_{m\lambda}(\hat{R})|\vec{p},jm\rangle. \tag{3.32}$$

3.6.2 Three particle system

Consider a system of three particles and let's use the notations s_i, η_i, λ_i and w_i to indicate the spin, parity, helicity and mass of the particle i ($i = 1,2,3$). In the rest frame (r.f.) of the three particles, the momentum and energy of the particle i will be denoted by $\vec{p}_i$ and E_i. In the r.f., the "standard orientation" of the three-particle system is shown in figure 3.5. This coordinate system may be rotated by the Euler angles α, β, and γ to obtain a system with arbitrary orientation.
A system with standard orientation can be written:

$$|000,E_i\lambda_i\rangle = N\prod_{i=1}^{3}|\vec{p}_i,s_i\lambda_i\rangle, \tag{3.33}$$

where N is a normalization factor and $|\vec{p}_i,s_i\lambda_i\rangle$ are the single particle helicity states.
A three particle system with an arbitrary orientation in the r.f. can now be obtained by applying a rotation $R(\alpha,\beta,\gamma)$ to the state 3.33:

$$|\alpha\beta\gamma,E_i\lambda_i\rangle = U[R(\alpha,\beta,\gamma)]|000,E_i\lambda_i\rangle. \tag{3.34}$$

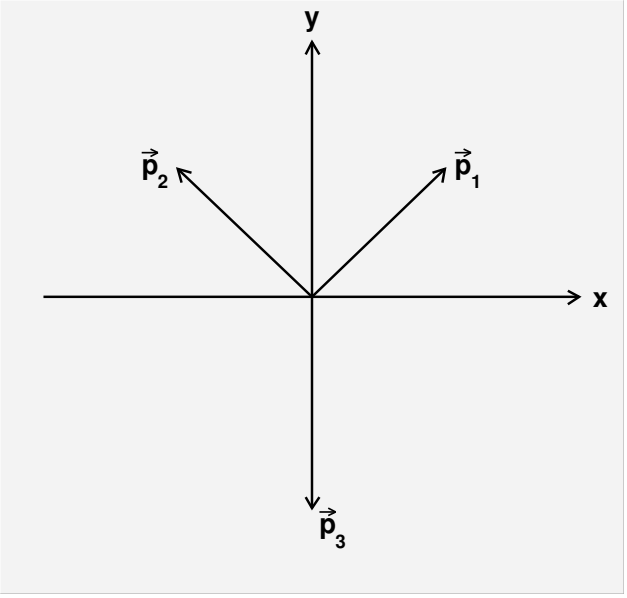

Figure 3.5: Standard orientation for the three particle rest system. Note that the y-axis is defined along the negative direction of $\vec{p}_3$, and the z-axis along $\vec{p}_1 \times \vec{p}_2$

It is now possible to build a state of definite angular momentum:

$$|JM\mu, E_i\lambda_i\rangle = \frac{N_J}{\sqrt{2\pi}} \int dR D^{j*}_{M\mu}(\alpha,\beta,\gamma)|\alpha\beta\gamma, E_i\lambda_i\rangle, \tag{3.35}$$

where N_J is a normalization constant. It can be shown that this state represents a definite angular momentum state by applying an arbitrary rotation R' and verifying that:

$$U[R']|JM\mu, E_i\lambda_i\rangle = \sum_{M'} D^J_{M'M}(R')|JM'\mu, E_i\lambda_i\rangle. \tag{3.36}$$

This relation also shows that in addition to the obvious invariants E_i and λ_i, the quantity μ is also an invariant. It represents the z-component of angular momentum whose quantization axis itself rotates under a rotation of the system.
Transformation under parity of the state 3.35 reads:

$$\Pi|JM\mu, E_i\lambda_i\rangle = \eta_1\eta_2\eta_3(-1)^{s_1+s_2+s_3-\mu}|JM\mu, E_i, -\lambda_i\rangle, \tag{3.37}$$

while the operator P_{12} which exchange the particle 1 and 2 acts on the system as follows:

$$P_{12}|JM\mu, E_i\lambda_i\rangle = (-1)^{J+\mu}|JM-\mu, E_2\lambda_2, E_1\lambda_1, E_3\lambda_3\rangle. \tag{3.38}$$

3.6.3 Three body decays

Let us consider a process in which a resonance with spin parity J^η and mass w decays into three particles. In the rest frame of the resonance (JRF), let the angles (α, β, γ) describe the orientation of the three particle system. The decay amplitude may be written:

$$\begin{aligned} A &= \langle \alpha\beta\gamma, E_i\lambda_i | \mathcal{M} | JM \rangle \\ &= \langle \alpha\beta\gamma, E_i\lambda_i | JM\mu E_i\lambda_i \rangle \langle JM\mu E_i\lambda_i | \mathcal{M} | JM \rangle \\ &= \frac{N_J}{\sqrt{2\pi}} F^J_\mu(E_i\lambda_i) D^{J*}_{M\mu}(\alpha\beta\gamma) \end{aligned} \tag{3.39}$$

If the "decay operator" $\mathcal{M}$ is rotationally invariant, the decay amplitude F should depend only on the rotational invariants, i.e.:

$$F^J_\mu(E_i\lambda_i) = \langle JM\mu E_i\lambda_i | \mathcal{M} | JM \rangle. \tag{3.40}$$

If parity is conserved (as in the strong interaction processes), F satisfy the symmetry:

$$F^J_\mu(E_i\lambda_i) = \eta\eta_1\eta_2\eta_3(-)^{s_1+s_2+s_3+\mu} F^J_\mu(E_i, -\lambda_i). \tag{3.41}$$

If particles 1 and 2 are identical: If parity is conserved (as in the strong interaction processes), F satisfy the symmetry:

$$F^J_\mu(E_1\lambda_1, E_2\lambda_2, E_3\lambda_3) = \pm(-)^{J+\mu} F^J_{-\mu}(E_2\lambda_2, E_1\lambda_1, E_3\lambda_3) \tag{3.42}$$

where the plus sign holds for identical bosons and the minus sign for fermions.

Let us consider now the case of interest for this thesis, i.e. the decay process $B^0 \to D^{*+} X^-$, $X^- \to \pi^+\pi^-\pi^-$ where, in principle, more resonances X_k with different spins and parities can be produced, each decaying into the three pions system.
Pions are pseudo-scalar mesons, so we have $s_i = 0$, $\lambda_i = 0$, $\eta_i = -1$, and their state is described by the three four-momenta p^μ_i. The three mass shell conditions

$$p^\mu_i p_{i\mu} = m^2_\pi, \tag{3.43}$$

and the constraints from the four-momentum conservation reduce the number of independent parameters from twelve to five.
In the X resonance rest frame the kinematical configuration of the system is given by the 3 Euler

angles (α, β, γ), describing the orientation of the system with respect to the "standard orientation" introduced in subsection 3.6.2, and by other two independent variables that can be choose in several different ways. Since the decay operator is invariant under rotations, the decay amplitude does not depend on the Euler angles but only on these other two variables. The scatter plot of these variables is called the "Dalitz plot" [57] of the three body decay. The most common used choice of the Dalitz plot variables is in terms of the invariants:

$$\begin{aligned} m_{12}^2 &= (p_1+p_2)^\mu (p_1+p_2)_\mu \\ m_{13}^2 &= (p_1+p_3)^\mu (p_1+p_3)_\mu. \end{aligned} \tag{3.44}$$

Four momentum conservation defines a kinematical allowed region for the Dalitz plot. The area of this region increase with the total mass w of the system. The kinematical bounds of the two variables above for a given value of w are defined by:

$$\begin{aligned} (m_1+m_2)^2 &<= m_{12}^2 <= (w-m_3)^2 \\ m_{13}^2[min](w, m_{12}^2) &<= m_{13}^2 <= m_{13}^2[max](w, m_{12}^2), \end{aligned} \tag{3.45}$$

where:

$$\begin{aligned} m_{13}^2[max](w, m_{12}^2) &= (E_2^* + E_3^*)^2 - \left(\sqrt{E_2^{*2} - m_2^2} - \sqrt{E_3^{*2} - m_3^2}\right)^2, \\ m_{13}^2[max](w, m_{12}^2) &= (E_2^* + E_3^*)^2 - \left(\sqrt{E_2^{*2} - m_2^2} + \sqrt{E_3^{*2} - m_3^2}\right)^2, \end{aligned} \tag{3.46}$$

with E_2^*= $(m_{12}^2 - m_1^2 + m_2^2)/2m_{12}$ and E_3^*= $(w^2 - m_{12}^2 - m_3^2)/2m_{12}$ representing the energies of the particles 2 and 3 in the m_{12} rest frame.

Another set of Dalitz variables is given by the pair (E_1, E_2) indicating the energies of the particles 1 and 2 in the resonance rest frame. The following considerations are independent of the particular choice of the Dalitz plot coordinates.

Suppose that two resonance with spins J_1 and J_2 are possible for the three pions system. From eq. 3.39 it's possible to derive the over-all amplitude:

$$m_{fi} \sim \sum_{M_1\mu_1} T_1 D^{J_1 *}_{M_1\mu_1}(\alpha, \beta, \gamma) F^{J_1}_{\mu_1}(E_1, E_2) + \sum_{M_2\mu_2} T_2 D^{J_2 *}_{M_2\mu_2}(\alpha, \beta, \gamma) F^{J_2}_{\mu_2}(E_1, E_2), \tag{3.47}$$

where T_i is the production amplitude for the resonance J_i. If $J_1 \neq J_2$, the Dalitz plot distribution is given by:

$$\frac{d\sigma}{dw dE_1 dE_2} \sim \sum_{M_1\mu_1} |T_1 F^{J_1}_{\mu_1}|^2 + \sum_{M_2\mu_2} |T_2 F^{J_2}_{\mu_2}|^2 \tag{3.48}$$

after integrating on the Euler angles and using the orthogonality of the D functions (eq.3.29). This shows that states of different spin does not interfere in the Dalitz plot distribution. If the two resonances have the same spin but opposite parities the integration over the Euler angles yields:

$$\frac{d\sigma}{dw dE_1 dE_2} \sim \sum_{M\mu} |T_1 F_\mu^J + T_2 \bar{F}_\mu^J|^2 \tag{3.49}$$

where $\bar{F}$ indicates a decay amplitude of opposite parity to that of F. Applying parity conservation, one may rewrite the equation above with a relative minus sign between the two terms, which means that the interference is identically zero, again obtaining the result 3.48.

In conclusion, we have seen that, as long as one integrates over the orientation of the three particle system, states of different spin-parity do not interfere with one another in a Dalitz plot analysis. This means that with a suitable model to describe the decay amplitudes $F_{\mu_i}^{J_i P_i}(w, E_1, E_2)$ (or equivalently $F_{\mu_i}^{J_i P_i}(w, m_{12}^2\,, m_{13}^2\,)$) it is possible to separate the different J^P contribution to the 3 pions system by fitting the experimental Dalitz plot distribution.

As will be shown in the next two chapters, in this thesis we have performed a Dalitz plot spin parity analysis to separate the dominant $J^P = 1^+$ contribution to the 3 pions system produced in $B \to D^{*-} \pi^+ \pi^+ \pi^-$ from other possible resonances. The model used to describe the decay amplitudes is the standard Isobar model and will be discussed in detail in the section 5.2. Since our goal is to measure the a_1 mass distribution, the 3 pions system mass spectrum is divided in several intervals, and the Dalitz plot analysis is performed in each bin.

Chapter 4

The $B \rightarrow D^{*-} a_1^+$ decay reconstruction

4.1 Introduction

This chapter describes the criteria adopted to select a sample of events mainly containing the $B \rightarrow D^{*-} a_1^+$ ($a_1^- \rightarrow \pi^+ \pi^- \pi^-$) signal decay.

The data analyzed were recorded in 1999-2004 and the integrated luminosity is 208.7 fb^{-1} corresponding to about 230 Million of $B\overline{B}$ pairs. Events are first pre-selected with loose requirements in order to reduce the amount of data in input to the analysis. B mesons are then reconstructed combining the decay daughters in the mode considered after reconstruction of the full decay chain. The D^{*+} is reconstructed via the decay chain $D^{*+} \rightarrow D^0\pi^+$, $D^0 \rightarrow K\pi$ ($K\pi\pi\pi$) and it is associated with a 3 pions system to form the B meson candidate.

A critical issue for this analysis is to suppress the combinatorial background, arising from random combination of the tracks from $e^+e^- \rightarrow q\overline{q}$ (q = u,d,s,c) or $e^+e^- \rightarrow B\overline{B}$ events. Backgrounds can be rejected on the basis of discriminating quantities whose distribution is different for signal and background events. In order to study the background properties, suitable control samples are selected on the experimental data.

The first step in the reconstruction process is the selection of $B\overline{B}$ events, which is described in Section 4.2. Section 4.3 describes the cuts applied to ensure a good reconstruction quality for the

final state tracks. Section 4.4 contains the particle identification criteria used to select the kaons and pions belonging to the decay chain. In section 4.5 are shown the selection cuts for the D^0 and D^{*+} mesons reconstruction. The final B selection and the discriminating variables used for the background suppression and characterization are presented in section 4.6.

4.2 Event selection

Production cross sections for the physics processes at the $\Upsilon(4S)$ energy were listed in Table 2.2. In addition to the $\Upsilon(4S) \to B\overline{B}$ decay, these processes include continuum $q\overline{q}$ and QED events such as $e^+e^- \to e^+e^-$,$\mu^+\mu^-$,$\tau^+\tau^-$, and $\gamma\gamma$. The event topology is significantly different for each type of processes. Table 4.1 summarizes the main characteristics of each process.

In order to reduce the amount of data in input to the analysis a pre-selection is applied which enhances the number of $B\overline{B}$ and B^+B^- events over the background from $q\overline{q}$ and QED processes.
A fiducial volume of the detector is defined as a region characterized by well-measured reconstruction efficiency and an accurate modeling of the detector material in the Monte Carlo (MC) simulations. The fiducial volume for tracks is $0.41 < \theta_{lab} < 2.54$ rad, while for neutrals is $0.41 < \theta_{lab} < 2.409$, where θ_{lab} is the polar angle in the laboratory frame.
The QED events are discriminated by selecting events with three well reconstructed charged tracks in the fiducial volume and a total visible energy W greater than 4.5 GeV.
The three tracks above are required to have at least 12 hits released in the Drift Chamber, to ensure that their momenta and dE/dx are well measured. In addition they are required to have transverse momentum $p_T > 100$ MeV/c, and to point back to the nominal interaction point within 1.5cm in the xy-plane and 3 cm along the z-axis. Moreover, the primary vertex, constructed from the tracks above, must be within 0.5 cm of the average position of the interaction point in the xy plane and within 6 cm in the z direction.
The visible energy W is defined as the sum of energies associated to all the charged tracks and neutral candidates detected in the fiducial volume.
The distributions of the number of well reconstructed charged tracks and of the visible energy W are shown in figures 4.1 and 4.2. The distributions are normalized to the same area, hence only the shapes are meaningful. The above requirements remove, almost entirely, the QED events and select the hadronic $B\overline{B}$ and continuum $q\overline{q}$ events.

Event type	Main characteristics
$e^+e^- \rightarrow e^+e^-$	Two high-momentum back-to-back tracks, and associated energy deposit in the EMC
$e^+e^- \rightarrow \mu^+\mu^-$	Two high-momentum back-to-back tracks
$e^+e^- \rightarrow \tau^+\tau^-$	Back-to-back topology with large missing energy, due neutrinos from semileptonic τ decays
$e^+e^- \rightarrow \gamma\gamma$	Large missing energy, and small number of tracks due to preferential production of particles along the beam direction
$e^+e^- \rightarrow q\overline{q}$ with q = u,d,s,c	Large number of hadrons and jet-like topology, due to the hadronization of the quarks which are produced back-to-back
$e^+e^- \rightarrow \Upsilon(4S)$	Large number of hadrons and isotropic topology due to the B decays

Table 4.1: *Main characteristics of the processes at the $\Upsilon(4S)$ energy*

In order to reduce the amount of continuum $q\overline{q}$ events the normalized second Fox-Wolfram moment [58] R_2 is used. The l^{th} Fox-Wolfram moment H_l is the momentum-weighted sum of Legendre polynomial of l^{th} order, computed from the cosine of the angle between all pairs of tracks:

$$H_l = \Sigma_{i,j} \frac{|p_i||p_j| P_l(cos\theta_{ij})}{E_{vis}^2}.$$

Each H_l is basically a multipole moment of the momentum distribution in an event. The H_0 moment is the analog of the electric charge distribution. The first moment H_1 is zero because the momentum is not a signed quantity (unlike the electric charge) and therefore can not have a dipole

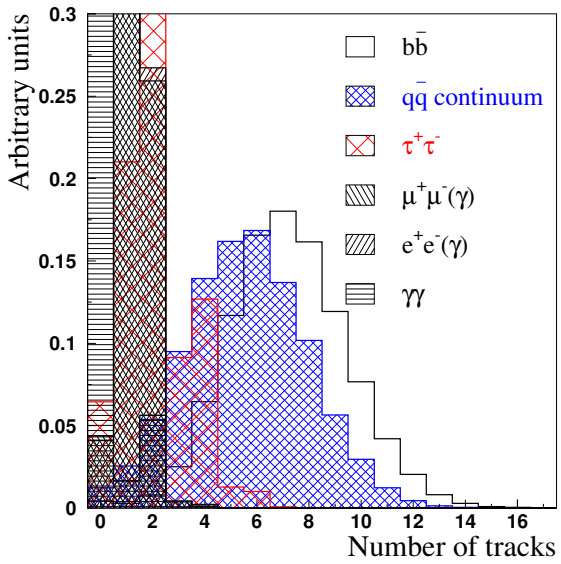

Figure 4.1: Distribution of the number of well reconstructed charged tracks in the main physics processes at the $\Upsilon(4S)$ energy. The distributions are normalized to the same area.

moment. The quadrupole moment H_2 can instead discriminate events with a jet-like structure of momentum ($q\overline{q}$ events) from those with a more spherically symmetric topology ($B\overline{B}$ events). The normalized ratio $R_2 = H_2/H_0$ is therefore very close to unity for events with back-to-back tracks such as QED events, and approaches 0 for isotropic events like $B\overline{B}$ events.
The distribution of R_2 for the physics processes at the $\Upsilon(4S)$ energy is shown in Figure 4.3.

The efficiency of the pre-selection described in this section on the $b\overline{b}$ events is 95.6% as estimated from the Monte Carlo simulation.

4.3 Tracks selection

The final state of the B meson decay chain is exclusively constituted of charged particles that are reconstructed by means of the BABAR tracking system (sec. 2.3).
Tracks selection criteria are summarized in Table 4.2.

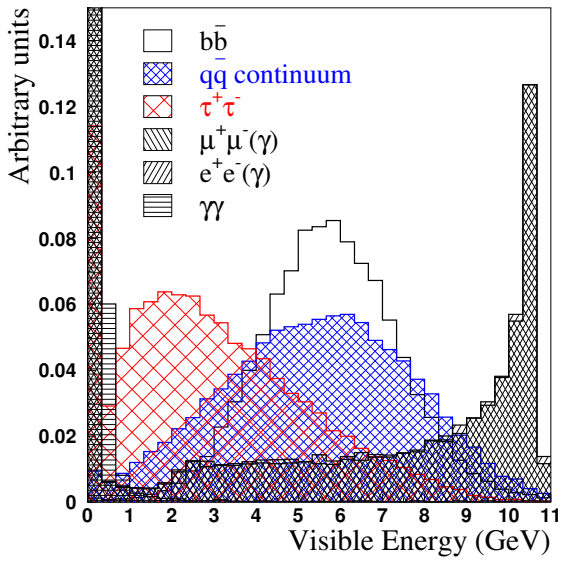

Figure 4.2: Distribution of the visible energy W in the main physics processes at the $\Upsilon(4S)$ energy. The distributions are normalized to the same area.

- Tracks are required to be within the polar angle acceptance of the detector: $0.410 < \theta_{lab} < 2.54$ rad. This ensures a well-understood tracking efficiency.

- A cut on the distance of closest approach to the beam spot in the $x-y$ plane ($|d_{xy}| < 1.5\,\mathrm{cm}$) and along the z axis ($|d_z| < 10\,\mathrm{cm}$) is applied. This reduces fake tracks and background tracks not originating from the vicinity of the interaction point.

- A cut on the maximum momentum of $p_{lab} < 10\,\mathrm{GeV}/c$, where p_{lab} is the laboratory momentum of the track is applied. This removes tracks not compatible with the beam energies.

- The kaon candidate track used for the reconstruction of the $D^0 \to K3\pi$ decay channel is also required to have a transverse momentum greater than 100 MeV and at least 12 hits detected in the Drift Chamber. This cuts are applied to reduce the combinatorial background.

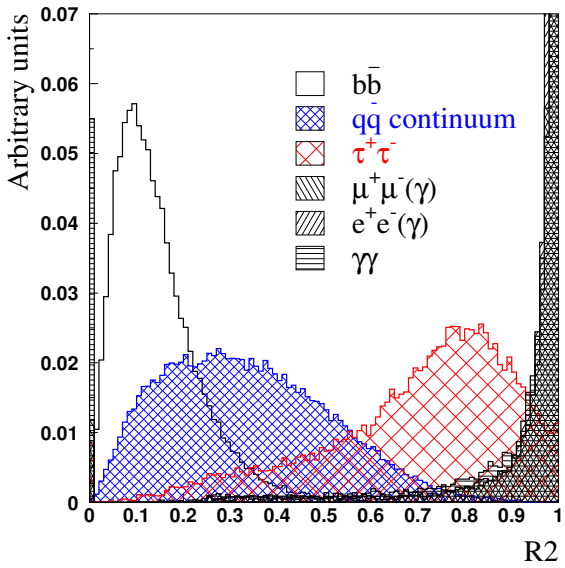

Figure 4.3: Distribution of R_2 for the main physics processes at the $\Upsilon(4S)$ energy. The distributions are normalized to the same area.

4.4 Particle identification

Kaons are distinguished from pions and protons on the basis of specific energy-loss measurements dE/dx in SVT and DCH, and the number of Cerenkov photons N_γ and the Cerenkov angle θ_c in the DIRC (sections 2.3,2.4).

The standard BABAR identification algorithm for kaons and pions is based on the likelihood ratio technique. The probability density functions for the discriminating variables dE/dx, N_γ and θ_c are measured from control samples and are used to compute likelihoods corresponding to the different particle hypotheses.
A purity category for the kaon hypothesis is defined by assigning a threshold value r for the ratio between the likelihoods corresponding to the kaon and pion hypotheses and selecting candidates that satisfy:

$$\mathcal{L}_K / \mathcal{L}_\pi > r.$$

Particle hypothesis likelihoods are obtained using the DIRC informations for candidates with momentum above the pion Cerenkov threshold and using the dE/dx measurements for lower momen-

Table 4.2: Summary of track selection criteria.

Select tracks with	Selection criteria
geometrical acceptance	$0.410 < \theta_{lab} < 2.54$ rad
distance in $x-y$ plane	$\lvert d_{xy}\rvert < 1.5\,\mathrm{cm}$
distance in z axis	$\lvert d_z\rvert < 10\,\mathrm{cm}$
maximum momentum	$p_{lab} < 10\,\mathrm{GeV}/c$
Additional cuts for kaons from $D^0 \to K3\pi$	
minimum transverse momentum	$pT_{lab} < 10\,\mathrm{GeV}/c$
N_{hits} in the Drift Chamber	$N_{hits} \geq 12$

tum candidates.

The difference between the measured truncated-mean dE/dx in the DCH, and the expected mean for the pion, kaon, and proton hypotheses, with typical resolution of 7.5%, is used to compute likelihoods $\mathcal{L}_\pi$, $\mathcal{L}_K$ and $\mathcal{L}_p$, assuming Gaussian distributions. The distribution of the measured dE/dx in the DCH for selected control samples, as a function of momentum, is shown in Figure 4.4.

The difference between the measured 60% truncated-mean dE/dx in the SVT and the expected dE/dx is described by an asymmetric Gaussian distribution. For minimum-ionizing particles, the resolution on the SVT truncated mean is about 14% which allows a 2σ separation between pions and kaons up to momentum of 500 MeV/c, and between kaons and protons beyond 1 GeV/c.

The DIRC provides π/K separation of 4σ or greater, for all tracks from B-meson decays, with momenta from the pion Cerenkov threshold, up to 4.2 GeV/c. In the DIRC, a likelihood is obtained for each particle hypothesis from the product of two components: the expected number N of Cerenkov photons, with a Poisson distribution, and the difference between the measured average Cerenkov angle θ_c (Figure 4.5) and the expected angle θ_c^0, for a given mass hypothesis, assuming a Gaussian distribution.

For this analysis the likelihood ratio threshold required for the kaon candidates used in the $D^0 \to K\pi$ ($K\pi\pi\pi$) decay reconstruction ensures a selection efficiency greater than 90% and a

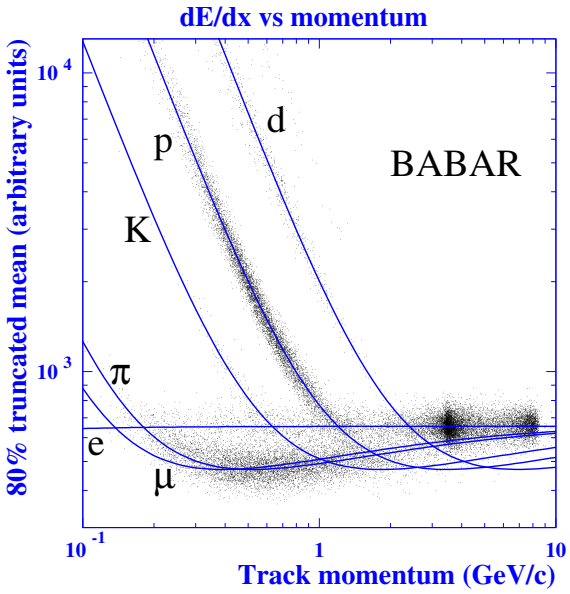

Figure 4.4: *Measurement of dE/dx in the DCH as a function of track momenta. The data include large samples of beam background triggers, evident from the high rate of protons. The curves show the Bethe-Bloch predictions derived from selected control samples of particles of different masses.*

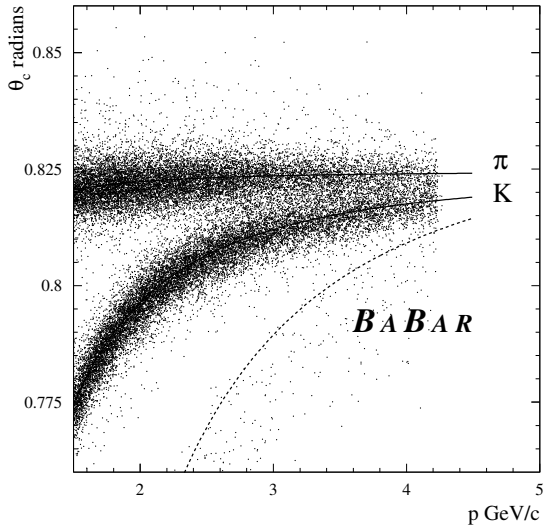

Figure 4.5: *Distribution of the measured Cerenkov angle θ_c in a control sample of $D^0 \to K\pi$ decays*

pion misidentification probability less than 15%.
The three pion candidates used to build the a_1 meson are required to fail (kaon veto) the selection criteria adopted to define a highly pure (misidentification probability less than 5%) kaon sample.

4.5 Charmed Mesons reconstruction

4.5.1 D^0 meson reconstruction

The decay modes $D^0 \to K\pi$ and $D^0 \to K3\pi$ are used to reconstruct the D^0 mesons. The branching ratios for these two channels are respectively $3.80 \pm 0.09\%$ and $7.46 \pm 0.31\%$ [13].
Charged tracks, selected as described in section 2.3, are combined to form the D^0 candidate. Kaons candidates are required to satisfy the identification criteria described in the previous section and a mass hypothesis is assigned to them accordingly.
The D^0 candidate is required to have a mass in a 3σ window of its nominal value (1.86 GeV/c^2). The mass distribution for the selected D^0 candidates is shown in figure 4.6.

4.5.2 D^* meson reconstruction

The D^* meson is reconstructed via the decay channel $D^{*+} \to D^0\pi^+$ which has a branching ratio of $67.7 \pm 0.5\%$[13]. The D^0 candidate, selected as described in the previous section, is associated with a pion candidate, taking into account the right correlation between the pion charge and the D^0 flavor.
Since the small mass difference between the D^* and the D^0 mesons, the phase space available for the pion is small and it is emitted with low momentum in the D^* reference frame. For this reason the pion emitted from the D^* decay is commonly called $soft\ pion$. Soft pions candidates selected in this analysis are requested to have momentum lower than $450 MeV/c^2$.
The mass difference δm = m(D^0- π) - m(D^0) between the D^0-π invariant mass and the D^0 mass is used to select D^* candidates. The resolution on δm is improved by constraining the D^0 candidate mass to its nominal value, and by using the beam-spot as an additional geometric constraint for the

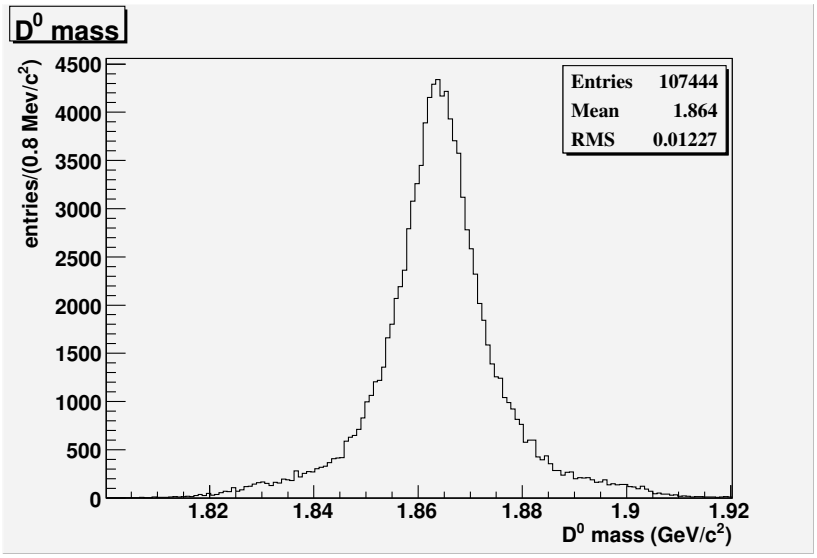

Figure 4.6: Distribution of the reconstructed D^0 mass in events that pass the pre-selection cuts described in 4.2 and the requirements on $|cos\theta_{thrust}|$ and P(χ^2) described in section 4.6.

soft pion, when the D^* decay vertex is computed (see Figure 4.8).
The distribution of δm for selected candidates is shown in Figure 4.7. The D^0-π candidates with a mass difference δm within 2.5 standard deviations $\sigma_{\delta m}$ of the expected value δm_0 = 145.4 MeV/c2 are selected.

4.6 B Meson selection

The D^{*+} candidates are combined with three charged tracks to reconstruct the $B \to D^{*+}\pi^+\ \pi^-\ \pi^-$ decay.
In order to reject background, different cuts are applied on discriminating quantities described in the next sub-sections. The first quantity, the trhust angle, is a topological variable wich suppress background from continuum events, like the normalized Fox-Wolfram momenta described in section 4.2. The probability of the kinematic fit to all the final state candidates is used to reject the background arising from random combinations of the tracks used to compose the B meson. The *energy substituted mass* ($m_{\rm ES}$) and the *energy difference* (ΔE) variables use the kinematic

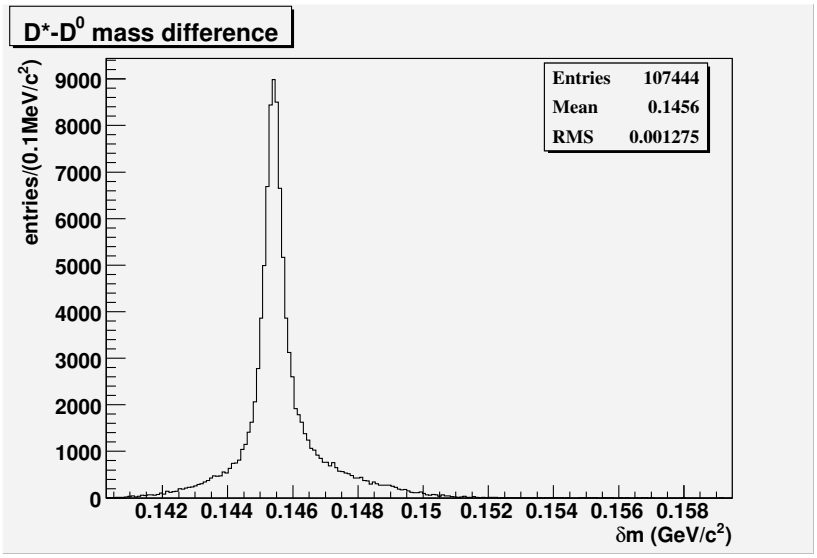

Figure 4.7: Distribution of the mass difference $\delta m = m(\overline{D}^0\pi^-) - m(\overline{D}^0)$ for D^{*-} candidates in events that pass the pre-selection cuts described in 4.2 and the requirements on $|cos\theta_{thrust}|$ and P(χ^2) described in section 4.6.

constraints from the initial state to finally select the B candidates.

4.6.1 Discriminating variables

- **Thrust angle**

  The thrust axis [59] of a set of particles is defined to be the direction which maximizes the sum of the longitudinal momenta of the particles. The thrust angle θ_{thrust} is the angle between the thrust axis of the B candidate and the thrust axis of the rest of the event. As explained in section 4.2, continuum background events tend to have a jet-like shape. Fake B candidates reconstructed in continuum events are built with particle that come from one of the two jets. Thus the decay axis of the B candidate is roughly collinear with the thrust axis for the rest of the event and the variable $|cos\theta_{thrust}|$ is peaked at one.
  For signal events, the B decay axis is uncorrelated with the thrust axis of the rest of the event (which in that case comes from the decay of the other B meson) resulting in a flat distribution for $|cos\theta_{thrust}|$. Figure 4.9 shows the distribution of $|cos\theta_{thrust}|$ for signal and

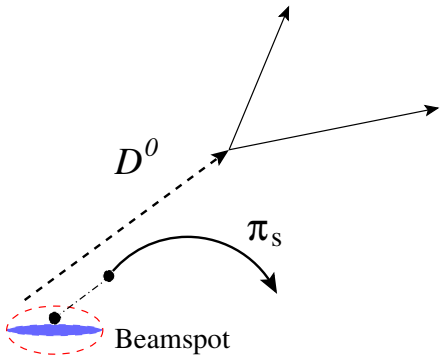

Figure 4.8: The blown up beam-spot (dashed ellipse) is used as an additional constraint on the trajectory of the soft pion π_s.

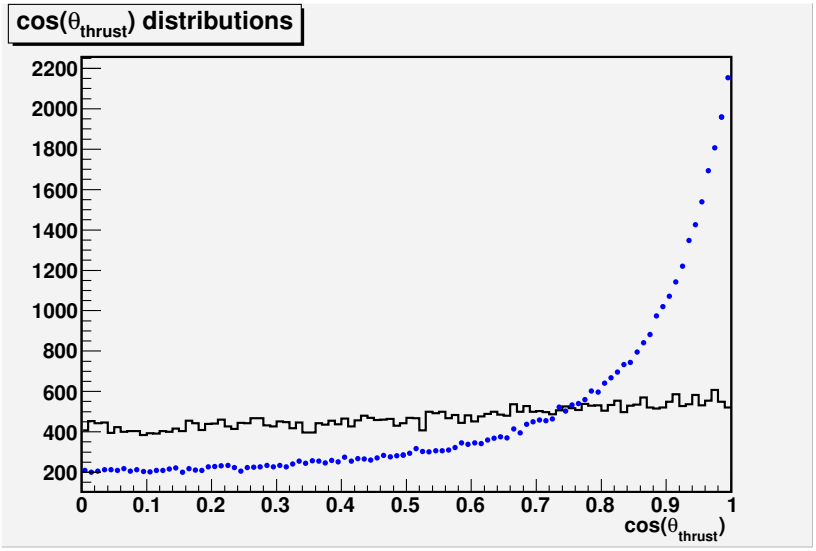

Figure 4.9: Comparison between the $|cos\theta_{thrust}|$ distributions for signal events form Monte Carlo simulation (continuum histogram) and background from data sideband (blue dots).

background events.

B candidates selected for this analysis are requested to satisfy the condition $|cos\theta_{thrust}| < 0.9$.

- **Probability of the kinematic fit**

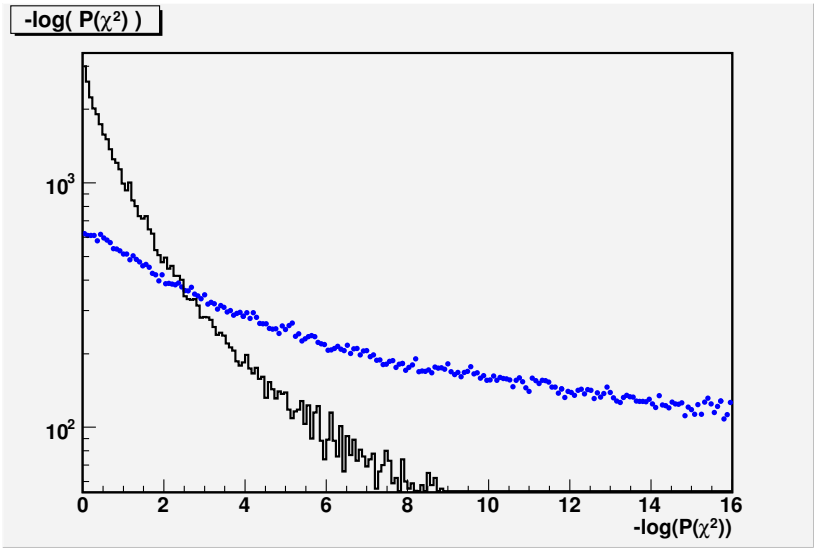

Figure 4.10: Comparison between the $-log(P(\chi^2))$ distributions for signal events form Monte Carlo simulation (continuum histogram) and background from data sideband (blue dots).

A kinematic fit on all the tracks used to reconstruct the B meson is performed. Particles momenta are re-calculated in the fit. A better resolution on the momenta is obtained by imposing some geometric and mass constraints. The D^{*+} candidate and the three pions tracks are requested to come from a common decay vertex taking into account the flightlenght of the B meson. The D^0 decay daughters invariant mass is constrained to nominal D^0 mass and the D^0-π_{soft} invariant mass is fixed to D^* mass. The χ^2 Probability of the kinematic fit is used to reject combinatorial background. For this analysis, only candidates with a χ^2 probability P(χ^2) greater than 0.01% are selected. Figure 4.10 shows the χ^2 probabilty distrubution for the kinematic fit for signal and background events.
Further details on the kinematic and vertex fit tecniques can be found here [60].

- **Energy difference**

After the cuts on the quantities described above, the final B candidate selection is performed using a pair of nearly uncorrelated kinematic variables which exploit the kinematic constraint from the $\Upsilon(4S)$ decay into a $B\bar{B}$ pair [61].

The first variable, ΔE, can be expressed in Lorentz invariant form as:

$$\Delta E = (2q_B q_0 - s)/2\sqrt{s}, \tag{4.1}$$

where $\sqrt{s}$=$2E^*_{beam}$ is the total energy of the e^+e^- system in the center of mass frame, and q_B and q_0 are the Lorentz vectors representing the quadri-momenta of the B candidate and of the e^+e^- system, $q_0 = q_{e^+} + q_{e^-}$. In the center of mass frame, ΔE takes the form:

$$\Delta E = E^*_B - E^*_{beam}, \tag{4.2}$$

where E^*_B is the reconstructed energy of the B meson. In this frame ΔE 's physical meaning becomes clear: it is the difference between the reconstructed and the expected B energy. The expected value of ΔE is thus zero. The RMS spread $\sigma(\Delta E)$ is given by the uncertainty σ_E on the measured energy and by the spread σ_B of the true B meson energy

$$\sigma^2(\Delta E) = \sigma^2_B + \sigma^2_E \, . \tag{4.3}$$

The uncertainty σ_E in the $B \to D^{*+}\pi^+ \, \pi^- \, \pi^-$ channel is found to be about 20 MeV. The measured spread in the beam energies result in variations of the $\Upsilon(4S)$ energy and are the main contribution to σ_B. The beam-energy spread is of the order of a few MeV (see Section 2.2) and therefore $\sigma(\Delta E)$ is dominated by σ_E. Figure 4.11 shows the ΔE distribution for events that satisfy all the selection criteria described above.

- **Energy substituted mass**

The beam-energy–substituted mass m_{ES} is defined as

$$m_{\mathrm{ES}} = \sqrt{E^{*2}_b - p^{*2}} \tag{4.4}$$

where E^*_b is again the beam energy and p^* is the measured momentum of the B candidate in the $\Upsilon(4S)$ center-of-mass frame, derived from the momenta of its decay products. m_{ES} is the B mass computed substituting the B meson energy by E^*_{beam}. The RMS spread of m_{ES} is given by [61]

$$\sigma^2(m_{\mathrm{ES}}) \approx \sigma^2_B + \left(\frac{p}{M_B}\right)^2 \sigma^2_p \tag{4.5}$$

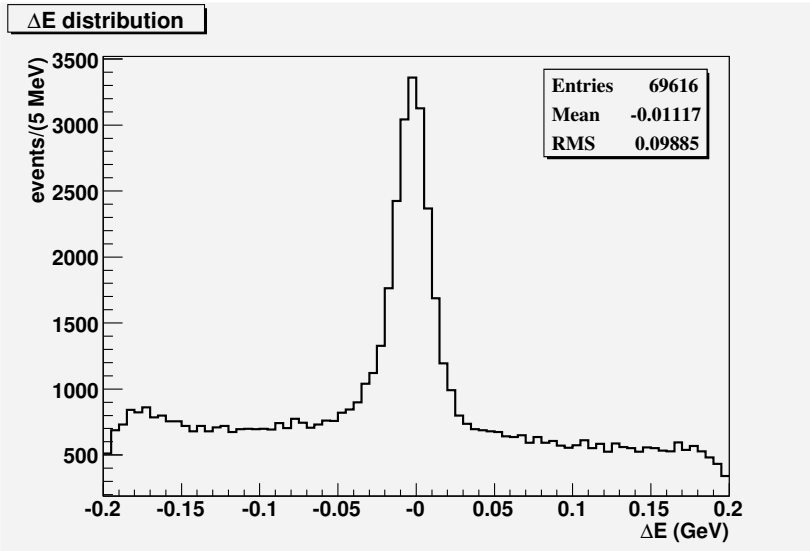

Figure 4.11: Distribution of the reconstructed energy difference ΔE for events selected in the $m_{\rm ES}$ peak region.

where σ_p is the uncertainty on the measured momentum. Unlike $\sigma(\Delta E)$, since $p/M_B \approx [325\,\mathrm{MeV}/c]/[5279\,\mathrm{MeV}/c^2] \approx 0.06c$, the uncertainty $\sigma(m_{\rm ES})$ is dominated by the beam-energy spread σ_B.

Although $m_{\rm ES}$ and ΔE are both evaluated from the beam energy E_b^*, the main sources of their experimental smearing are different (beams energy for $m_{\rm ES}$ and detector momentum resolution for ΔE). As a consequence these two variables are nearly uncorrelated. The $m_{\rm ES}$ distribution for selected $B \to D^{*+}\pi^+\,\pi^-\,\pi^-$ candidates is shown in figure 4.12.

4.6.2 Signal and background samples

Figure 4.13 shows the distribution of $m_{\rm ES}$ versus ΔE for the decay mode $B \to D^{*+}\pi^+\,\pi^-\,\pi^-$. Signal candidates accumulate around $m_{\rm ES} = m_B\,\mathrm{GeV}/c^2$ and $\Delta E = 0\,\mathrm{MeV}$.

The signal region is defined in the ($m_{\rm ES}$, ΔE) plane by:

$$5.27 < m_{\rm ES} < 5.29 GeV/c^2 \text{ and } |\Delta E^*| < 0.05,$$

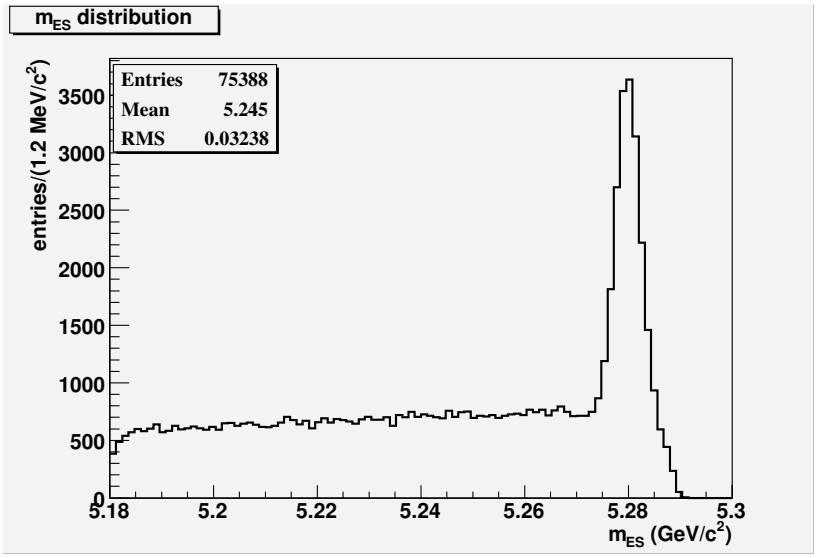

Figure 4.12: Distribution of the reconstructed beam energy substituted mass $m_{\rm ES}$ for events selected in the ΔE peak region.

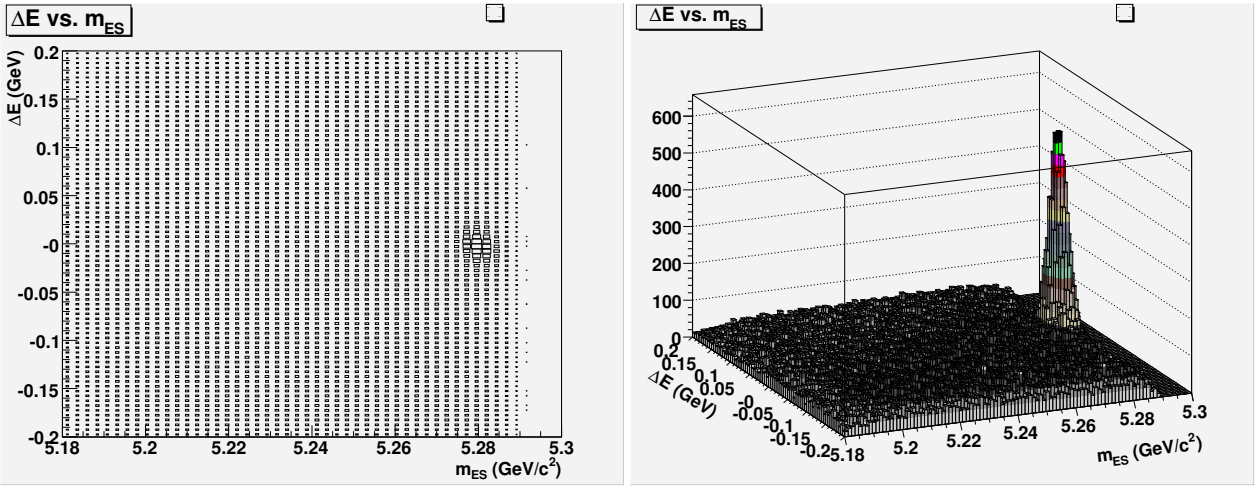

Figure 4.13: Distribution of ΔE vs. $m_{\rm ES}$ for selected $B \to D^{*+}\pi^+\,\pi^-\,\pi^-$ candidates. Left bidimensional view; Right tridimensional view.

For the purpose of determining event yields and purities and in order to study the backgorunds properties, four regions are defined in the ($m_{\rm ES}$, ΔE) plane. These regions are listed in Table 4.3.
The selection cuts described in this chapter, were applied to a sample of 209 fb^{-1} of data taken at the $\Upsilon(4S)$ resonance, resulting in 23204 events in the signal box.

Table 4.3: Definitions of subsamples of the selcted events used in the analysis.

Region	Selection criteria
Signal region	$5.27 < m_{\rm ES} < 5.29$ GeV/c^2 $\lvert\Delta E\rvert < 0.05$ GeV
$m_{\rm ES}$ Sideband	$5.2 < m_{\rm ES} < 5.26$ GeV/c^2 $\lvert\Delta E\rvert < 0.05$ GeV
Grand Sideband	$5.2 < m_{\rm ES} < 5.26$ GeV/c^2 $\lvert\Delta E\rvert < 0.15$ GeV
Fit Sample	$5.2 < m_{\rm ES} < 5.29$ GeV/c^2 $\lvert\Delta E\rvert < 0.15$ GeV

In order to estimate the contributions of signal and background to the signal box a fit to the $m_{\rm ES}$ distribution (including $m_{\rm ES}$ sideband events) was performed.

The combinatorial background arises from random combinations of charged particles that pass all the selection cuts. For these events the $m_{\rm ES}$ variable is smoothly distributed and does not peak near the B mass. This is parameterized with a threshold function

$$\mathcal{A}(m_{\rm ES}; m_0, \xi) = N_B\, m_{\rm ES} \sqrt{1-(m_{\rm ES}/m_0)^2}\, {\rm e}^{\xi\left(1-(m_{\rm ES}/m_0)^2\right)}, \tag{4.6}$$

commonly called the ARGUS function [62], where m_0 is the upper kinematic limit fixed at the beam energy E_b, N_B is the normalization factor, and ξ controls the slope of the function. The effect of variations in ξ is illustrated in Figure 4.14.

The $m_{\rm ES}$ distribution for signal events peak at the B mass. This distribution can be parameterized by a double gaussian.

The signal yield and the sample purity are determined from a fit to the $m_{\rm ES}$ distributions of the $N_{\rm tot}$ candidates contained in the signal and $m_{\rm ES}$-sideband regions, with a sum of a Double Gaussian $\mathcal{G}$ for the signal and an ARGUS function $\mathcal{A}$ for the background

$$f(m_{\rm ES}) = N_{sig}\ \mathcal{G}(m_{\rm ES}) + (N_{\rm tot} - N_{sig}\ )\,\mathcal{A}(m_{\rm ES})\ . \tag{4.7}$$

The purity $\mathcal{P}$ of the selected sample is defined as

$$\mathcal{P} = \frac{\int_{5.27}^{E_b} dm_{\rm ES}\, \mathcal{G}(m_{\rm ES})}{\int_{5.27}^{E_b} dm_{\rm ES}\, (\mathcal{G}(m_{\rm ES}) + \mathcal{A}(m_{\rm ES}))}\ . \tag{4.8}$$

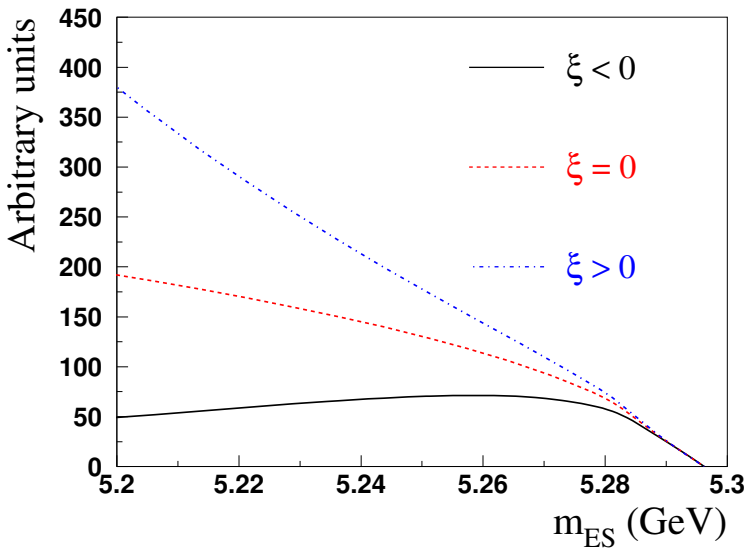

Figure 4.14: The shape of the ARGUS function for $\xi > 0$, $\xi = 0$, and $\xi < 0$.

Figure 4.15 shows the results of the $m_{\rm ES}$ fit on the full sample of selected events. We obtatains 16500$\pm$120 peaking events with a purity of 71%

Background contamination depends on the three pions system invariant mass $M_{3\pi}$, this is shown in figures 4.16 and 4.17 where are reported the $m_{\rm ES}$ fit results for the $0.5 < M_{3\pi} < 1.5\,{\rm GeV}$ and $1.5 < M_{3\pi} < 2.5\,{\rm GeV}$ intervals.

4.6.3 Three pions mass spectrum

As described in section 3.6, in order to study the properties of the 3 pions system the sample of events is divided in several sub-samples each charachterized by a range of values for the 3 pions invariant mass $M_{3\pi}$. In each bin a Dalitz plot analysis allows to separate the $J^P = 1^+$ contribution from other possible J^P states.

The 3 pions mass spectrum is shown in figure 4.18 The red histogram represents the $M_{3\pi}$ distribution for combinatorial background events. The shape for this distribution is taken from the $m_{\rm ES}$ sideband control sample while the normalization is obtained by integrating the fitted argus function on the signal region.

In addition to the broad structure around 1.2 GeV/c^2 mainly due to the a_1 meson a very narrow

peak is evident at $\sim$1.970 GeV/c^2. It correspond to the D_s^+ resonace decaying into 3 pions. In other words, the peak corresponds to the $B \to D^{*-} D_s^+$ decay with $D_s^+ \to \pi^-\pi^+\pi^+$. Since this charmed resonance is very narrow, we have choose to apply a veto in the D_s^+ region and we don't use events in the 1.8-2.0 GeV/c^2 for our spin parity analysis. With this choice of the veto region, we also reject $B \to D^{*-} D_s^+$, $D_s^+ \to K^-K^+\pi^+$ events, where two Kaons are wrongly identified as pions, resulting in a total invariant mass lower than the nominal mass of the D_s^+ ($M_{D_s} = 1968.6 \pm 0.6$ MeV[13]). Monte Carlo simulation have shown that these events are almost completely rejected with this veto.

The choice of the intervals in which we divide the $M_{3\pi}$ spectrum for our spin parity analysis is the result of a compromise between two opposite needs. On one side we would have bins as much as possible small to describe precisely the a_1 lineshape, but we have to ensure sufficient statistics to perform the Dalitz plot analysis in each bin.

The final choice is to use 17 not-uniform bins:

$$\begin{array}{llllll} 0.8-0.9, & 0.9-0.95, & 0.95-1.0, & 1.0-1.05, & 1.05-1.1, & 1.1-1.15, \\ 1.15-1.2, & 1.2-1.25, & 1.25-1.3, & 1.3-1.35, & 1.35-1.4, & 1.4-1.45, \\ 1.45-1.5, & 1.5-1.6, & 1.6-1.7, & 1.7-1.8, & 2.0-2.2, & \text{GeV}/c^2. \end{array} \tag{4.9}$$

The low statistcs and high backgruond contamination prevent us to have stable results for the Dalitz plot analysis above 2.2 GeV.

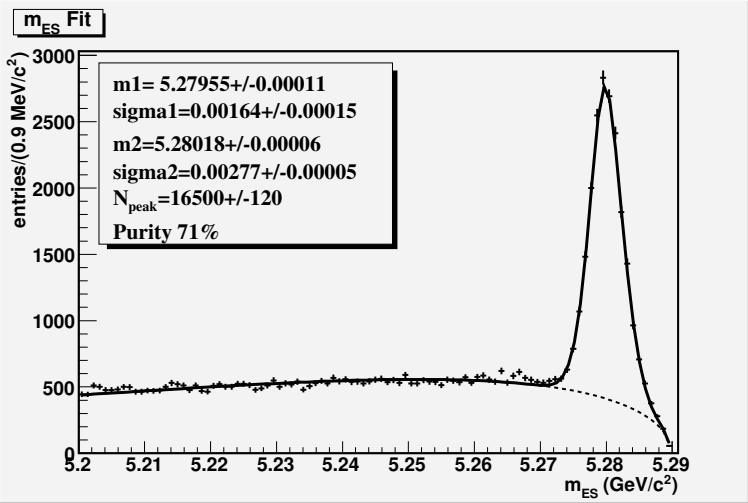

Figure 4.15: Fit to the $m_{\rm ES}$ distribution for the full sample of selected events. The combinatorial background is modeled with an argus function (dashed line) while signal si modeled by a double Gaussian.

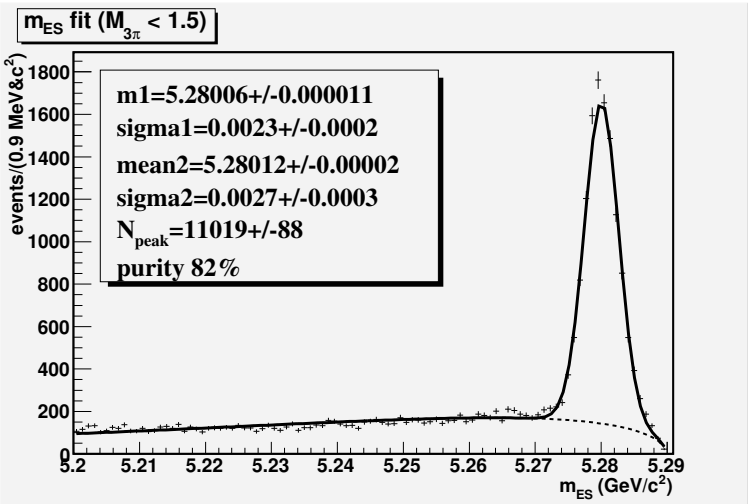

Figure 4.16: Fit to the $m_{\rm ES}$ distribution for the sample of selected events with $M_{3\pi} < 1.5$ GeV. The combinatorial background is modeled with an argus function (dashed line) while signal si modeled by a double Gaussian.

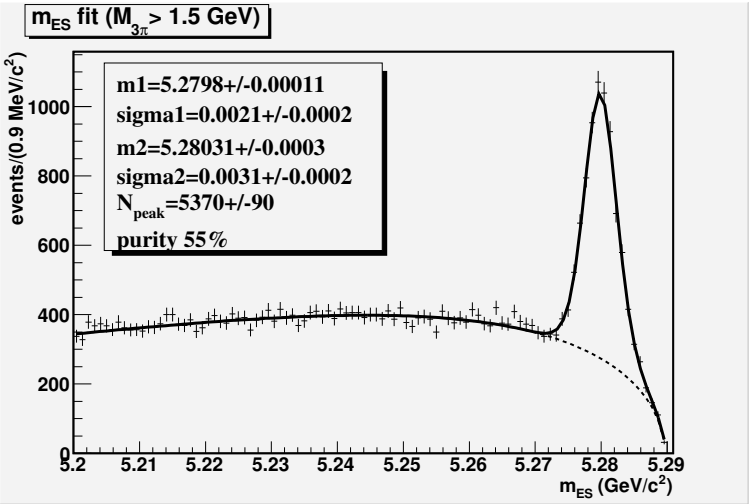

Figure 4.17: Fit to the $m_{\rm ES}$ distribution for the sample of selected events with $M_{3\pi} > 1.5$ GeV. The combinatorial background is modeled with an argus function (dashed line) while signal si modeled by a double Gaussian.

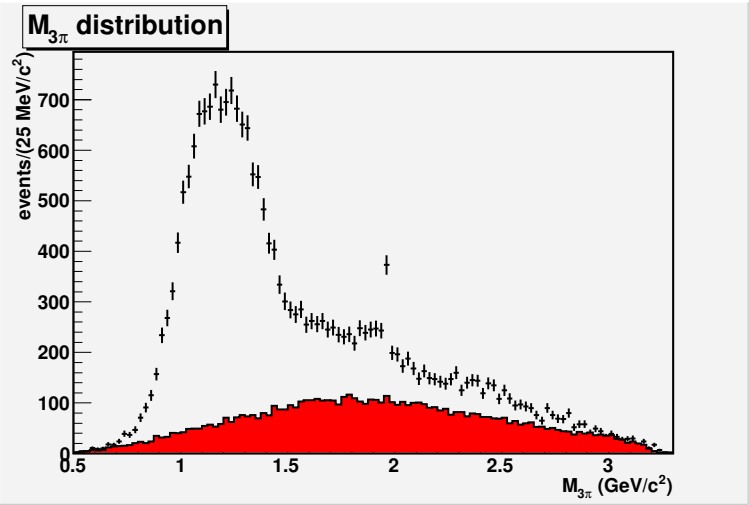

Figure 4.18: Distribution of the three pions system invariant mass for candidates selected in the signal region. The colored histogram shows the combinatorial background distribution obtained taking the shape from the $m_{\rm ES}$ sideband region and the normalization from the fit to $m_{\rm ES}$.

Chapter 5

Study of the $a_1(1260)$ meson

5.1 Introduction

In this chapter it is described the study of the three pions system produced in the $B \to D^{*-}\pi^+\,\pi^+\,\pi^-$ decays and the measure of the a_1 meson parameters.
In section 3.6 we have seen that the analysis of the Dalitz plot can be used to identify the different spin parity contributions to the the three pions.
In order to measure the a_1 line-shape, the three pions mass spectrum is divided in several bins and a Dalitz plot analysis is performed in each of them to extract the $J^P = 1^+$ yields, thus obtaining the a_1 mass distribution M_{a_1}.
We have used the Isobar model to describe each $J^P \to \pi\pi\pi$ decay. It is based on the assumption that the three body decay is dominated by a sequence of two body decays:

$$\begin{aligned} J^P \;\; &\to \;\; X\pi \\ &\quad\;\; X \to \pi\pi, \end{aligned} \tag{5.1}$$

where more intermediate resonances X can contribute to the total amplitude. In this framework, the Dalitz plot analysis allows to separate the a_1 meson from other possible resonances and to measure the contributions of the various intermediate resonances X contributing to the $a_1 \to \pi\pi\pi$ decay.
In order to obtain reliable results, it is important to correctly describe the combinatorial background, whose contribution to the signal sample increase in the high $M_{3\pi}$ region (4.6). Events selected in the $m_{ES} - \Delta E$ "Grand Sideband" control sample (defined in section 4.6) are used to

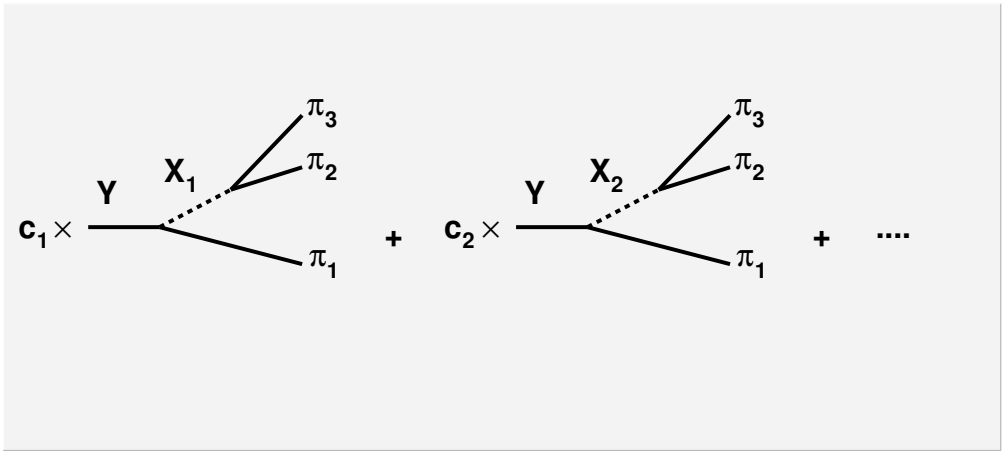

Figure 5.1: Three body decays in the Isobar Model. The decay amplitude is the sum of several amplitudes each characterized by a different intermediate resonance.

model the background Dalitz plot distribution.
Non uniformity in the phase space of the selection efficiency may affect the Dalitz plot and the extracted M_{a_1} distributions. These effects has been studied by measuring the selection efficiency in a Monte Carlo sample of signal events.
The Isobar model adopted in this analysis is described in detail in section 5.2. Section 5.3 contains the background characterization while the determination of the selection efficiencies is discussed in section 5.4. The results of the Isobar model fit in the various $M_{3\pi}$ bins are presented in section 5.5. The study of the $a_1 \to X\pi$ ($X \to \pi\pi$) substructures is presented in section 5.6, while the line-shape fit determining mass and width of the a_1 meson is shown in section 5.7. Section 5.8 contains the discussion on the main sources for the systematic uncertainty affecting the analysis that will be evaluated in the prosecution of the work.

5.2 The Isobar Model

We adopted the standard Isobar model [63] to describe the process $J^P \to \pi\pi\pi$ as a chain of two body decays.

Figure 5.1 shows the schematic diagram *'a la Feynman* used to build the total amplitude. It is obtained as a sum of amplitudes each describing a two body chain process with a different

propagating intermediate resonance:

$$\mathcal{A}(Y \to \pi\pi\pi) = \sum_k c_k A_{X_k} \tag{5.2}$$

where the c_k are phenomenological complex coefficients to be determined from the experiments. The two body chain amplitudes A_{X_k} are given by:

$$A_{X_k}(m_{12}^2, m_{13}^2|J, M, L) = R_k(m_{12})T_{JMjl}(p_1, p_2, p_3) + 2 \leftrightarrow 3, \tag{5.3}$$

where $R_k(m_{12})$ is the intermediate resonance mass term and T_{JMjl} provides the angular probability distribution depending on the spins of the initial state and of the intermediate resonance X_k and on the orbital angular momentum between X_k and the other pion. Since in this analysis we have two identical pions in the final state the amplitude is symmetrized for the exchange $2 \leftrightarrow 3$.

5.2.1 Mass term

The mass term R_k is given by a relativistic Breit Wigner describing the intermediate resonance propagation:

$$R_k(m_{12}) = \frac{(m_0^2 - m_{12}^2) + im_0\Gamma(m_{12})}{(m_0^2 - m_{12}^2)^2 + m_0^2\Gamma^2(m)}, \tag{5.4}$$

where the decay width of the resonance depends on the invariant mass of the two pions daughters:

$$\Gamma(m_{12}) = \Gamma_0(\frac{q}{q_0})^{2j+1}(\frac{m_0}{m_{12}})\frac{F_j^2(q)}{F_j^2(q_0)}. \tag{5.5}$$

The quantity q is the momentum of either daughter pion in the rest of frame of the intermediate resonance and is given by

$$q = \frac{1}{2}\sqrt{m_{12}^2 - 4m_\pi^2}. \tag{5.6}$$

The symbol q_0 denotes the value of q when $m_{12} = m_0$, the pole mass of the intermediate resonance. The functions $F_j(q)$ are the Blatt-Weisskopf barrier form factors [64]. These functions account of the fact that the maximum angular momentum L in a strong decay is limited by the linear momentum $\vec{q}$. Decay particles moving slowly with an impact parameter R (meson radius) of order 1 fm have difficulty generating sufficient angular momentum to conserve the spin of the

resonance. The explicit expressions for the Blatt-Weisskopf functions corresponding to j=1,2,3 are:

$$\begin{aligned} F_0 &= 1 \\ F_1 &= \sqrt{1/(1+z^2)} \\ F_2 &= \sqrt{1/(z^4+3z^2+9)}, \end{aligned} \tag{5.7}$$

where z = Rq, and R is the radius of the barrier, which is taken to be 1.5 GeV$^{-1} \simeq 0.3$ fm.

5.2.2 Angular distribution

The angular distribution function $T_{JMjl}(p_1, p_2, p_3)$ is evaluated from the three pions four momenta p_1, p_2, p_3 with the Zemach formalism approach [65]. The reaction of type 5.1, is characterized by four angular momentum quantum numbers: the spin J of the initial state and its component M along the quantization axis, the spin j of the intermediate resonance X and the orbital angular momentum l between X and the third pion:

$$J^P \rightarrow j^p + l. \tag{5.8}$$

Zemach has demonstrated the connection existing between the spin dynamics and the final state observables represented by the momenta of the three pions. This connection is given by the symmetric traceless Cartesian tensors formed by the particle four-momenta. A rank j tensor of this types has 2j+1 independent components, and represents an element of an irreducible subspace. In other words, it is isomorphous to a rank j spinor.

Recently Filippini, Fontana and Rotondi [66] have developed a covariant formulation of the Zemach formalism in which the spin tensors are represented in the Minkowski space as symmetric traceless tensor orthogonal to the particle four-velocity.

For a spin 1 particle decaying in two pions with momenta p_1 and p_2 the covariant Zemach tensor is given by:

$$S_\mu = q_\mu - (q \cdot u)u_\mu, \tag{5.9}$$

where $q^\mu = p_1^\mu - p_2^\mu$ is the break-up four momentum, while $u^\mu = (p_1^\mu + p_2^\mu)/2m_{12}$ is the four-velocity of the particle. The spin-2 tensor is instead given by:

$$T_{\mu\nu} = S_\mu S_\nu - \frac{1}{3}S^2(g_{\mu\nu} - u_\mu u_\nu). \tag{5.10}$$

To obtain the angular distribution function $T_{JMjl}(p_1, p_2, p_3)$, the Zemach prescription consists in the following steps:

- Build the Zemach tensors S and L representing the final state angular momenta j and l
- Combine these tensors to obtain a j+l rank tensor $S \times L$
- Contract this tensor with the spin $|JM\rangle$ Lorentz invariant wave function in the j+l dimensional space $e^{(J)}_{\mu_1 \ldots \mu_{j+l}}(M)$.

For a spin 1 particle of momentum p the three wave functions corresponding to $M = \pm 1, 0$ are given by [55]:

$$e^{\mu}(\mp 1) = \frac{\pm 1}{\sqrt{2}} \begin{pmatrix} p_x \pm i p_y \\ m + p_x(p_x \mp i p_y)/(E+m) \\ \mp i m + p_y(p_x \mp i p_y)/(E+m) \\ p_z(p_x \mp i p_y)/(E+m) \end{pmatrix}, \tag{5.11}$$

$$e^{\mu}(0) = \frac{1}{m} \begin{pmatrix} p_z \\ p_z p_x/(E+m) \\ p_z p_y/(E+m) \\ m + p_z^2(E+m) \end{pmatrix}. \tag{5.12}$$

The general spin functions can be obtained from the spin 1 wave functions using the Clebsh-Gordan series. For example the three rank-2 functions $|JM\rangle$ with $J = 0, 1, 2$ are given by:

$$e^{(J)}_{\mu\nu}(M) = \sum_{M=m_1+m_2} \langle 1 m_1; 1 m_2 | JM \rangle e_{\mu}(m_1) e_{\nu}(m_2). \tag{5.13}$$

With the prescriptions above it is possible to write the angular distribution functions for all the possible combinations of initial and final spin states. Since the 3 pions system is described by the two independent Dalitz variables the distribution functions turn out to depend only on these variables.

Figure 5.2 shows the simulated Dalitz plot distributions for the decay processes $1^+ \to \rho\pi$ (l =0,2), $0^- \to \rho\pi$ (l = 1), $2^+ \to \rho\pi$ (l = 1) with a total invariant mass $M = 1.7$ GeV.

5.2.3 Selection rules

Since we deal with strong decays, the amplitudes appearing in equation 5.2 have to be chosen taking into account parity conservation as well as angular momentum conservation. The following

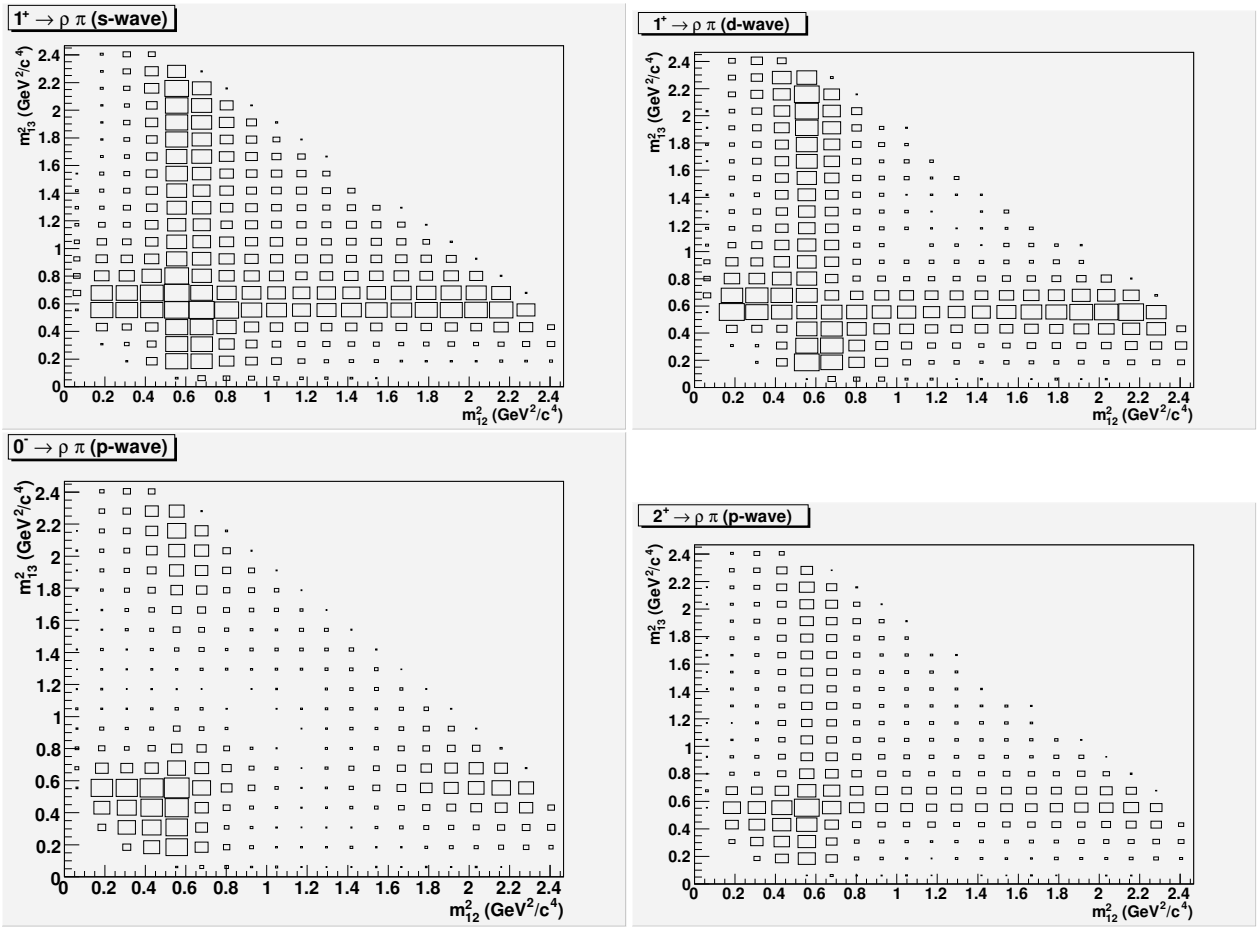

Figure 5.2: Comparison between Dalitz plots for the $J^P \rightarrow \rho\pi$ decay for different initial states spins and orbital angular momenta.

selection rules hold:

$$\begin{aligned} &|j-l| <= J <= j+l, \\ &p = (-1)^j, \\ &P = (-1)^{j+l+1}, \end{aligned} \tag{5.14}$$

In our analysis we neglected contributions of spin and orbital angular momenta greater than 2. From the selection rules above follows that the a_1 meson ($J^P = 1^+$) decays via scalar mesons intermediate resonances (σ, $f_0(980)$, $f_0(1370)$,...) only in p-wave while for the pseudo-vector mediated decays (ρ,ρ') both s-wave and d-wave may contribute. It is also possible a spin 2 intermediate resonance ($f_2(1270)$) in a p-wave state.

Table 5.1 resumes the allowed amplitudes for other possible J^P states.

$J^P \rightarrow$	$j^p + l$	intermediate resonance	orbital angular momentum state
$0^- \rightarrow$	$0^+ + 0$	$\sigma\pi$, $f_0(980)\pi$, $f_0(1370)\pi$	S-wave
	$1^- + 1$	$\rho\pi$, $\rho'\pi$	P-wave
	$2^+ + 2$	$f_2\pi$	D-wave
$1^+ \rightarrow$	$0^+ + 1$	$\sigma\pi$, $f_0(980)\pi$, $f_0(1370)\pi$	P-wave
	$1^- + 0$	$\rho\pi$, $\rho'\pi$	S-wave
	$1^- + 2$	$\rho\pi$, $\rho'\pi$	D-wave
	$2^+ + 1$	$f_2\pi$	P-wave
$2^- \rightarrow$	$0^+ + 2$	$\sigma\pi$, $f_0(980)\pi$, $f_0(1370)\pi$	D-wave
	$1^- + 1$	$\rho\pi$, $\rho'\pi$	P-wave
	$2^+ + 0$	$f_2\pi$	S-wave
	$2^+ + 2$	$f_2\pi$	D-wave
$2^+ \rightarrow$	$1^- + 2$	$\rho\pi$, $\rho'\pi$	D-wave
	$2^+ + 1$	$f_2\pi$	P-wave

Table 5.1: Allowed amplitudes for the different $J^P \rightarrow \pi^+\pi^+\pi^-$ processes.

5.3 Combinatorial Background model

In order to build the probability density functions modeling the background Dalitz distribution in the 18 bins of $M_{3\pi}$, we make use of the control sample of events from the "Grand Sideband" region defined in table 4.3.

The Probability density functions are built from the binned Dalitz distributions smoothed by means of a bilinear interpolation technique [67].

It should be noticed that we can not use the bidimensional histogram in the usual coordinates (m^2_{12} , m^2_{13}), since the Dalitz plot bounds in this coordinates depend on the total mass $M_{3\pi}$ (eq. 3.46), while the histogram we take from the control sample is integrated on a finite range of $M_{3\pi}$. The Pdf $f_{bkg}(M_{3\pi}, m^2_{12}\,, m^2_{13}\,)$ obtained from this histogram is normalized as:

$$\int_{M_1}^{M_2} dM_{3\pi} \int_{D.P.(M_2)} dm^2_{12}\, dm^2_{13}\, f_{bkg}(M_{3\pi}, m^2_{12}\,, m^2_{13}\,) = 1, \tag{5.15}$$

where M_1 and M_2 are the bounds of the $M_{3\pi}$ bin, and $D.P.(M_2)$ is surface in the (m^2_{12} , m^2_{13}) plane corresponding to $M_{3\pi} = M_2$.

The correct normalization we would obtain is instead:

$$\int_{M_1}^{M_2} dM_{3\pi} \int_{D.P.(M_{3\pi})} dm_{12}^2 \, dm_{13}^2 \, f_{bkg}(M_{3\pi}, m_{12}^2 \, , m_{13}^2 \,) = 1. \tag{5.16}$$

To build the correctly normalized Pdf, we use a co-ordinate transformation to a square Dalitz plot defined as [68]:

$$\begin{array}{rcl} (M_{3\pi}, m_{12}^2 \, , m_{13}^2 \,) & \rightarrow & (M'_{3\pi}, m', \theta') \\ M'_{3\pi} & = & M_{3\pi} \\ m' & = & \frac{1}{\pi} arccos(2\frac{m_{++}-m_{++}[min]}{m_{++}[max]-m_{++}[min]} - 1) \\ \theta' & = & \frac{1}{\pi}\theta_{++}, \end{array} \tag{5.17}$$

where m_{++} is the invariant mass between the two pions with the same charge, $m_{++}[max] = M_{3\pi} - m_\pi$ and $m_{++}[min] = 2m_\pi$ are its kinematical boundaries while θ_{++} is the helicity angle between one of the like-sign pions and the three pions system momentum in the $\pi^+\pi^+$ rest frame. The new variables (m', θ') range from 0 to 1 for each value of $M_{3\pi}$.

The correctly normalized Probability density functions are obtained from the experimental histograms in these coordinates by means of the Jacobian of the transformation defined as:

$$dm_{12}^2 \, dm_{13}^2 \, = |J| dm' d\theta'. \tag{5.18}$$

The determinant of the Jacobian $|J|$ is given by:

$$|J| = 4|p_+^*|^2 m_{++} \frac{\partial m_{++}}{\partial m'} \frac{\partial cos\theta_{++}}{\partial \theta'}, \tag{5.19}$$

where $|p_+^*|$ is the momentum of the like-sign pions in the rest frame of the $\pi^+\pi^+$ system and the partial derivative above are given by:

$$\begin{array}{rcl} \frac{\partial m_{++}}{\partial m'} & = & -\frac{\pi}{2} sin(\pi m')(m_{++}[max] - m_{++}[min]) \\ \frac{\partial cos\theta_{++}}{\partial \theta'} & = & -\pi sin(\pi\theta'). \end{array} \tag{5.20}$$

Figure 5.3 shows the usual and the square Dalitz plot experimental distributions for "Grand Sideband" events in the $[1.5, 1.6]$ $M_{3\pi}$ interval. The Jacobian determinant function is illustrated in figure 5.4.

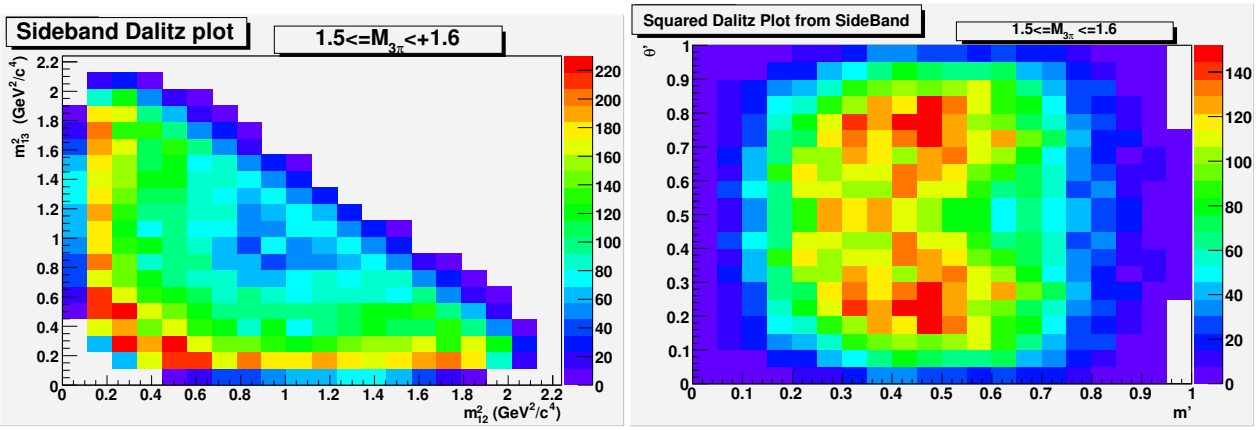

Figure 5.3: Dalitz plot distributions in the "usual" (left) and in the "square" coordinates for "Grand Sideband" events with $M_{3\pi}$ in the $[1.5, 1.6]$ interval.

5.4 Selection efficiency

In order to study the effects of the efficiency selection on the $M_{3\pi}$ and Dalt plot distributions, we make use of a sample of Monte Carlo simulated signal events. Our sample consist of about 60000 of reconstructed $B \rightarrow D^{*-}\pi^+\,\pi^+\,\pi^-$ events, which corresponds to approximately 4 times the number of signal events in the data. In order to cover almost uniformly the whole $M_{3\pi}$ spectrum, the MC sample used is a cocktail of $B \rightarrow D^{*-}a_1^+$ events with $M_{3\pi}$ mainly distributing in the [0.5 GeV,1.5 GeV] range and of non-resonant $B \rightarrow D^{*-}\rho\pi^-$ and $B \rightarrow D^{*-}\pi^+\,\pi^+\,\pi^-$ events mainly covering the $M_{3\pi} > 1.5GeV$ region.

In each bin i in which we divided the $M_{3\pi}$ spectrum for the spin-parity analysis, we evaluate the overall efficiency as the ratio $\epsilon_i = N_i^{Sel}/N_i^{Gen}$ where N_i^{Gen} and N_i^{Sel} are respectively the total number of generated events and the number of selected events in that bin. The distribution of the efficiency over the Dalitz plots is obtained by the ratio between the reconstructed and generated Dalitz plots. With the currently available Monte Carlo statistics we cannot perform a fine binning to estimate the Dalitz plot efficiency. We find that the Dalitz efficiency functions are consistent with a flat distribution within the statistical error. The efficiency distributions over the Dalitz plot for the [1.3, 1.35 GeV] and [1.6,1.7 GeV] $M_{3\pi}$ bins are shown in figure 5.5.

Figure 5.6 shows the measured overall efficiencies ϵ_i as a function of the total 3 pions mass $M_{3\pi}$. The decreasing trend is related with the D^* reconstruction. At increasing values of $M_{3\pi}$ correspond decreasing values of the D^* momentum and, as a consequence, lower values for the

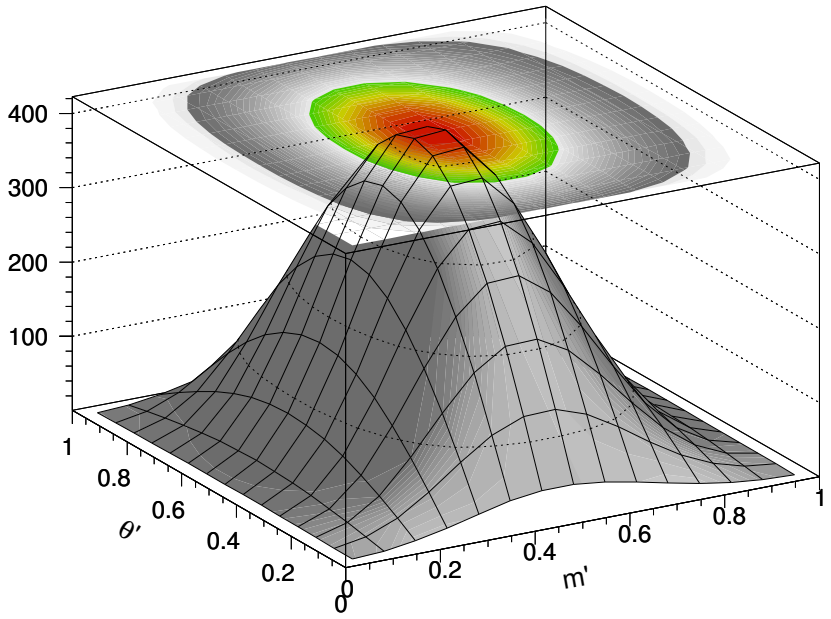

Figure 5.4: Jacobian determinant function for the (m_{12}^2 ,m_{13}^2)$\rightarrow$(m', θ') coordinate transformation.

transverse momentum of the *soft pion* (see section 4.5.2) from the $D^{*-} \rightarrow \bar{D}^0\pi^-$ decay. The soft pion is the slower particle in the event and its reconstruction efficiency drops for small transverse momenta (figure 2.9).

The measured ϵ_i of figure 5.6 are used to correct the number of a_1 events extracted from the spin-parity analysis in the various bin of $M_{3\pi}$ thus obtaining the a_1 mass distribution.

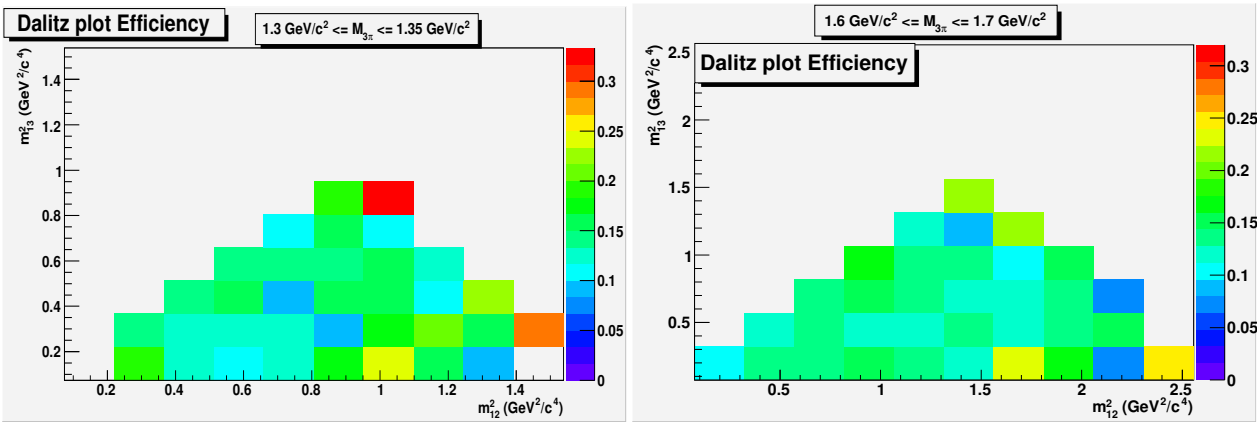

Figure 5.5: Selection efficiency in the symmetrized half-Dalitz plot for the [1.3, 1.35 GeV] (left) and [1.6,1.7 GeV] (right) $M_{3\pi}$ bins. The distributions are obtained in Monte Carlo events.

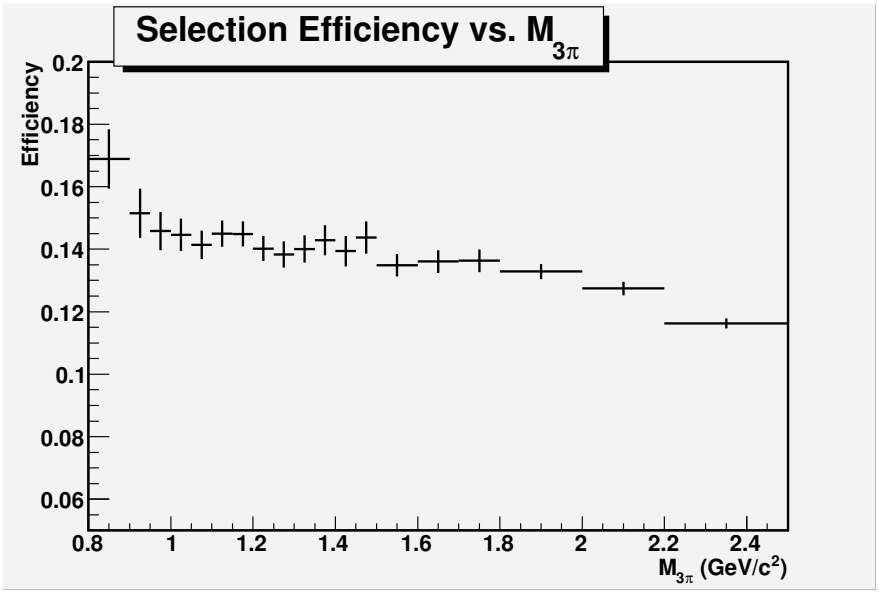

Figure 5.6: Selection efficiency as a function of the 3 pions system invariant mass $M_{3\pi}$ determined from Monte Carlo events.

5.5 Dalitz plot analysis

5.5.1 The likelihood function

The spin parity analysis we have performed in each of the 17 $M_{3\pi}$ bins defined in eq. 4.9 consists in an extended unbinned maximum likelihood fit to the m_{ES}, $M_{3\pi}$, m_{12}^2 , m_{13}^2 distribution. The likelihood function we use is defined as:

$$\mathcal{L} = \sum_{J^P} N_{J^P}\mathcal{P}_{J^P} + N_{bkg}\mathcal{P}_{bkg}, \tag{5.21}$$

where $\mathcal{P}_{J^P}$ and $\mathcal{P}_{bkg}$ are the product of the normalized Probability Density Functions (PDFs) for m_{ES}, $M_{3\pi}$, and the Dalitz variables:

$$\mathcal{P} = \mathcal{P}_{m_{\rm ES}} \times \mathcal{P}_{M_{3\pi}} \times \mathcal{P}_{D.P.(M_{3\pi})}. \tag{5.22}$$

The signal and background PDFs for the $m_{\rm ES}$ variable are described in section 4.6.2. We model the $m_{\rm ES}$ signal distribution with a double Gaussian while the background distribution is modeled by the Argus function (eq. 4.6).

In each of the 17 bins, the 3 pions mass distribution for signal and background events are well modeled by first order polynomials described by the slope parameters c_{sig} and c_{bkg}. We assume the same $\mathcal{P}_{m_{\rm ES}}$ and $\mathcal{P}_{M_{3\pi}}$ PDFs for the different spin parity states which are discriminated by means of the Dalitz plot PDF.

The Dalitz plot distribution for a given J^P state is obtained using the Isobar model described in section 5.2:

$$\mathcal{P}_{D.P.(M_{3\pi})} = \frac{|\sum_i c_i A_i(m_{12}^2\,, m_{13}^2\,)|^2}{\int\int_{D.P.(M_{3\pi})} |\sum_i c_i A_i(m_{12}^2\,, m_{13}^2\,)|^2} dm_{12}^2\, dm_{13}^2\,, \tag{5.23}$$

where the sum runs over the possible intermediate states contributing to the $J^P \to \pi\pi\pi$ decay and $c_i = |c_i|e^{i\phi_i}$ are the phenomenological complex coefficients weighing each intermediate states and have to be determined from the fit. Each amplitude A_i is given by the product of the mass and angular terms defined in sections 5.2.1 and 5.2.2. The list of the intermediate resonances used in the fit is given in table 5.1, the values for their Breit-Wigner pole masses and widths are taken from PDG [13].

To obtain normalized Pdfs we have to evaluate the integral appearing at the denominator of eq. 5.23. This term can be re-written as:

$$\int\int_{D.P.(M_{3\pi})} |\sum_i c_i A_i(m_{12}^2\,, m_{13}^2\,)|^2 dm_{12}^2\, dm_{13}^2 \;= \sum_{i,j} c_i c_j^* I_{ij}(M_{3\pi}), \tag{5.24}$$

where:

$$I_{ij}(M_{3\pi}) = \int\int_{D.P.(M_{3\pi})} A_i A_j^* dm_{12}^2 \, dm_{13}^2 \, . \tag{5.25}$$

The integral terms I_{ij} are evaluated by means of a toy-Monte Carlo technique by generating an high statistics sample of 3 pions systems with total invariant mass $M_{3\pi}$ and flat in the phase space. The algorithm used to generate this sample is GENBOD [69].
The model for the background Dalitz plot PDF is obtained from the experimental distribution of events in the "Grand Sideband" region and has been discussed in detail in section 5.3.

5.5.2 Goodness of fit

To compare the fit results with the data, we have developed a toy Monte Carlo to generate high statistics samples of events according with the fitted parameters. Starting from a sample of events uniformly distributed in the phase space, we apply the hit-or-miss technique to obtain the distribution described by our PDF.
A χ^2 comparison between the data and the toy MC Dalitz plots gives us an estimate of the goodness of the fit. However, as pointed out in [70], the use of evenly spaced bins may cause an unreliable value of the χ^2 due to the presence of low populated bins. For this reason we have implemented an adaptive binning algorithm to represent the Dalitz plot. The bins of the resulting histogram are partitioned according to the density of the data and are nearly equally populated.
The binning algorithm is described in detail in [71]. The starting point is a cell that contains all the data points in the (m_{12}^2 ,m_{13}^2) plane. The cell is splitted in two parts by a line passing for its centroid. Among the two possible cell-cut directions (vertical and horizontal), the algorithm choose the one that minimize the difference between the number of points contained in two resulting subcell. This criterion is applied iteratively to each sub-cell which is splitted as long as the number of events contained exceed a threshold value.
Once the partitioning is completed, at each cell is assigned a χ^2 value given by:

$$\chi^2_{cell} = \frac{(N^{data}_{cell} - N^{fit}_{cell})^2}{N^{data}}, \tag{5.26}$$

where N^{fit}_{cell} is estimated by means of the toy MC. The sum of the χ^2_{cell} quantities is the bidimensional χ^2 of our fit.

5.5.3 Fit strategy

The event sample given in input to the fit program is the "Fit Sample" defined in table 4.3.
In order to reduce the number of free parameters in the fit, the $m_{\rm ES}$ and $M_{3\pi}$ shape parameters are fixed from a previous unbinned maximum likelihood fit in which the Dalitz variables are not considered. The free parameters for the likelihood of eq. 5.21 are the N_{J^P}, N_{bkg} yields and the Isobar model parameters $|c_i^{J,P}|$ and $\phi_i^{J,P}$. Each J^P PDF is defined up to a not-observable complex constant. A convention choice can be done to fix one of the coefficients $c_i^{J,P}$ in 5.23 as:

$$\begin{aligned} |c_1| &= 1 \\ \phi_1 &= 0 \end{aligned} \tag{5.27}$$

The other complex coefficient fitted are so relative to the fixed one. The results on the observables yields N_{J^P}, N_{bkg} does not depend on the convention choice. Moreover, from the fitted c_i it is possible to define other physical quantities that does not depend on the convention choice and can be used for comparison between the experiments (section 5.6).
Since the available statistics is not enough to obtain stable results from a simultaneous fit of all the possible J^P states and intermediate resonance of table 5.1 we decided to perform, in each bin of $M_{3\pi}$, a set of independent fits each characterized by a choice of a reduced number of contributing amplitudes and to adopt the above defined χ^2 criterion to select the configuration that better describe the data.

5.5.4 Results

The results of the maximum likelihood fits in the 17 $M_{3\pi}$ bins are shown in figures 5.7-5.23 . For each bin we report:

- the $m_{\rm ES}$ and $M_{3\pi}$ distributions with the fit result superimposed.
- The symmetrized Dalitz plot distribution,
- The m_{+-} projection of the symmetrized Dalitz plot. It is compared with the fit expectation histogram generated by means of the toy Monte Carlo described in subsection 5.5.2. Different colors are used to identify the different J^P and background contributions.

- The distribution of the χ^2 on the adaptively binned Dalitz plot.
- A table summarizing the results of the fit.

Below 1.5 GeV/c^2, the data are well reproduced by the only $J^P = 1^+$ state, corresponding to the a_1 resonance. The intermediate resonances contributing to the the total amplitude are $(1^+ \to \rho\pi)_{s-wave}$, that gives the main contribution, $1^+ \to \sigma\pi$, $(1^+ \to \rho\pi)_{d-wave}$, and $1^+ \to \rho'\pi$. The peak of the ρ resonance is clearly visible in the m_{+-} distribution and in the Dalitz plot.
Above 1.5 GeV/c^2 also the $f_2(1270)$ peak is evident in the two opposite-sign pions mass spectrum but the $1^+ \to f_2\pi$ amplitude is not useful to well reproduce the data. The introduction of a $J^P = 2^-$ state is needed describe the data in the $M_{3\pi} > 1.5$ GeV intervals. We find significant contributions of the $2^- \to f_2\pi$, and $2^- \to \rho\pi$ amplitudes. The $J^P = 2^-$ state is found in a mass region that corresponds to the $\pi_2(1600)$ resonance. The presence of a spin 2 resonant contribution to the 3 pion system in $B \to D^{*-}\pi^+\,\pi^+\,\pi^-$ decay may indicate that non-factorizable terms are not negligible in this process, since the CKM favored diagram for a two body $B \to D^{*-}X^+$ decay is expected to be suppressed in QCD factorization [72] for a resonance X with spin higher than 1. We don't find significant contributions of any other J^P state to the mass spectrum.

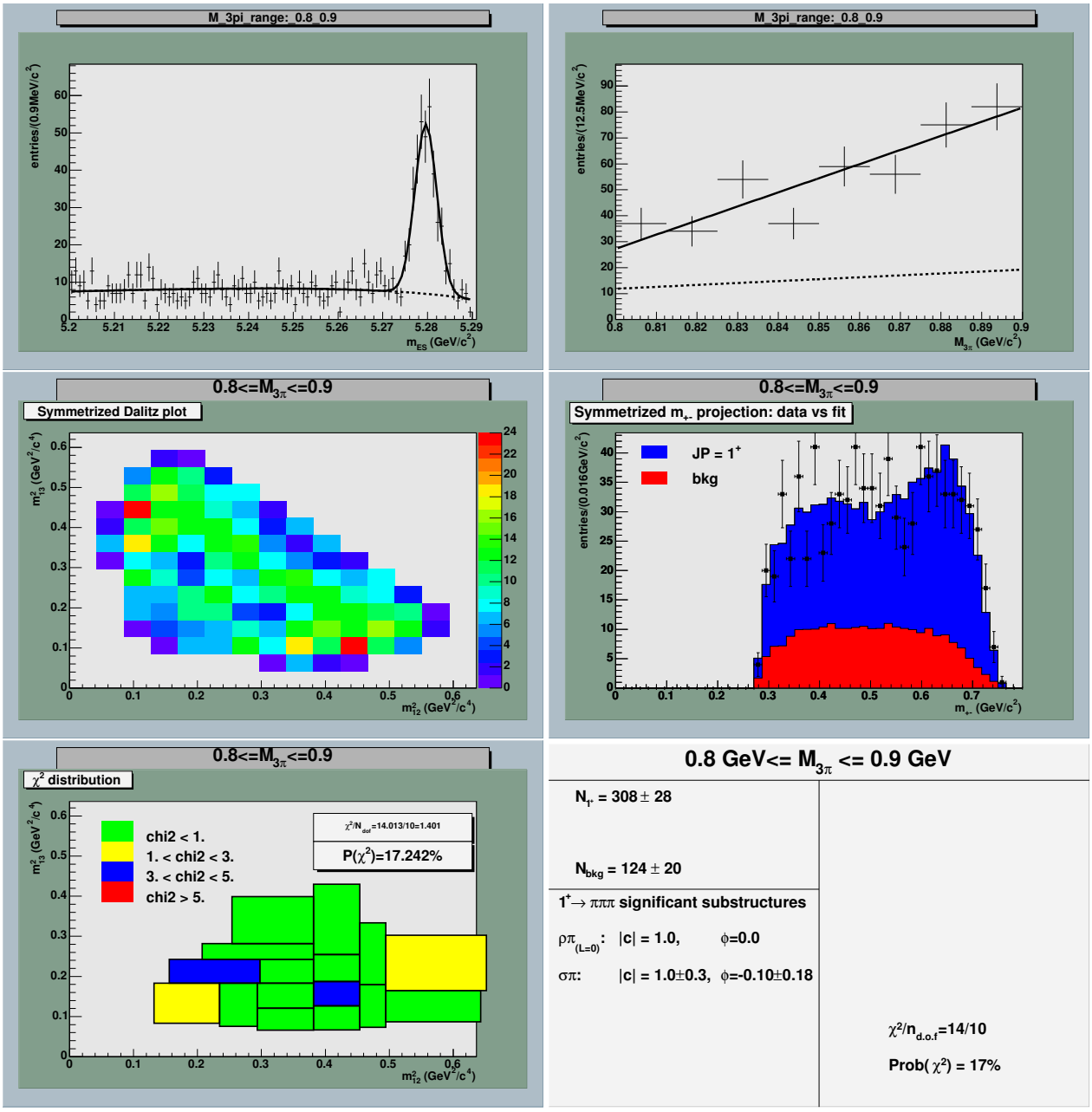

Figure 5.7: Results of the spin parity analysis in the [0.8 GeV, 0.9 GeV] $M_{3\pi}$ interval. Top-left: $m_{\rm ES}$ distribution (data vs. fit). Top-right: $M_{3\pi}$ distribution (data vs. fit). Middle-left: Symmetrized Dalitz plot distribution. Middle-right: Symmetrized m_{+-} distribution (2 entries per event) compared with the fit results (colored histograms). Bottom-left: χ^2 distribution on the half symmetrized Dalitz plot. Bottom-right: Summary table with the fitted coefficients (moduli and phases) for the intermediate states that significantly contribute to the total amplitude.

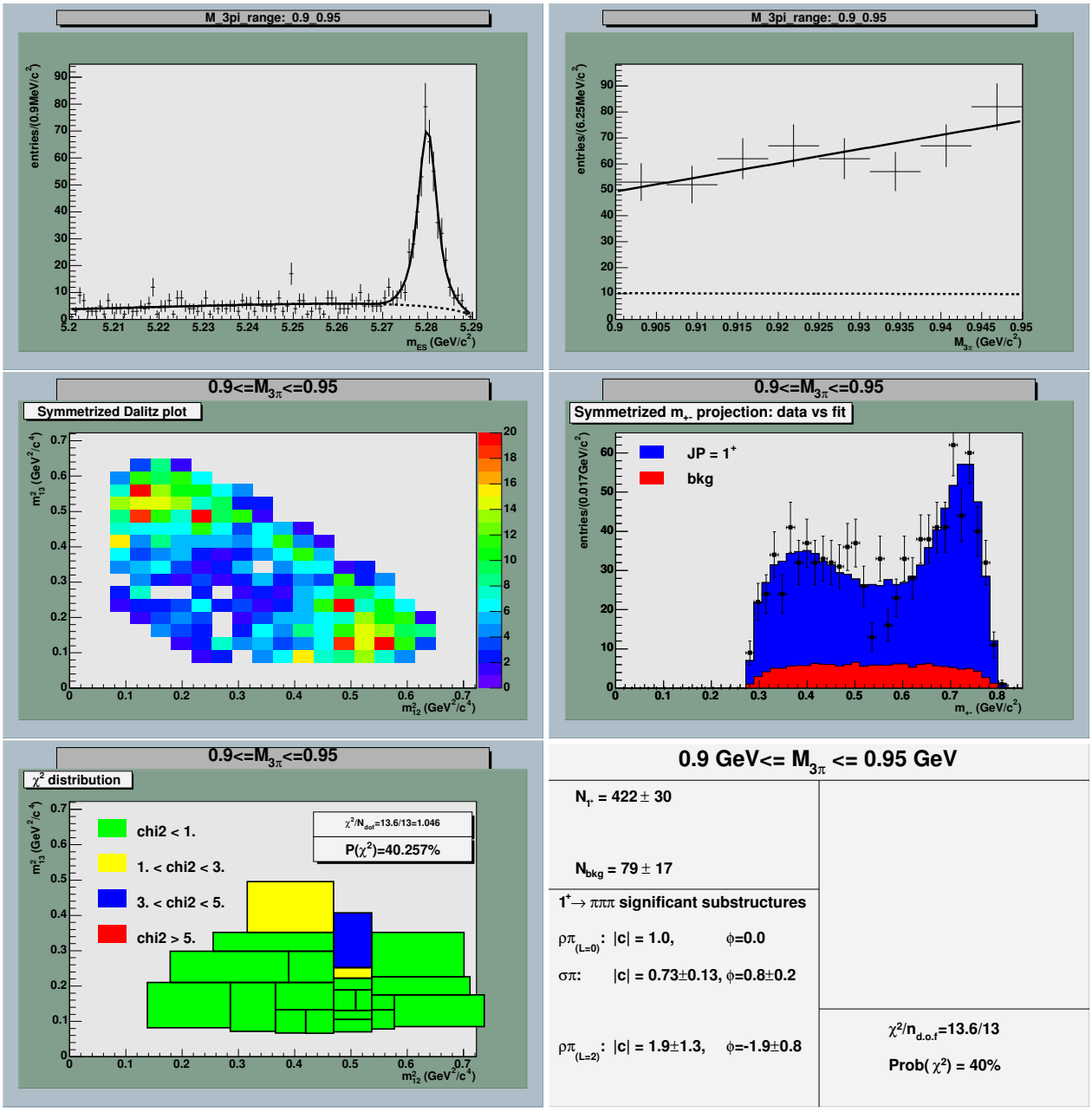

Figure 5.8: Results of the spin parity analysis in the [0.9 GeV, 0.95 GeV] $M_{3\pi}$ interval. Top-left: $m_{\rm ES}$ distribution (data vs. fit). Top-right: $M_{3\pi}$ distribution (data vs. fit). Middle-left: Symmetrized Dalitz plot distribution. Middle-right: Symmetrized m_{+-} distribution (2 entries per event) compared with the fit results (colored histograms). Bottom-left: χ^2 distribution on the half symmetrized Dalitz plot. Bottom-right: Summary table with the fitted coefficients (moduli and phases) for the intermediate states that significantly contribute to the total amplitude.

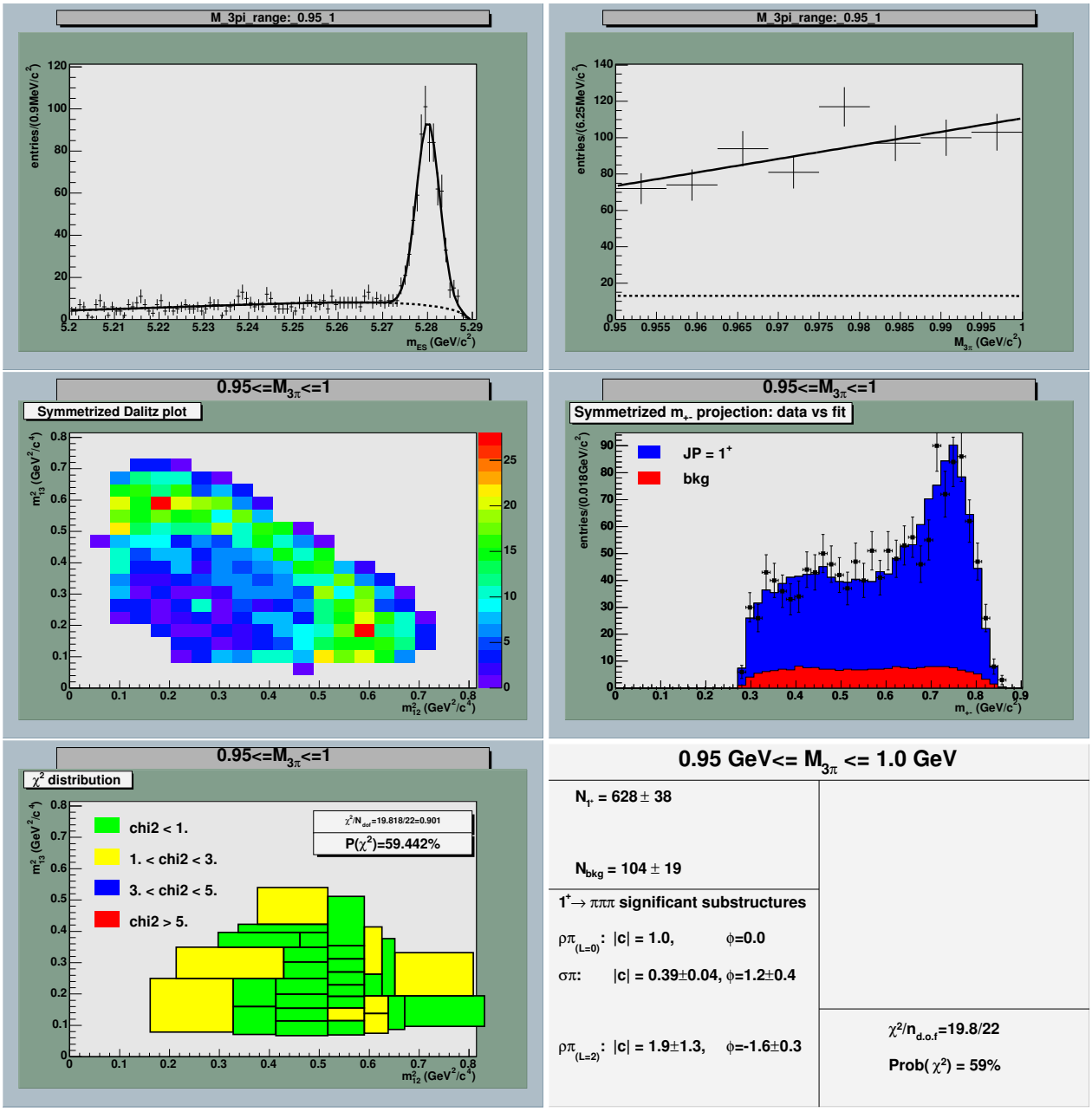

Figure 5.9: Results of the spin parity analysis in the [0.95 GeV, 1.0 GeV] $M_{3\pi}$ interval. Top-left: $m_{\rm ES}$ distribution (data vs. fit). Top-right: $M_{3\pi}$ distribution (data vs. fit). Middle-left: Symmetrized Dalitz plot distribution. Middle-right: Symmetrized m_{+-} distribution (2 entries per event) compared with the fit results (colored histograms). Bottom-left: χ^2 distribution on the half symmetrized Dalitz plot. Bottom-right: Summary table with the fitted coefficients (moduli and phases) for the intermediate states that significantly contribute to the total amplitude.

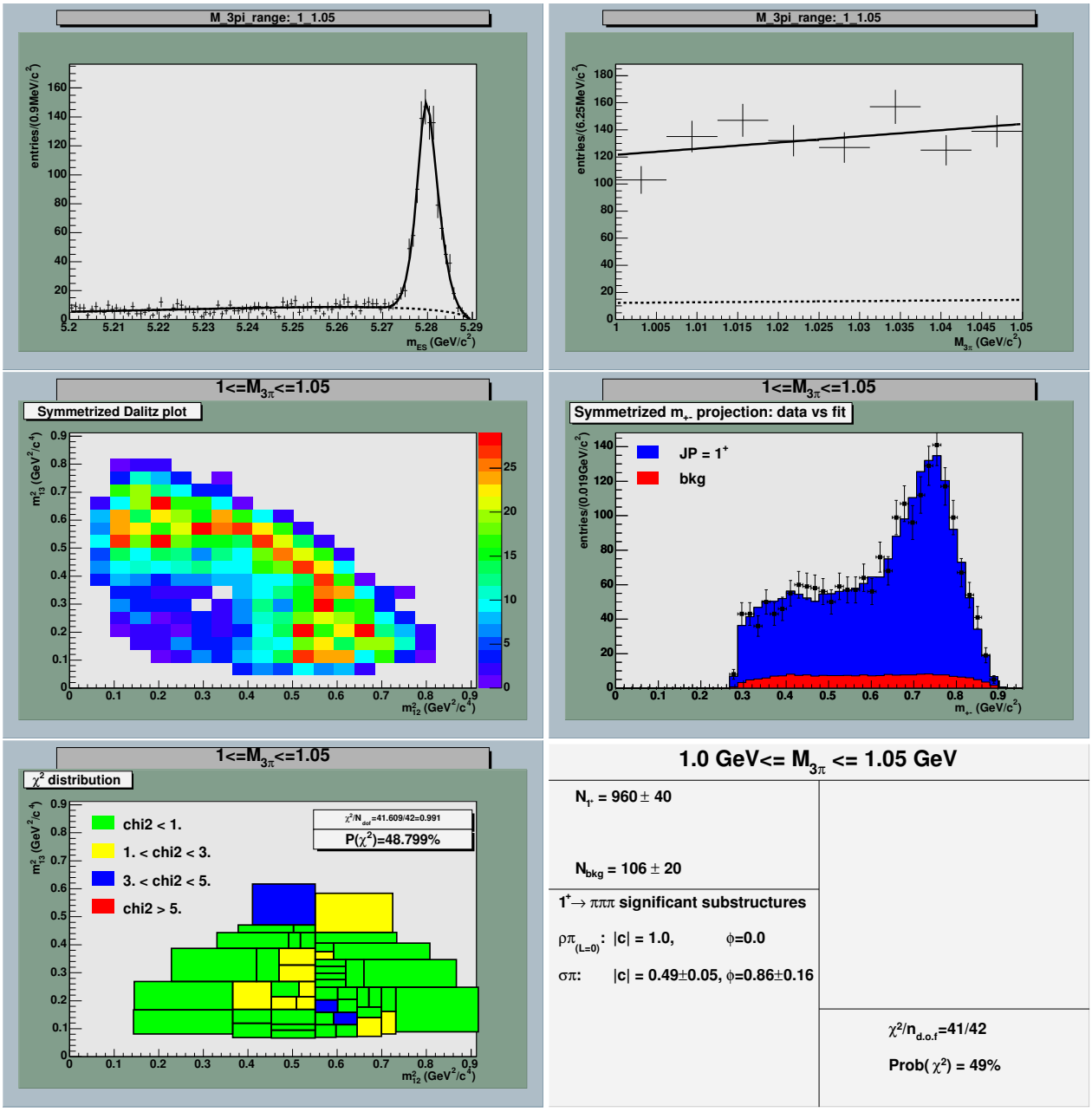

Figure 5.10: Results of the spin parity analysis in the [1.0 GeV, 1.05 GeV] $M_{3\pi}$ interval. Top-left: $m_{\rm ES}$ distribution (data vs. fit). Top-right: $M_{3\pi}$ distribution (data vs. fit). Middle-left: Symmetrized Dalitz plot distribution. Middle-right: Symmetrized m_{+-} distribution (2 entries per event) compared with the fit results (colored histograms). Bottom-left: χ^2 distribution on the half symmetrized Dalitz plot. Bottom-right: Summary table with the fitted coefficients (moduli and phases) for the intermediate states that significantly contribute to the total amplitude.

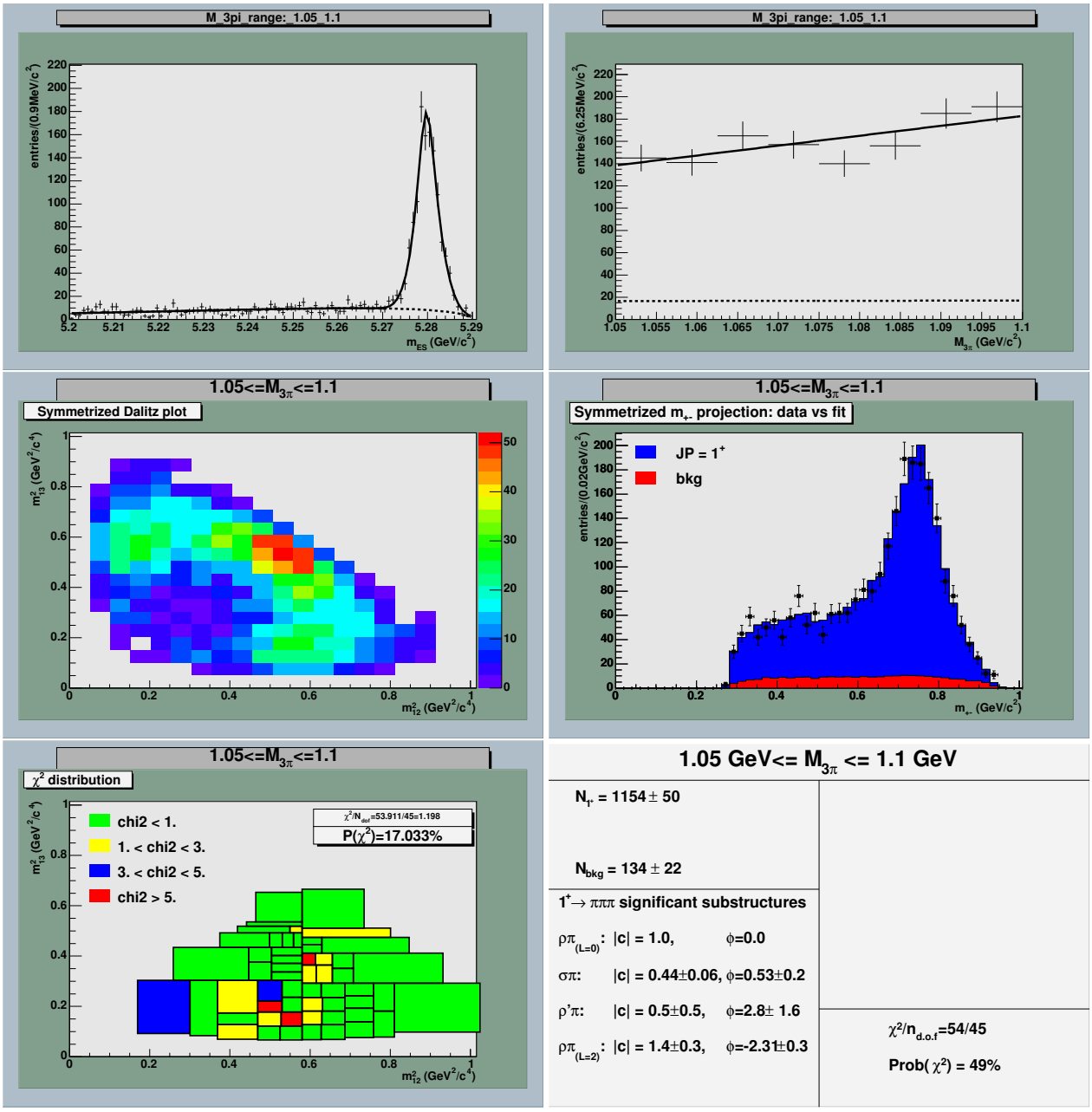

Figure 5.11: Results of the spin parity analysis in the [1.05 GeV, 1.1 GeV] $M_{3\pi}$ interval. Top-left: $m_{\rm ES}$ distribution (data vs. fit). Top-right: $M_{3\pi}$ distribution (data vs. fit). Middle-left: Symmetrized Dalitz plot distribution. Middle-right: Symmetrized m_{+-} distribution (2 entries per event) compared with the fit results (colored histograms). Bottom-left: χ^2 distribution on the half symmetrized Dalitz plot. Bottom-right: Summary table with the fitted coefficients (moduli and phases) for the intermediate states that significantly contribute to the total amplitude.

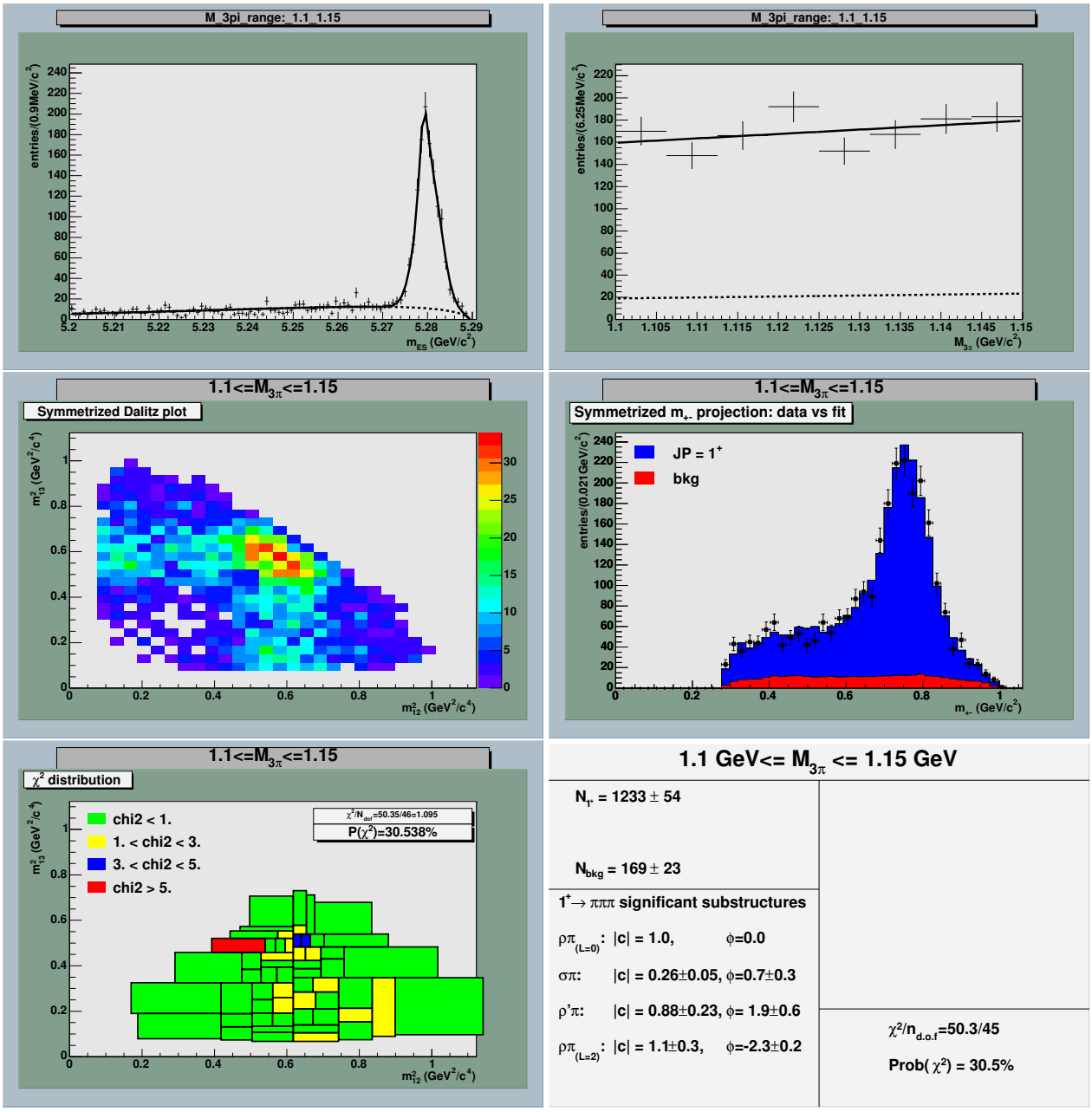

Figure 5.12: Results of the spin parity analysis in the [1.1 GeV, 1.15 GeV] $M_{3\pi}$ interval. Top-left: $m_{\rm ES}$ distribution (data vs. fit). Top-right: $M_{3\pi}$ distribution (data vs. fit). Middle-left: Symmetrized Dalitz plot distribution. Middle-right: Symmetrized m_{+-} distribution (2 entries per event) compared with the fit results (colored histograms). Bottom-left: χ^2 distribution on the half symmetrized Dalitz plot. Bottom-right: Summary table with the fitted coefficients (moduli and phases) for the intermediate states that significantly contribute to the total amplitude.

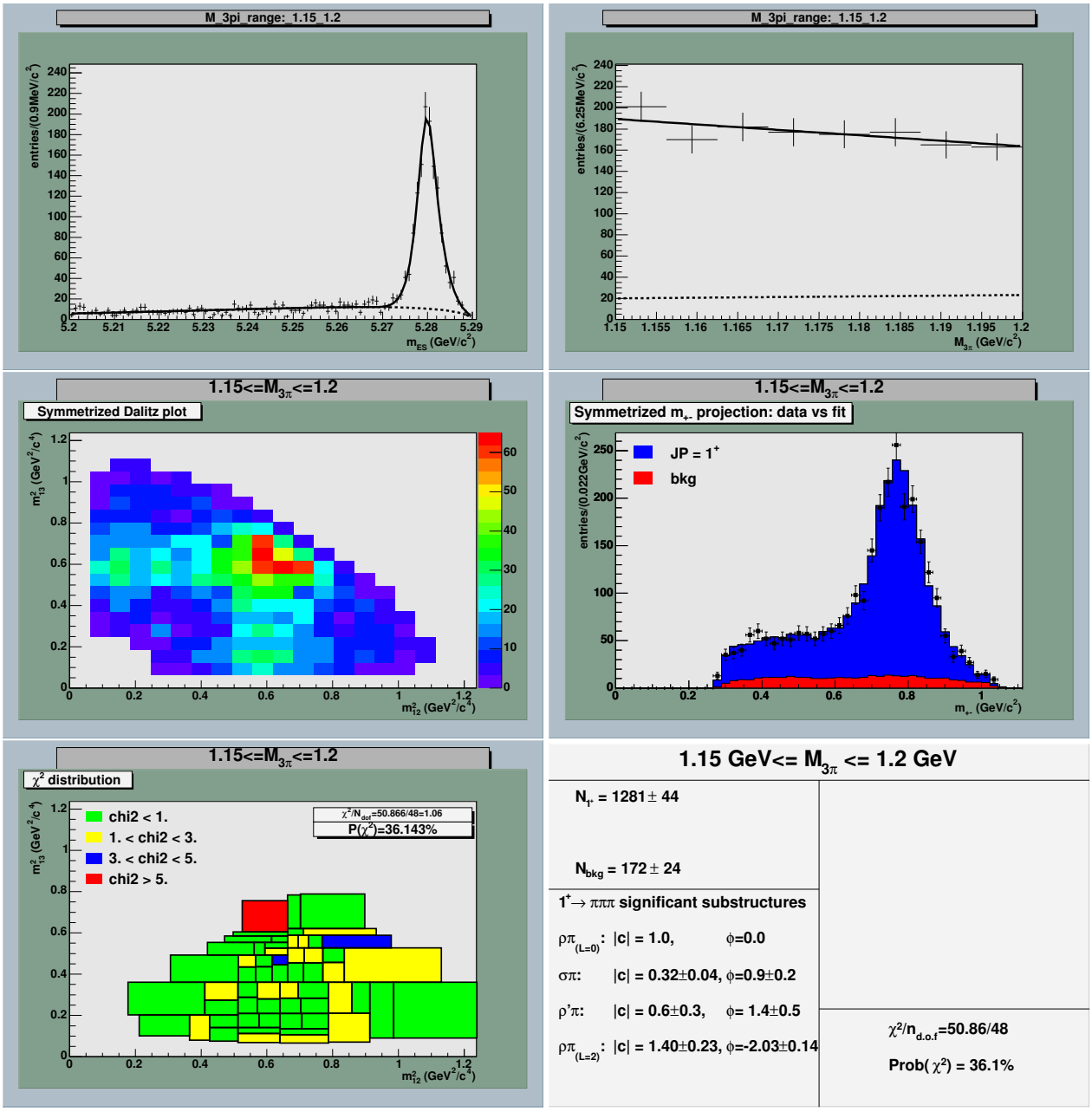

Figure 5.13: Results of the spin parity analysis in the [1.15 GeV, 1.2 GeV] $M_{3\pi}$ interval. Top-left: $m_{\rm ES}$ distribution (data vs. fit). Top-right: $M_{3\pi}$ distribution (data vs. fit). Middle-left: Symmetrized Dalitz plot distribution. Middle-right: Symmetrized m_{+-} distribution (2 entries per event) compared with the fit results (colored histograms). Bottom-left: χ^2 distribution on the half symmetrized Dalitz plot. Bottom-right: Summary table with the fitted coefficients (moduli and phases) for the intermediate states that significantly contribute to the total amplitude.

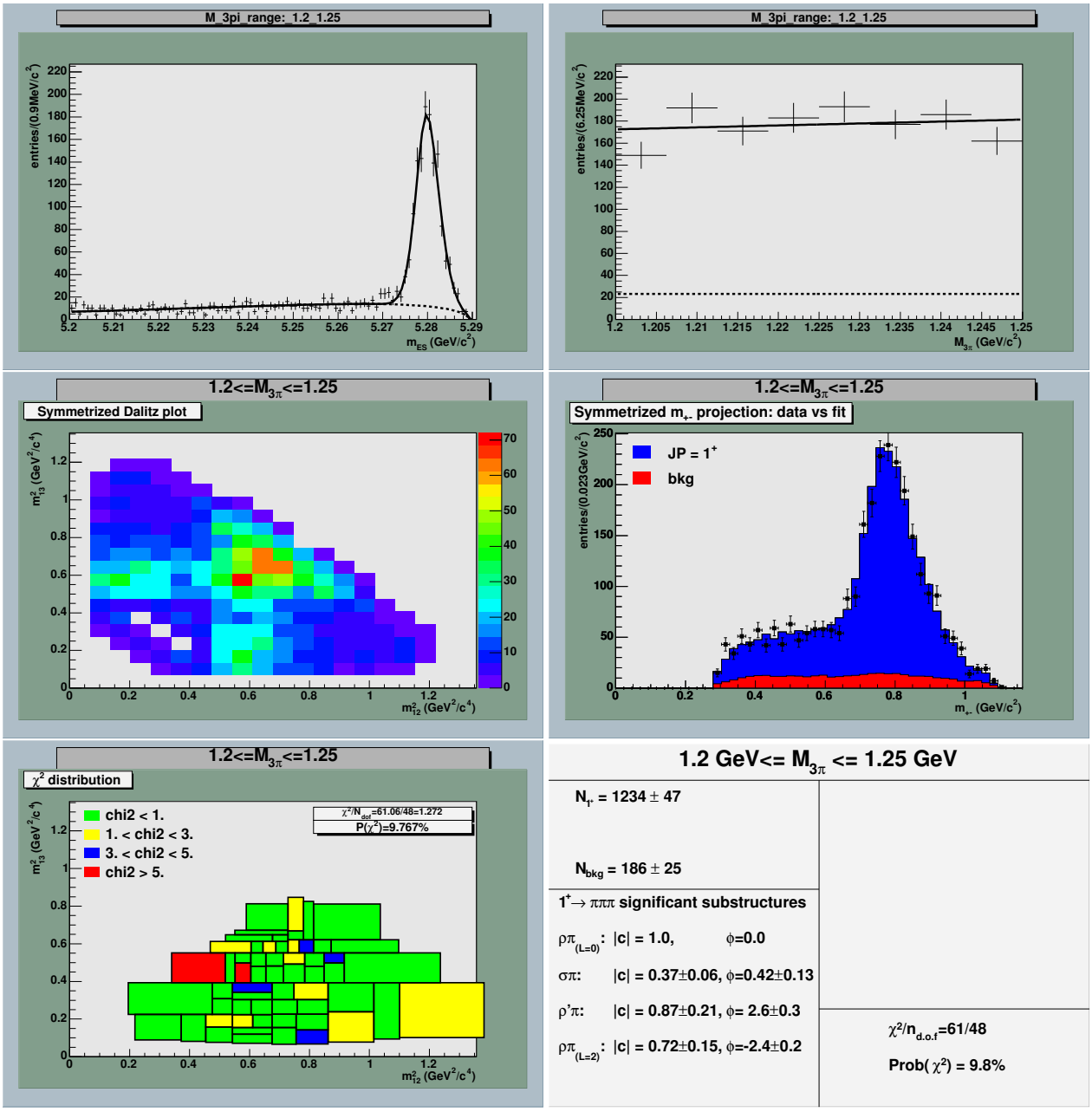

Figure 5.14: Results of the spin parity analysis in the [1.2 GeV, 1.25 GeV] $M_{3\pi}$ interval. Top-left: $m_{\rm ES}$ distribution (data vs. fit). Top-right: $M_{3\pi}$ distribution (data vs. fit). Middle-left: Symmetrized Dalitz plot distribution. Middle-right: Symmetrized m_{+-} distribution (2 entries per event) compared with the fit results (colored histograms). Bottom-left: χ^2 distribution on the half symmetrized Dalitz plot. Bottom-right: Summary table with the fitted coefficients (moduli and phases) for the intermediate states that significantly contribute to the total amplitude.

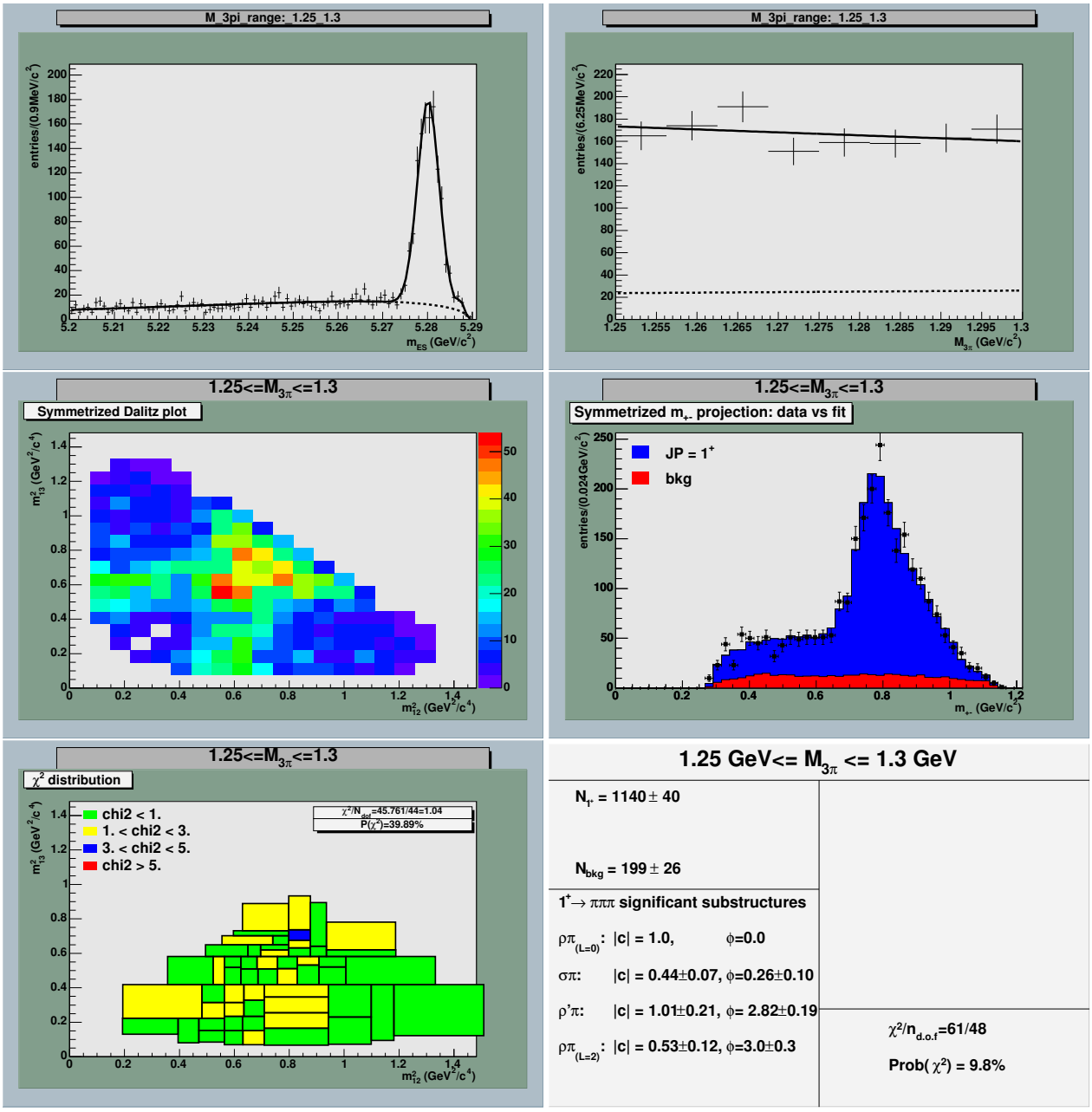

Figure 5.15: Results of the spin parity analysis in the [1.25 GeV, 1.3 GeV] $M_{3\pi}$ interval. Top-left: $m_{\rm ES}$ distribution (data vs. fit). Top-right: $M_{3\pi}$ distribution (data vs. fit). Middle-left: Symmetrized Dalitz plot distribution. Middle-right: Symmetrized m_{+-} distribution (2 entries per event) compared with the fit results (colored histograms). Bottom-left: χ^2 distribution on the half symmetrized Dalitz plot. Bottom-right: Summary table with the fitted coefficients (moduli and phases) for the intermediate states that significantly contribute to the total amplitude.

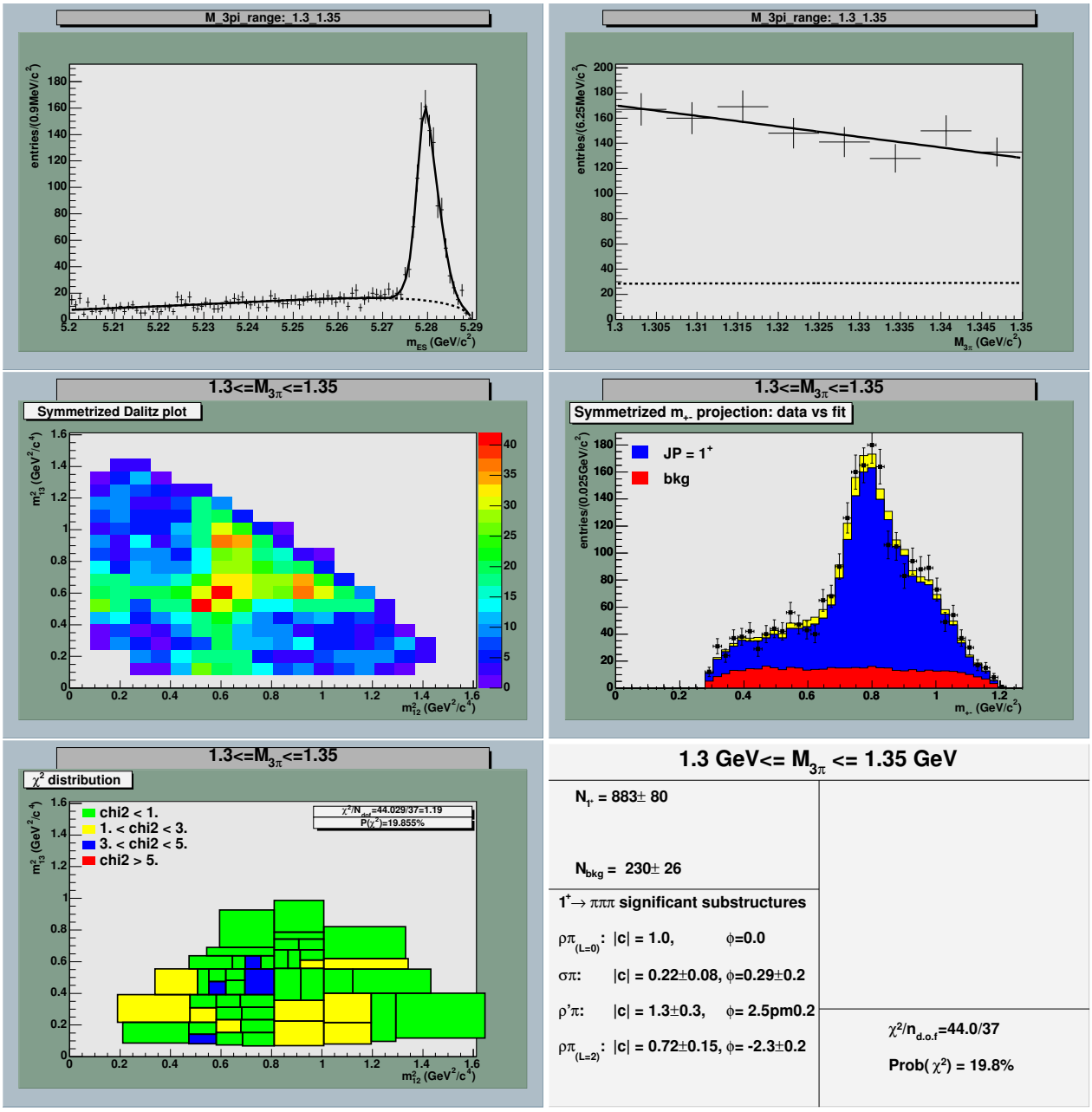

Figure 5.16: Results of the spin parity analysis in the [1.3 GeV, 1.35 GeV] $M_{3\pi}$ interval. Top-left: $m_{\rm ES}$ distribution (data vs. fit). Top-right: $M_{3\pi}$ distribution (data vs. fit). Middle-left: Symmetrized Dalitz plot distribution. Middle-right: Symmetrized m_{+-} distribution (2 entries per event) compared with the fit results (colored histograms). Bottom-left: χ^2 distribution on the half symmetrized Dalitz plot. Bottom-right: Summary table with the fitted coefficients (moduli and phases) for the intermediate states that significantly contribute to the total amplitude.

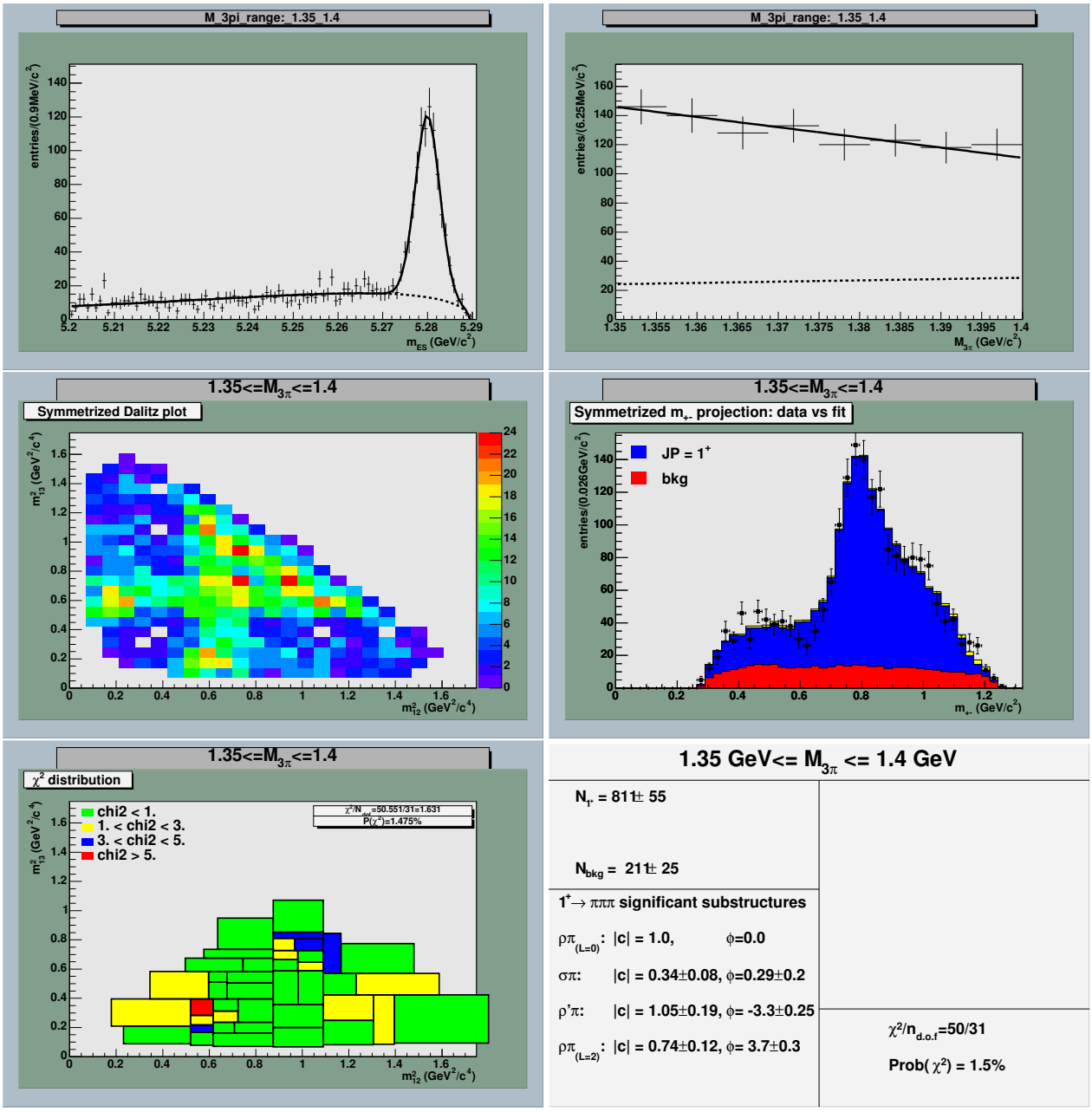

Figure 5.17: Results of the spin parity analysis in the [1.35 GeV, 1.4 GeV] $M_{3\pi}$ interval. Top-left: $m_{\rm ES}$ distribution (data vs. fit). Top-right: $M_{3\pi}$ distribution (data vs. fit). Middle-left: Symmetrized Dalitz plot distribution. Middle-right: Symmetrized m_{+-} distribution (2 entries per event) compared with the fit results (colored histograms). Bottom-left: χ^2 distribution on the half symmetrized Dalitz plot. Bottom-right: Summary table with the fitted coefficients (moduli and phases) for the intermediate states that significantly contribute to the total amplitude.

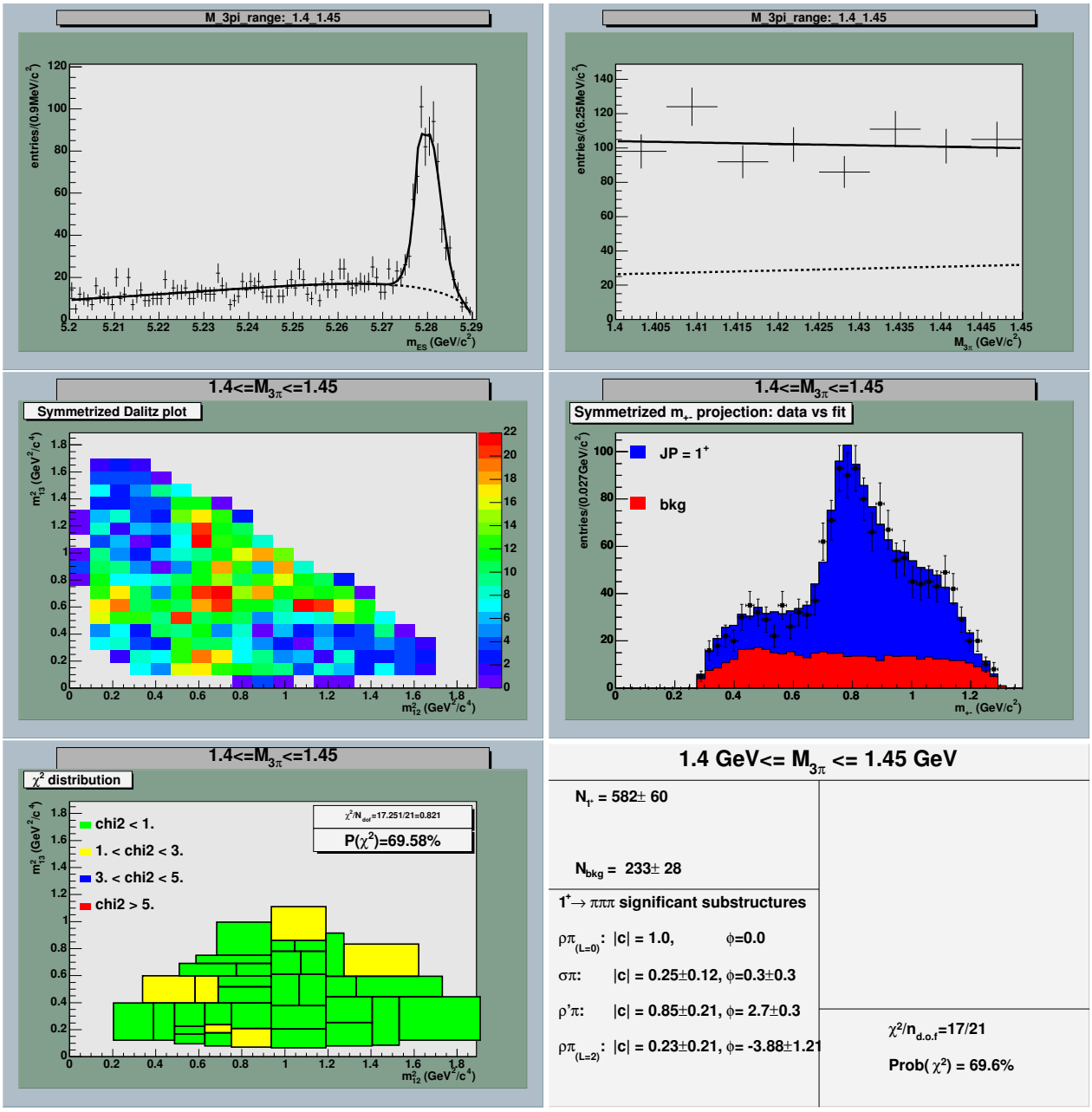

Figure 5.18: Results of the spin parity analysis in the [1.4 GeV, 1.45 GeV] $M_{3\pi}$ interval. Top-left: $m_{\rm ES}$ distribution (data vs. fit). Top-right: $M_{3\pi}$ distribution (data vs. fit). Middle-left: Symmetrized Dalitz plot distribution. Middle-right: Symmetrized m_{+-} distribution (2 entries per event) compared with the fit results (colored histograms). Bottom-left: χ^2 distribution on the half symmetrized Dalitz plot. Bottom-right: Summary table with the fitted coefficients (moduli and phases) for the intermediate states that significantly contribute to the total amplitude.

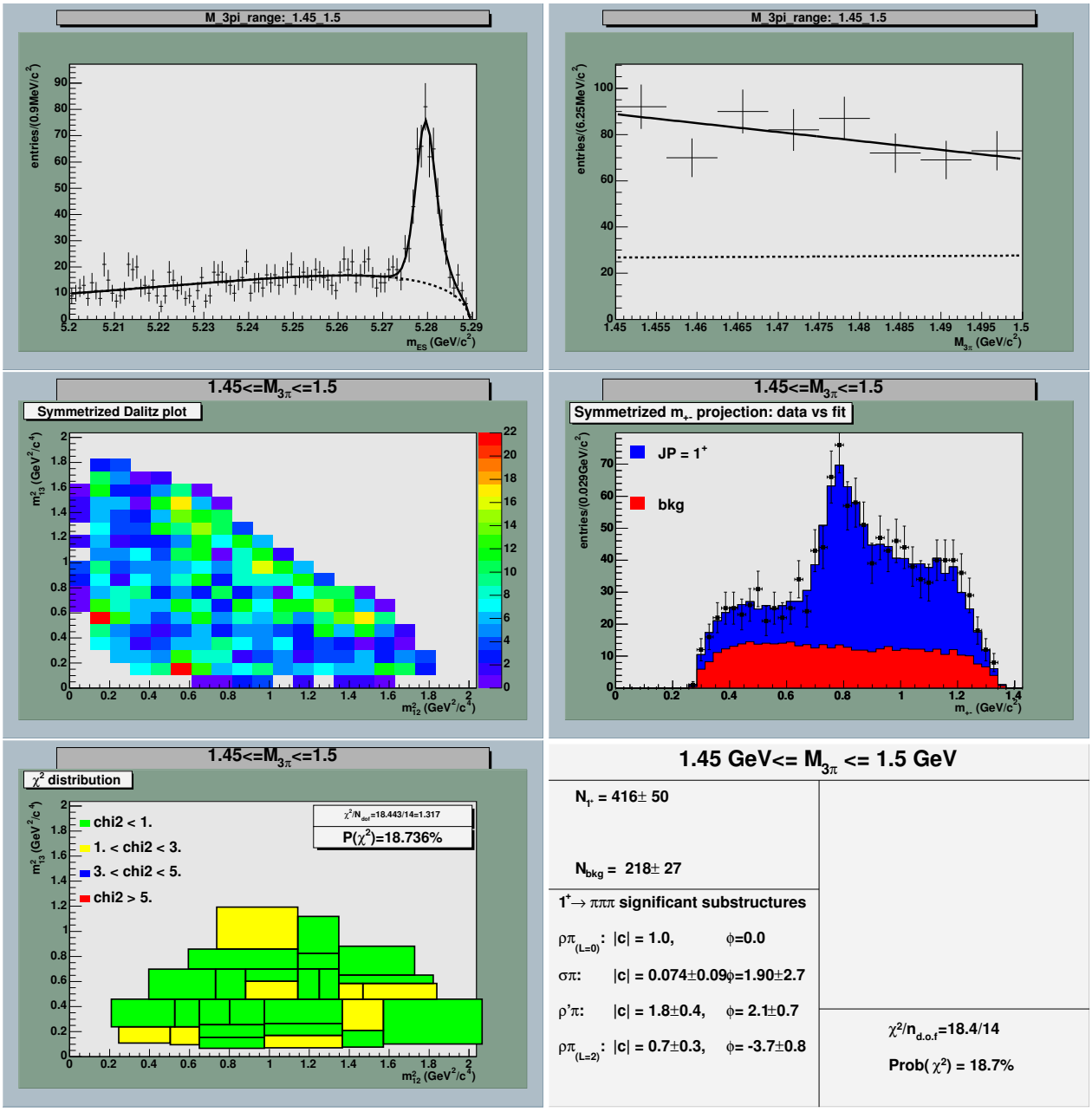

Figure 5.19: Results of the spin parity analysis in the [1.45 GeV, 1.5 GeV] $M_{3\pi}$ interval. Top-left: $m_{\rm ES}$ distribution (data vs. fit). Top-right: $M_{3\pi}$ distribution (data vs. fit). Middle-left: Symmetrized Dalitz plot distribution. Middle-right: Symmetrized m_{+-} distribution (2 entries per event) compared with the fit results (colored histograms). Bottom-left: χ^2 distribution on the half symmetrized Dalitz plot. Bottom-right: Summary table with the fitted coefficients (moduli and phases) for the intermediate states that significantly contribute to the total amplitude.

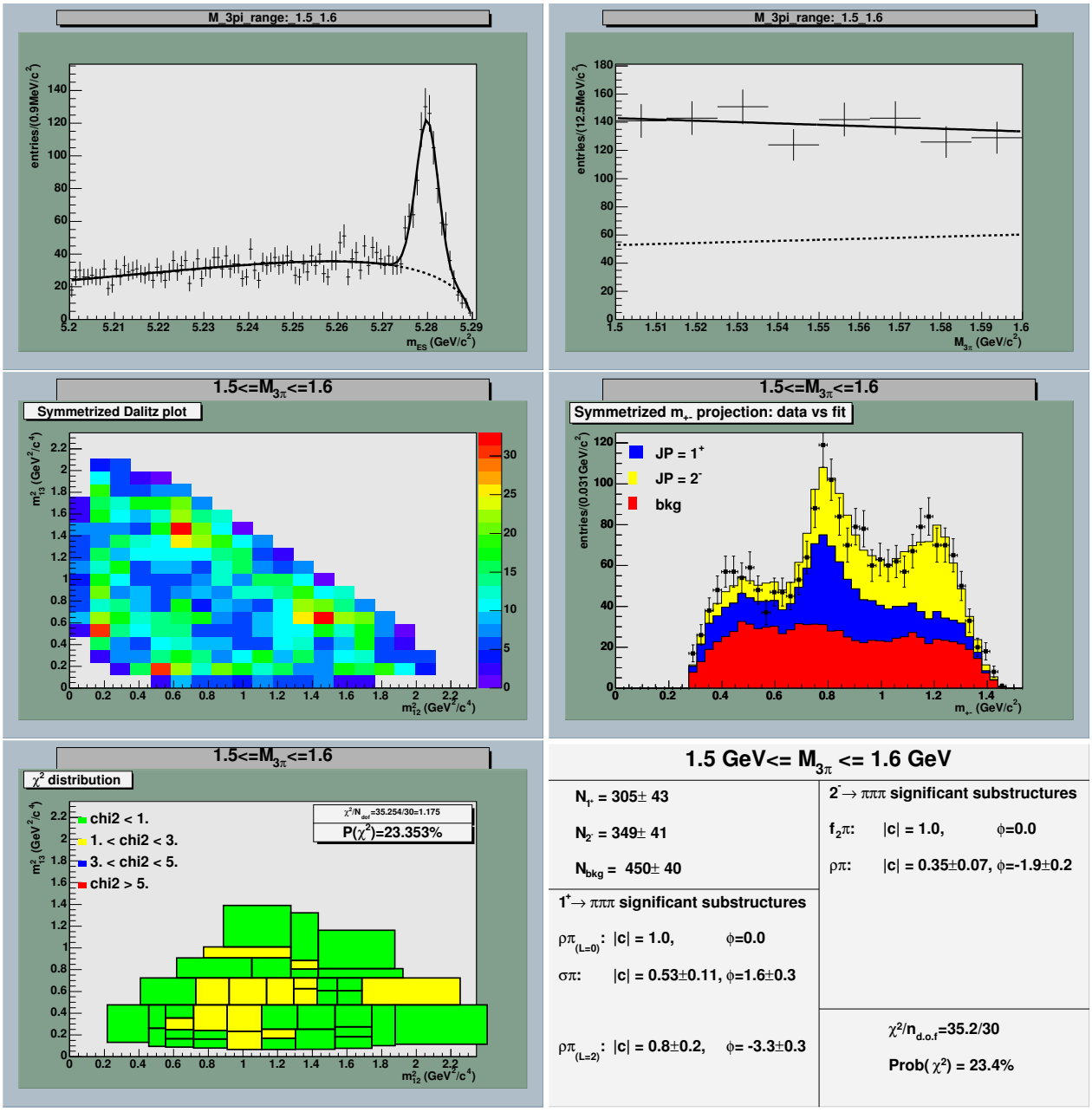

Figure 5.20: Results of the spin parity analysis in the [1.5 GeV, 1.6 GeV] $M_{3\pi}$ interval. Top-left: $m_{\rm ES}$ distribution (data vs. fit). Top-right: $M_{3\pi}$ distribution (data vs. fit). Middle-left: Symmetrized Dalitz plot distribution. Middle-right: Symmetrized m_{+-} distribution (2 entries per event) compared with the fit results (colored histograms). Bottom-left: χ^2 distribution on the half symmetrized Dalitz plot. Bottom-right: Summary table with the fitted coefficients (moduli and phases) for the intermediate states that significantly contribute to the total amplitude.

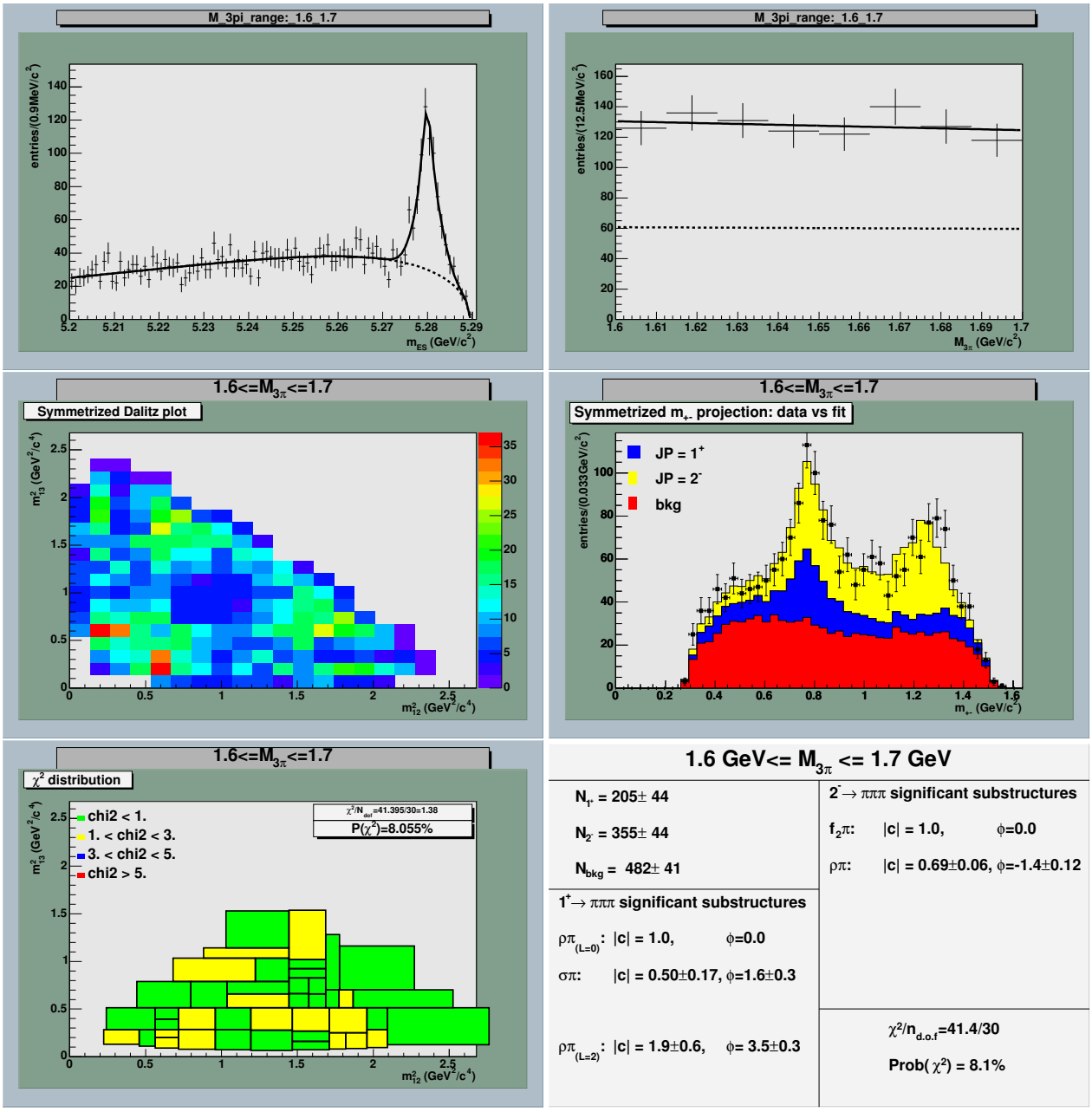

Figure 5.21: Results of the spin parity analysis in the [1.6 GeV, 1.7 GeV] $M_{3\pi}$ interval. Top-left: $m_{\rm ES}$ distribution (data vs. fit). Top-right: $M_{3\pi}$ distribution (data vs. fit). Middle-left: Symmetrized Dalitz plot distribution. Middle-right: Symmetrized m_{+-} distribution (2 entries per event) compared with the fit results (colored histograms). Bottom-left: χ^2 distribution on the half symmetrized Dalitz plot. Bottom-right: Summary table with the fitted coefficients (moduli and phases) for the intermediate states that significantly contribute to the total amplitude.

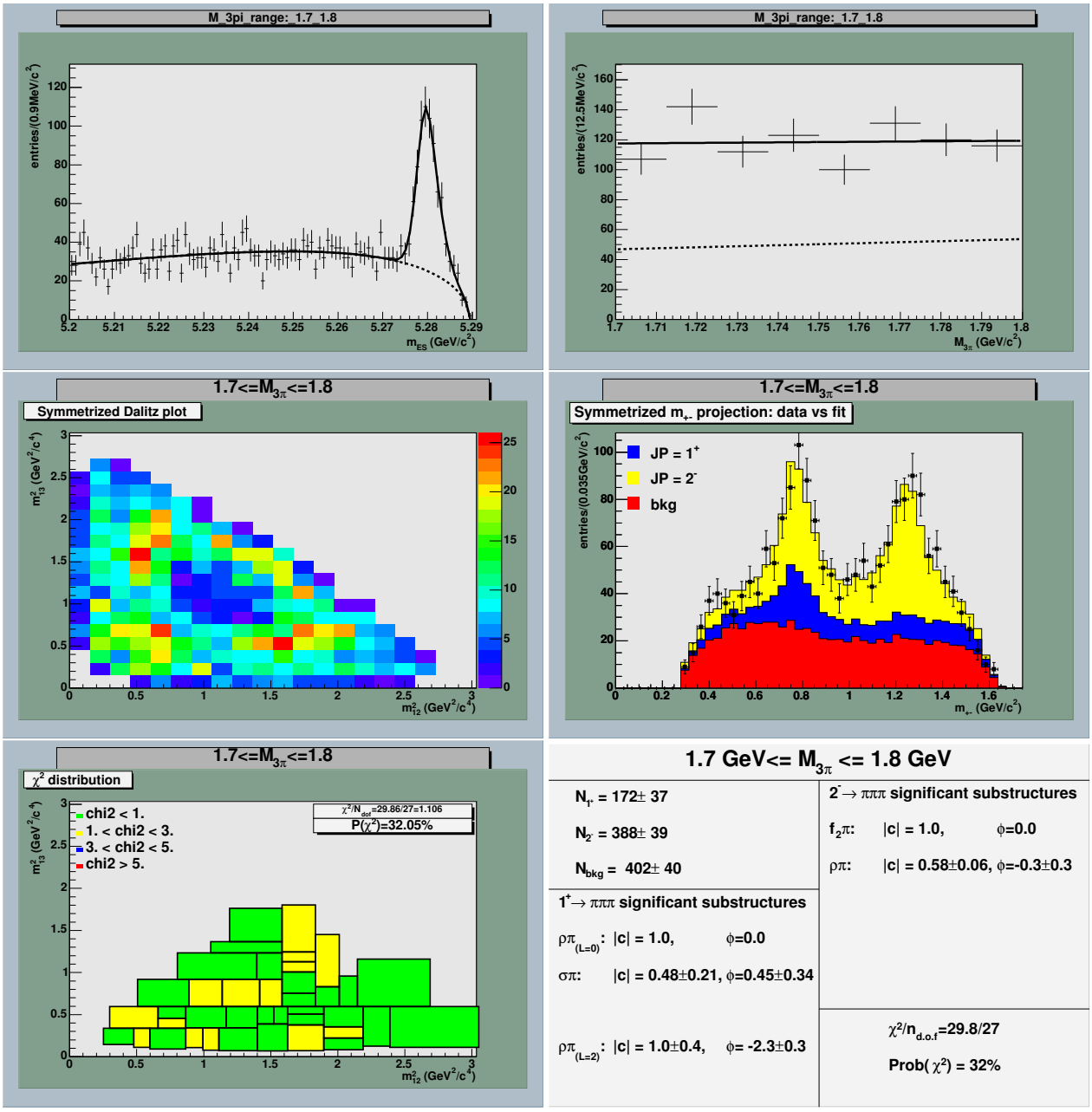

Figure 5.22: Results of the spin parity analysis in the [1.7 GeV, 1.8 GeV] $M_{3\pi}$ interval. Top-left: $m_{\rm ES}$ distribution (data vs. fit). Top-right: $M_{3\pi}$ distribution (data vs. fit). Middle-left: Symmetrized Dalitz plot distribution. Middle-right: Symmetrized m_{+-} distribution (2 entries per event) compared with the fit results (colored histograms). Bottom-left: χ^2 distribution on the half symmetrized Dalitz plot. Bottom-right: Summary table with the fitted coefficients (moduli and phases) for the intermediate states that significantly contribute to the total amplitude.

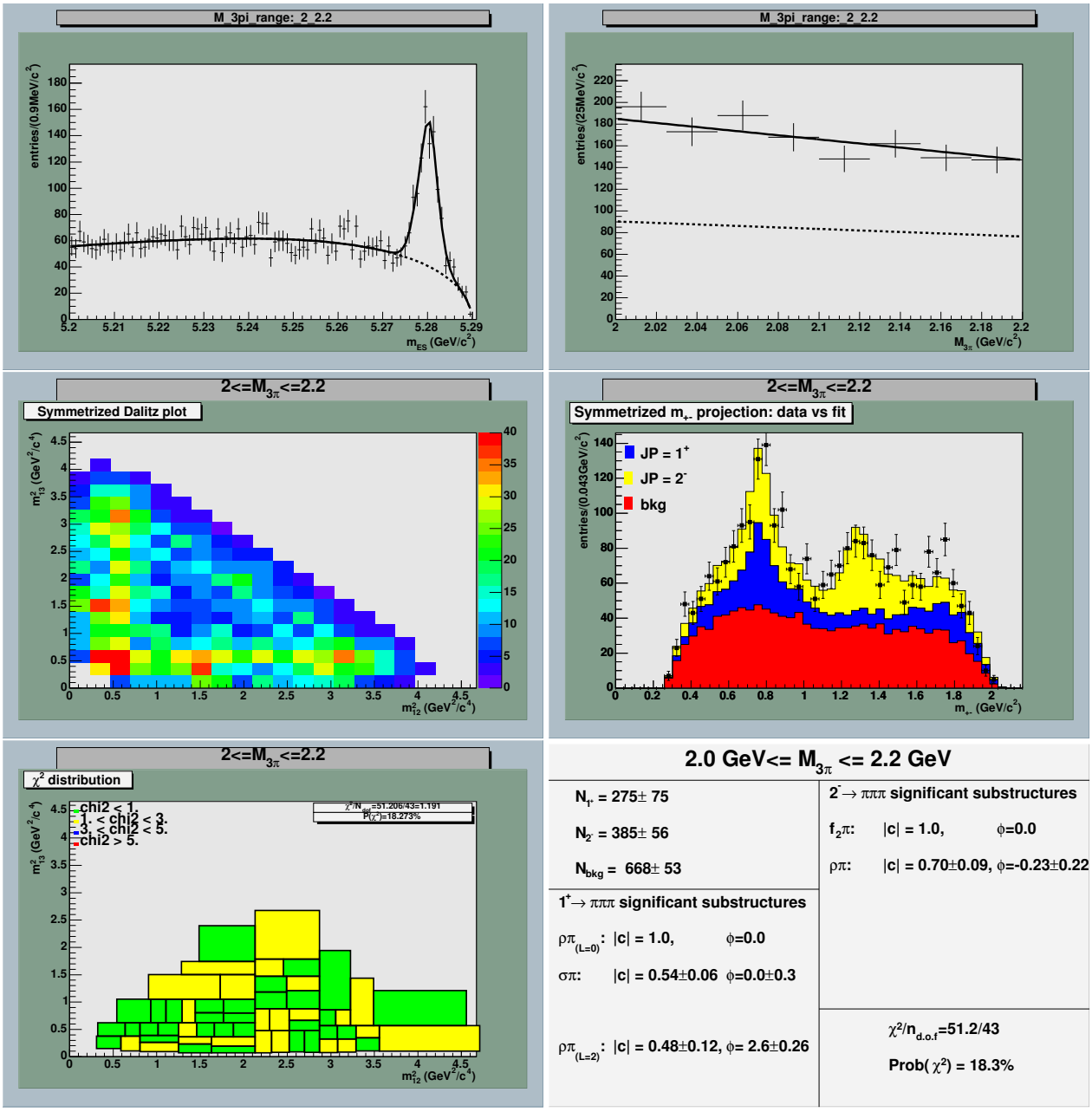

Figure 5.23: Results of the spin parity analysis in the [2.0 GeV, 2.2 GeV] $M_{3\pi}$ interval. Top-left: $m_{\rm ES}$ distribution (data vs. fit). Top-right: $M_{3\pi}$ distribution (data vs. fit). Middle-left: Symmetrized Dalitz plot distribution. Middle-right: Symmetrized m_{+-} distribution (2 entries per event) compared with the fit results (colored histograms). Bottom-left: χ^2 distribution on the half symmetrized Dalitz plot. Bottom-right: Summary table with the fitted coefficients (moduli and phases) for the intermediate states that significantly contribute to the total amplitude.

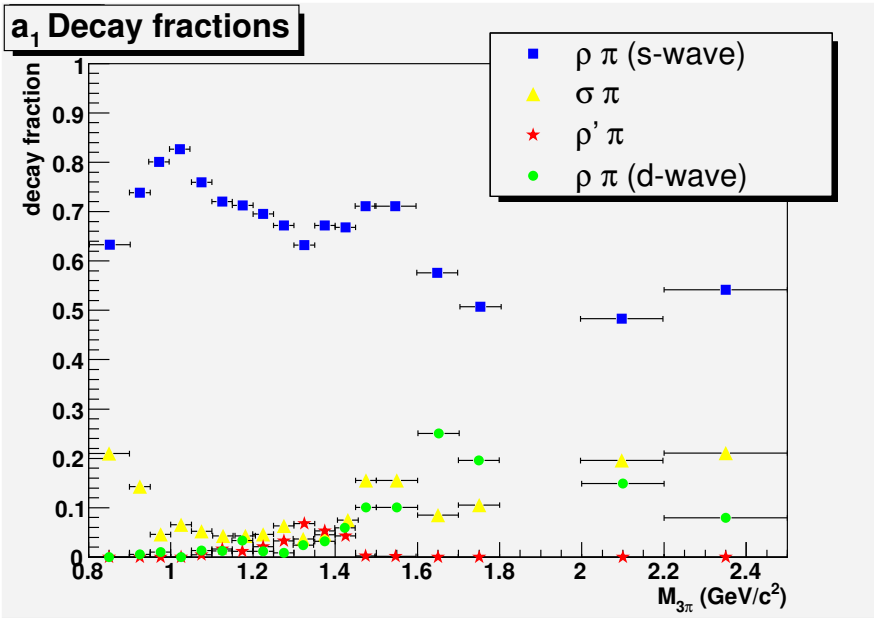

Figure 5.24: "Decay fractions" for the $a_1 \to \pi\pi\pi$ substructures.

5.6 $a_1(1260)$ decay fractions

From the Isobar complex coefficients appearing in 5.23 it is possible to define the quantities:

$$f_{ij} = \int_{M_1}^{M_2} dM\mathcal{P}(M)\frac{c_i c_j^* I_{ij}(M)}{\sum_{i,j} c_i c_j^* I_{ij}(M)}. \tag{5.28}$$

The diagonal terms f_{ii} are real and are usually interpreted as the "decay fraction" in the intermediate state i. However, due to the interference terms, these fractions does not sum to one while from the above definition follows

$$\sum_{i,j} f_{i,j} = 1. \tag{5.29}$$

These quantities are widely used in the Dalitz plot analysis as their values does not depend on the convention choice adopted in the fit of the Isobar coefficient c_i (eq.5.27).

For the a_1 resonance we have found significant contributions of the $a_1 \to \rho\pi$ (S and D waves), $a_1 \to \sigma\pi$ and $a_1 \to \rho'\pi$ channels. Figure 5.24 shows the central values of these "decay fractions" as a function of the 3 pions mass $M_{3\pi}$.

The $\rho\pi$ s-wave contribution is the dominant one, as expected, with a decay rate around 70% in qualitatively agreement with the CLEO analysis [48].

The $\sigma\pi$ coefficient $|c_{\sigma\pi}|$ significantly differ from zero in each $M_{3\pi}$ interval.
Its decay fraction increase in the a_1 tail region. Also the $\rho\pi$ d-wave amplitude become more important at high $M_{3\pi}$ values.
In the most populated bins (1.2-1.5 GeV) we also have sensitivity to the $\rho'\pi$ contribution.
We don't find significant contribution for the other scalar intermediate states ($f_0(980)$, $f_0(1370)$).
The determination of the statistic uncertainties $\sigma(f_{ii})$ on the decay fractions require a careful treatment of the correlation between the complex coefficients c_i and is actually under study. A possible strategy is to apply the same Monte Carlo technique often used in the $D^0 \to 3$ bodies Dalitz plot analyses [73]. Once the fit is converged and the covariance matrix is available, the solution from the fit is randomly modified according to the covariance matrix [74]. For each iteration, new fractions have to be computed and the resulting distributions can be fitted with Gaussian whose σ's give the errors on the fractions.

5.7 $a_1(1260)$ line-shape measurement

The spin-parity analysis described in section 5.5 allows us to extract the N_{1^+} yields in each bin of the three pions mass spectrum.
From these quantities we obtain the a_1 mass distribution by unfolding for the efficiencies effects estimated from the Monte Carlo simulation as described in section 5.4.
The a_1 line-shape can be modeled with a relativistic Breit Wigner, using the following expression [75]:

$$\frac{dN}{dm} = N\frac{m_{a_1}\Gamma_{a_1}(m)}{(m^2 - m_{a_1}^2)^2 + \Gamma^2(m)m^2 a_1}, \tag{5.30}$$

where $\Gamma_{a_1}(m)$ is a mass dependent width of the form:

$$\Gamma_{a_1}(m) = \Gamma_{a_1}(m_{a_1})\frac{f(m)}{f(m_{a_1})} \tag{5.31}$$

and f(m) is a phase space factor term, here parametrized by a 2^{nd} order polynomial.

We performed a minimum χ^2 fit to the a_1 line-shape to determine the line-shape parameters. The χ^2 is defined as:

$$\chi^2 = \sum_{i=1}^{N_{bins}} \frac{(N_{a_1}^i - N_{expected}^i)^2}{\sigma^2(N_{a_1}^i)}. \tag{5.32}$$

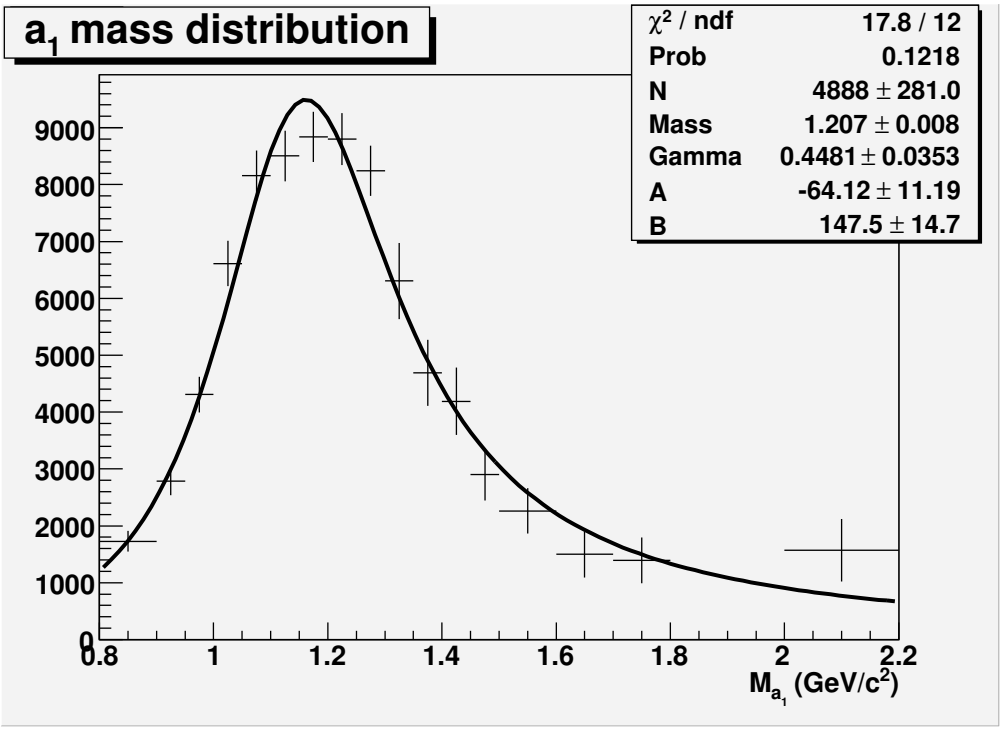

Figure 5.25: Fit to the efficiency unfolded a_1 mass distribution.

Here $N^i_{a_1}$ is the measured number of $J^P = 1^+$ events in the i-th bin divided by the selection efficiency in that bin and $\sigma^2(N^i_{a_1})$ is the error on $N^i_{a_1}$ obtained by propagating the statistical uncertainty on $N^i_{1^+}$ (quoted from the Dalitz plot fit) and the error on the efficiency, due to the finite Monte Carlo statistics. The quantity $N^i_{expected}$ is given by:

$$N^i_{expected} = \int_{min[i]}^{max[i]} dm \frac{dN}{dm}, \tag{5.33}$$

where min[i] and max[i] are the bounds of the i-th bin.
The result of the fit is shown in figure 5.25.

We find the following values for the mass and width of the a_1 meson:

$$m_{a_1} = 1.207 \pm 0.008 \text{ GeV}/c^2 \tag{5.34}$$

and

$$\Gamma_{a_1} = 450 \pm 0.035 \text{ MeV}/c^2, \tag{5.35}$$

with a $\chi^2/n_{d.o.f.} = 18/12$. The errors here quoted ere statistic only. The systematic uncertainties will be evaluated in the prosecution of the work. Section 5.8 contains a discussion on the main systematic uncertainty sources affecting this measurement.
Our measurements of m_{a_1} and Γ_{a_1} are in good agreement with the PDG estimates[13]. It should be noticed, however, that a direct comparison between the currently available measurements of the a_1 parameters is not completely meaningful since different experiments use different models to parametrize the a_1 line-shape. The model used here, was previously adopted by the WA76 [76] and WA103 [77] collaborations that give consistent results.

5.8 Plan for systematic uncertainties study

We summarize here the main sources of the systematic uncertainty affecting the a_1 parameters measurement. A quantitative determination of their impact on our measurement will be achieved in the prosecution of the work.

5.8.1 Model assumptions

A first class of systematic uncertainties is due to the assumptions made in our Isobar model parameterization. We have fixed the intermediate resonance masses and widths in the Breit-Wigner expressions taking their values from the PDG. However some of these quantity are not well determined and their uncertainty affect the yields determination in each $M_{3\pi}$ bin. A systematic uncertainty can be evaluated by repeating the Isobar fit with these parameter modified within the errors and by measuring how the resulting a_1 mass distribution is modified.

It should be noticed, however, that the standard Isobar model, we have adopted in this work, is not the only available model to describe three body decays. An alternative approach is the so called K-matrix formalism [78]. It results particularly suitable to treat the case of overlapping intermediate states with the same quantum numbers. The diffusion of this approach is increasing in the last years, in particular in the analysis of the spin-less charmed meson decays. Its application to the analysis presented year is made difficult by the need of take into account initial states with higher spin.

5.8.2 Background shape uncertainties

As we have seen in section 5.3, the PDFs describing the combinatorial background in the various bins are obtained by smoothing the "Grand Sideband" experimental Dalitz plot histograms in the (m',θ') coordinates. Each bin of these histogram is affected by a statistical error that is neglected in the smoothing procedure. To estimate the impact of this effect on the Isobar fit results we plan to repeat our fits in several configurations each obtained by random fluctuating the bin contents in accordance with their errors. The widths of the distributions of the results on the fitted parameters can be taken as systematic uncertainties.

5.8.3 Efficiency across the Dalitz plot

In section 5.4, we have seen how the selection efficiency effects are evaluated from the Monte Carlo simulation. Although the efficiency distributions across the Dalitz plots in the various $M_{3\pi}$ intervals was found to be flat within the errors, the Monte Carlo statistics actually available is not sufficient to perform a finely binned map. A Monte Carlo production of a 10 times higher populated sample of signal events is planned to improve our understanding of the efficiency distorting effects on the Dalitz plot distributions.

5.8.4 Efficiency vs $M_{3\pi}$

The statistical uncertainties on the efficiencies is taken into account in the unfolding of the a_1 mass distribution. However, the data Monte Carlo discrepancies have to be taken into account as a source of systematic uncertainty on the $M_{3\pi}$ distribution. These effects can be studied by means of suitable control samples [79]. Since the line-shape measurement is affected by the slope that describe the variations across the $M_{3\pi}$ bins and not on the absolute values of the efficiencies, the main source of systematic error is expected to be the due to the simulation of the soft pion tracking efficiency (see 5.4). A control sample of inclusive D^{*+} mesons decaying to $D^0\pi^+$ ($D^0 \to K^-\pi^+$) and charge-conjugate processes can be used to evaluate this effect and how it contribute to the total

systematic error.

Conclusions

This thesis has presented a data analysis work performed in the context of the BABAR experiment and aimed at studying the properties of the a_1 meson produced in $B \to D^{*-} a_1^+$ decays.
The analysis is based on data collected by BABAR in 1999-2004 corresponding to an integrated luminosity of 208.7 fb^{-1}.
The selected sample of events is divided in 17 bins of the 3 pions invariant mass and in each interval a Dalitz plot analysis, based on the Isobar model, was performed to disentangle the a_1 meson ($J^P = 1^+$) from other possible spin parity states. We have found that below 1.5 GeV the only contributing resonance is the a_1 meson while at higher values of $M_{3\pi}$ also a significant contribution of a $J^P = 2^-$ state was found,corresponding to the $\pi_2(1600)$ mass region. The extracted a_1 mass distribution was fitted with a relativistic Breit-Wigner to determine the line-shape parameters. We found the following preliminary results for the a_1 pole mass and width:

$$m_{a_1} = 1.207 \pm 0.008 \text{ GeV}/c^2 \tag{5.36}$$

and

$$\Gamma_{a_1} = 450 \pm 0.035 \text{ MeV}/c^2, \tag{5.37}$$

where the quoted error are statistic only. These results are in agreement with the PDG estimates [13]. The main sources of systematic uncertainty to this measurement were detected and a quantitative determination will be achieved in the prosecution of the work.

The study of the a_1 substructures has pointed out that, beside to the main $(1^+ \to \rho\pi)_{s-wave}$ amplitude, also the $1^+ \to \sigma\pi$, $(1^+ \to \rho\pi)_{d-wave}$, and $1^+ \to \rho'\pi$ intermediate states give not negligible contributions to the total $a^+ \to \pi^-\pi^+\pi^+$ amplitude.

Bibliography

[1] S.L. Glashow, Nucl. Phys. **22** (1961) 579;
S. Weinberg, Phys. Rev. Lett. **19** (1967) 1264;
A. Salam, in *Proc. 8th Nobel Symp.*, ed. N. Swartholm,
Almquist and Wiksells, Stockholm (1968).

[2] M. E. Peskin and D.V. Schroeder, *An Introduction to Quantum Field Theory*, Addison-Wesley Publishing Company (1995) .

[3] F. Mandel and G. Shaw, *Quantum Field Theory*, John Wiley and Sons Ltd. (1984) .

[4] T. Muta, *Foundations of Quantum Chromodynamics*, World Scientific (1987).

[5] See for example Chapter 20 in Reference [2].

[6] A. Ali and B. Kayser, Quark Mixing and CP Violation, hep-ex/9806230 (1998).

[7] M. Kobayashi and T. Maskawa, Prog. Th. Phys. **49**, 652 (1973).

[8] N. Cabibbo, Phys. Rev. Lett. **10**, 531 (1963).

[9] S. W. Herb *et al.,*, Phys. Rev. Lett. **39**, 252 (1977).

[10] W. R. Innes *et al.,*, Phys. Rev. Lett. **39**, 1240 (1977).

[11] F. Abe *et al.,*, Phys. Rev. Lett. **74**, 2626 (1995).

[12] A. Abachi *et al.,*, Phys. Rev. Lett. **74**, 2632 (1995).

[13] Particle Data Group S. Eidelman et al., Phys. Lett. B **592**, 1 (2004)

[14] L. L. Chau and W. Y. Keung, Phys. Rev. Lett. **53**,1802 (1984).

[15] J. D. Bjorken, Phys. Rev. D **39**, 1396 (1989).

[16] C. Jarlskog and R. Stora, Phys. Lett. **B208**, 268 (1988).

[17] L. Wolfenstein, Phys. Rev. Lett. **51**, 1945 (1983).

[18] A. J. Buras, M.E. Lautenbacher and G. Ostermaier, Phys. Rev. D **50**, 3433 (1994).

[19] M. Bona *et al.,*[UTfit collaboration], hep-ph/0509219. for the last updates http://www.utfit.org

[20] T. Inami and C.S. Lim,*Prog. Theor. Phys.* **65** (1981) 297;

[21] G. Buchalla, A. J. Buras e M. E. Lautenbacher, *Rev. Mod. Phys.* **68** (1996) 1125 [hep-ph/9512380].

[22] A.J. Buras, M. Jasmin and P.H. Weisz, *Nucl. Phys. B* **347** (1990) 491.

[23] S. Herrlich and U. Nierste, *Nucl. Phys. B* **419** (1994) 192. *ibid.* **65** (1981) 1772.

[24] G. S. Branco, L. Lavoura, and J. P. Silva, *CP Violation*, Oxford Science Publications (1999)

[25] J.J. Sakuray, *Modern Quantum Mechanics, Revised Edition*, Addison-Wesley (1985).

[26] David London,Nita Sinha,Rahul Sinha hep-ph/0104157 (2001).

[27] M. Gronau, D. Pirjol, D. Wyler, Phys. Rev. Lett. **90**, 051801 (2003)

[28] B.Aubert *et al.*, [*BABAR* Collaboration], SLAC-PUB-8569, [hep-ex/0105044].

[29] P.Billoir, *Nucl.Instr.Methods* , A225 (1984) 225

[30] T. Brandt, "Likelihood Based Electron Identification", *BABAR* Analysis Documents #396 (2002).

[31] K.G. Wilson, Phys. Rev. **179** 1499 (1969)

[32] M. Bauer, B. Stech and M.Wirbel, Z. Phys. C 34, 103 (1987).

[33] R. Fleisher CERN-PH-TH/2004-85
hep-ph/04005091
Lectures given to the 2003 European school of High Energy Physics,
Tsakhkadzor, Armenia, 24 August-6 September 2003.

[34] F.J. Gilman and M.B. Wise, Phys. Rev. **D20** (1979) 2392;
G. Altarelli, G. Curci, G. Martinelli and S. Petrarca, Phys. Lett. **B99** (1981) 141;
A.J. Buras and P.H. Weisz, Nucl. Phys. **B333** (1990) 66.

[35] A.J. Buras, hep-ph/9806471, lectures given at Summer School on Theoretical Physics: Probing the Standard Model of Particle Interactions, Les Houches, France, 28 July – 5 September 1997.

[36] G. Buchalla, A.J. Buras and M.E. Lautenbacher, Rev. Mod. Phys. **68** (1996) 1125.

[37] M. Neubert, B. Stech, Adv. Ser. Direct. High Energy Phys. **15** (1998) 294, and references therein.

[38] A.J. Buras and J.-M. Gérard, Nucl. Phys. **B264** (1986) 371;
A.J. Buras, J.-M. Gérard and R. Rückl, Nucl. Phys. **B268** (1986) 16.

[39] M. Beneke, G. Buchalla, M. Neubert and C. Sachrajda, Phys. Rev. Lett. **83** (1999) 1914;
Nucl. Phys. **B591** (2000) 313; Nucl. Phys. **B606** (2001) 245.

[40] J.D. Bjorken, Nucl. Phys. (Proc. Suppl.) **B11** (1989) 325;
M. Dugan and B. Grinstein, Phys. Lett. **B255** (1991) 583;
H.D. Politzer and M.B. Wise, Phys. Lett. **B257** (1991) 399.

[41] H.-n. Li and H.L. Yu, Phys. Rev. **D53** (1996) 2480;
Y.Y. Keum, H.-n. Li and A.I. Sanda, Phys. Lett. **B504** (2001) 6;
Y.Y. Keum and H.-n. Li, Phys. Rev. **D63** (2001) 074006;
Y.Y. Keum and A.I. Sanda, eConf **C0304052** (2003) WG420 [hep-ph/0306004].

[42] C.W. Bauer, D. Pirjol and I.W. Stewart, Phys. Rev. Lett. **87** (2001) 201806;
C.W. Bauer, B. Grinstein, D. Pirjol and I.W. Stewart, Phys. Rev. **D67** (2003) 014010.

[43] A. Khodjamirian, Nucl. Phys. **B605** (2001) 558;
A. Khodjamirian, T. Mannel and B. Melic, Phys. Lett. **B571** (2003) 75.

[44] A.J. Buras, R. Fleischer, S. Recksiegel, F. Schwab, CERN-PH-TH/2004-020 [hep-ph/0402112].

[45] A.J. Buras, R. Fleischer, S. Recksiegel and F. Schwab, *Phys. Rev. Lett.* **92** (2004) 101804.

[46] R.Deck Phys. Rev. Lett. **13,169**

[47] P.Gavillet *et al.,*Phys. Lett. **69B**, 119

[48] D.M. Asner *et al.,*(CLEO collaboraion) *Phys. Rev.* **D61**, 12002

[49] N. Isgur, C. Morningstar and C. Reader, *Phys. Rev.* **D39**, 1357 (1989) M. Feindt, Z. Phys. C 48, 681 (1990).

[50] N. Isgur and M. B. Wise, Phys. Lett. B **237**,527 (1990)

[51] BABAR-CONF-04/018, hep-ex/0408038

[52] BABAR-CONF-04/029, hep-ex/0408059

[53] Belle-CONF-0448, hep-ex/0408106

[54] Belle collaboration: PRL 93 (2004) 031802; Erratum-ibid. 93 (2004) 05990

[55] Suhu-Urk Chung:
SPIN FORMALISM -Updated Version-
BNL-QGS-02-0900

[56] M.E. Rose, Elementary theory of angular momentum
(John Wiley & Sons, Inc., New York, 1957).

[57] R.H.Dalitz *P*hil. Mag.**44** (1953) 1068

[58] C.G. Fox and S. Wolfram Phys. Rev. Lett. **41**,(1978) 1581

[59] S.Brandt *et al.,*Phys. Lett. **12**, (1964) 57
E.Fabri, Phys. Rev. Lett. **39** (1977) 1587

[60] F. Martinez *et al.,*, *The BABAR Vertexing*, *BABAR* Analysis Document 102 (2001).
Paul Avery, *Applied Fitting Theory*, CLEO Note CBX 91-72 (1991). Available online at
`http://www.phys.ufl.edu/~avery/fitting.html`.

[61] W.T. Ford, *Choice of Kinematic Variables in B Meson Reconstruction– Take 3*, *BABAR* Analysis Document #53, 2000.

[62] ARGUS Collaboration, Z. Phys. **C48**, 543 (1990).

[63] M.Abramovich *et al.,*, Nucl Phys **B23** (1970) 426

[64] J. Blatt and V. Weisskopf, "Theoretical Nuclear Physics", John Wiley & Sons, New York, 1956.

[65] C. Zemach, Phys. Rev. B 133 (1964)1201
C. Zemach, Phys. Rev. B 140 (1965)97

[66] V. Filippini, A. Fontana and A. Rotondi, *Phys. Rev.* **D51** 2247 1994

[67] W.H.Press *et al.,*
Numerical Recipies in C++, Chapter 3.
Cambridge University Press.

[68] BABAR collaboration hep-ex/0408099

[69] http://wwwasd.web.cern.ch/wwwasd/cernlib/mc/genbod.html

[70] R.Gardner and J. Wiss,
Asseessing Goodness of Fit Using Adaptive binning,
E687 Internal Note, 1994 http://www.hep.uiuc.edu/e687/memos/memos_st.html

[71] A.Pompili, An adaptive binning technique for Dalitz plot analyses.
BABAR Analysis Document # 506, 2003

[72] M.Diehl and G.Hiller hep-ph/0105194

[73] BABAR collaboration, SLAC-PUB-11333.
A.Palano, a Dalitz plot analysis of $D^0 \to \bar{K}^0 K^+ K^-$,
BaBar Analysis Document # 911

[74] See for example the algorithm CORSET in the CERN Library

[75] M.G. Bowler, Phys. Lett. **B182** (1986) 400

[76] T.A. Armstrong *et al.*,, Z. Phys. C 48,213 (1990)

[77] D. Barberis *et al.*,Phys. Lett. **B422** (1998) 399

[78] E.P. Wigner, Phys. Rev. **70** (1946) 15
E.P. Wigner and L. Eisenbud, Phys. Rev. **72** (1947) 29. R.H. Dalitz and S. Tuan, Ann. Phys. 10 (1960) 307

[79] BABAR analysis document # 867
"Tracking efficiency studies in release 12 and 14"
BABAR analysis document # 1056 "Particle Identifications control samples in BABAR "